High frequency amplification, filtering and nonlinearity in a computational model of mammalian cochlear mechanics

by

Julien Meaud

A dissertation submitted in partial fulfillment
of the requirements for the degree of
Doctor of Philosophy
(Mechanical Engineering)
in The University of Michigan
2010

Doctoral Committee:

Professor Karl Grosh, Chair
Professor Carlos E. Cesnik
Associate Professor Bogdan Epureanu
Assistant Professor Robert Keith Duncan

© Julien Meaud

2010

ACKNOWLEDGEMENTS

I would like to thank my advisor Dr. Karl Grosh for introducing me to the fascinating research topic of the mechanics of the cochlea and for his guidance and support throughout this project. I thank my committe members, Dr. Carlos E. Cesnik, Dr. Bobgdan Epureanu and Dr. R. Keith Duncan for their time and their interest in this thesis.

TABLE OF CONTENTS

LIST OF FIGURES

Figure

LIST OF TABLES

Table

LIST OF APPENDICES

Appendix

LIST OF ABBREVIATIONS

AFT alternating frequency time

BM basilar membrane

BP best place

CF characteristic frequency

DPOAE distortion product otoacoustic emission

EEOAE electrically evoked otoacoustic emission

FFT fast Fourier transform

HB hair bundle

IFFT inverse fast Fourier transform

IHC inner hair cell

OAE otoacoustic emission

OHC outer hair cell

OoC organ of Corti

OW oval window

RL reticular lamina

RW round window

SOAE spontaneous otoacoustic emission

ST scala tympani

StV stria vascularis

SV scala vestibuli

TM tectorial membrane

ABSTRACT

High frequency amplification, filtering and nonlinearity in a computational model of mammalian cochlear mechanics

by

Julien Meaud

Chair: Karl Grosh

In this thesis the active and nonlinear dynamics of the mammalian cochlea in response to acoustic stimulation are simulated using a computational model of the physics and physiology of the cochlea. The model is based on a three-dimensional representation of the cochlear partition and intracochlear fluid and includes the electrical domain and linear feedback from outer hair cell (OHC) somatic motility.

A linear version of the model of the cochlea is first used to assess the role of structural longitudinal coupling in cochlear mechanics. Longitudinal coupling in the TM and BM mechanics is found to improve the predictions compared to a locally reacting model as it broadens the frequency response of the BM to acoustic stimulation and reduces the duration of the impulse response.

The linear model of the cochlea is then used to investigate the identity of the cochlear amplifier - prestin-based somatic motility or hair bundle (HB) motility. A nonlinear six-state channel model of the active HB is linearized for small harmonic perturbation around the operating point and implemented in the macroscopic model of the cochlea. A calcium binding event models fast adaptation of the transduc-

tion current and active HB force generation. The macroscopic simulations show that somatic motility underlies cochlear amplification and that the active HB force is insufficient to modulate the response of the BM to low intensity acoustic stimulation. However, the reduction of the sensitivity of the transduction channel to HB deflection due to the fast adaptation mechanism controls the energy delivered by somatic motility and thereby the sensitivity of the BM to acoustic stimulation, stabilizing the cochlea.

The nonlinear dynamics of the cochlea are simulated by introducing a physiologically relevant nonlinearity in the mechanotransduction channel. An efficient alternating frequency/time method is used to compute the stationary response of the cochlea. The model predicts a realistic compressive response and generation of harmonic distortion in response to a single tone. The simulations of two tone interaction on the BM - two tone suppression and distortion products - are also in good agreement with published experimental data.

CHAPTER I

Introduction

1.1 Mammalian hearing mechanics

The role of the mammalian ear is to convert sound into neural impulses transmitted to the brain. The ear accomplishes its function with remarkable characteristics. For example, young humans can distinguish between frequencies only 0.2% apart and detect timing differences of 6 to 10 μs between sounds [29]. The mammalian ear responds to sounds over a very broad frequency range (about 10 octaves). Moreover it is very sensitive to low level acoustic input since subatomic internal movements (less than thermal noise induced movements) can be detected and transduced by the mammalian ear. It has a very broad dynamic range and can respond to sounds that have an energy a million times higher than the threshold of detection. To accomplish its goal with these characteristics the mammalian ear has evolved and has become a very complex nonlinear system. It consists of three parts: the external ear, the middle ear and the inner ear.

The external ear collects the sound pressure waves and channels them toward the tympanic membrane or eardrum. In response to acoustic stimulation the eardrum converts the acoustic wave to mechanical vibrations. These vibrations are transmitted through the bones of the middle ear (malleus, incus and stapes) to the oval window of the inner ear. The inner ear consists of the cochlea (the organ of hearing) and of

the vestibular apparatus (the organ of balance). The mechanics of the mammalian cochlea is the subject of this thesis.

1.2 Anatomy of the mammalian cochlea

The cochlea converts mechanical vibrations to neural impulses (electrical signals). It is spiral shaped and consists of three fluid-filled ducts (with a nearly incompressible fluid) : the scala vestibuli, scala media and scala tympani. The scala media and scala tympani are separated by the cochlear partition; the scala vestibuli and scala media are separated by Reissner's membrane which is acoustically transparent. The scala tympani and scala vestibuli connect at the apical end of the cochlea through an orifice called helicotrema. A membrane-covered opening called round window is present on the wall located at the basal end of the scala tympani. Because of the near incompressibility of the cochlear fluids, the presence of the round window is necessary to allow movements of the oval window, of the fluid and of the cochlear partition during acoustic stimulation. To facilitate the analysis of its mechanics, the cochlea is often represented using an uncoiled model, as shown in Fig. 1.1. The effect of coiling on the mechanics of the cochlea is probably limited to apical locations [92].

The cochlear partition comprises the basilar membrane (BM), the tectorial membrane (TM) and the organ of Corti (between the BM and the TM). The organ of Corti (OoC) consists of different cells and structures, notably the reticular lamina (RL) which is parallel to the TM, and the outer hair cell (OHC) between the BM and the RL. The sensory cell of the cochlea, also located on the cochlear partition, is the inner hair cell (IHC). Both the IHCs and OHCs have stereocilia or hair bundle (HB) that insert into the apical surface of the IHCs and OHCs (see Fig. 1.2). The stria vascularis (StV) is an important structure (to maintain the ionic balance of the cochlea) occupying the lateral wall of the scala media.

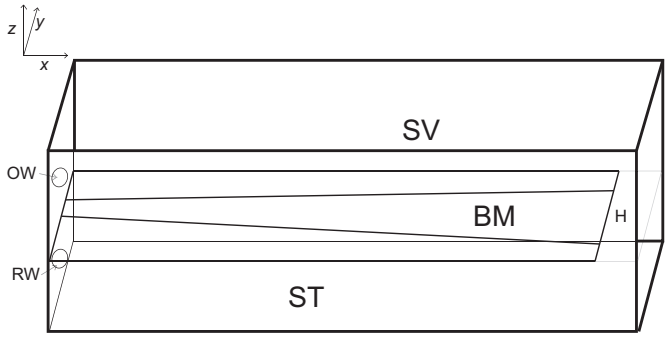

Figure 1.1: Idealized and uncoiled box model of the cochlea. x corresponds to the longitudinal direction, y to the radial direction and z to the vertical direction. The BM becomes wider and thinner as x increases, making its stiffness and resonant frequency lower. The cochlear partition (that includes the BM as well as the organ of Corti and the TM) separates the two ducts. The organ of Corti and the TM are not shown on the figure for clarity. The Reissner's membrane that separates the SV and scala media is not shown as it is acoustically transparent. The SV and ST connect at the end to the cochlear partition through an orifice called helicotrema (H on the figure). Acoustic stimulation excites the stapes attached to the OW. The RW vibrates to allow movement of the OW, of the nearly incompressible fluid and of the cochlear partition.

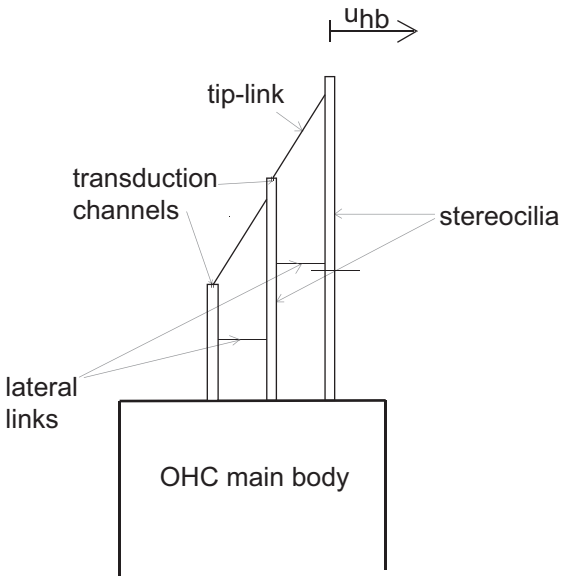

Figure 1.2: OHC and its stereocilia. Each OHC has 3 rows of stereocilia. The rows are connected by horizontal lateral links and by the tip-links. When the stereocilia is deflected by a displacement u_{hb}, the tip-link opens the transduction channels and allows current (carried mostly by potassium and also by calcium) to enter the cell.

1.3 Passive cochlear mechanics

Von Bekesy published in 1960 [7] his measurements of the response of the BM to acoustic stimulation in human cadavers using stromboscopic flashes of ordinary visible light (which limited the smallest measurable amplitudes to about 500nm [50]). He observed that the BM is tuned locally to specific frequencies and was awarded the Nobel prize in medicine in 1961 for his findings. At the base (close to the oval window) the BM responds primarily to high frequency sounds and at the apex to low frequency sounds. The geometrical [42] and mechanical properties of the structure of the cochlear partition, and particularly of the BM [60], are varying longitudinally. This explains the tonotopic tuning of the BM which acts as a spectral analyzer.

During acoustic stimulation, the fluid pressure difference between the scala tympani and scala vestibuli (due to the oval window excitation) forces the cochlear partition to vibrate. Because of the tonotopic tuning of the BM and of the fluid coupling, a longitudinally propagating wave travels on the BM until it reaches what is called the best place (BP). At the BP the resonant frequency of the cochlear partition matches the frequency of the excitation. The TM moves relative to the the RL due to the vibrations of the organ of Corti induced by the vibrations of the BM. Because of this motion and of the viscosity of the fluid, the fluid in the interstitial space between the TM and the RL moves and deflects the HBs of the inner hair cells (which are not attached to the TM). The transduction channels on the HBs of the IHCs opens and current depolarizes the IHCs, which sends a signal to the brain.

However, the BM is poorly tuned in the measurements from Von Bekesy. These measurements and the theory derived from them are not sufficient to explain the sharper tuning of the neural responses.

1.4 Active cochlear mechanics

1.4.1 Response to single tone

Rhode [123] measured in 1971 the response of the BM to high frequency acoustic stimuli in living animals using the Mössbauer effect (which can measure displacements in the nanometer range). He showed that, in contrast to the postmortem response, the BM of the living cochlea is highly sensitive and sharply tuned to low level stimuli. At a given longitudinal location, the peak frequency of the BM in response to low intensity stimulation in the living animal is called characteristic frequency (CF) of the location. These results have been validated by more recent measurements using the same method [142, 130] or alternative techniques [112, 20, 35, 159]. For instance, in the guinea pig [112, 20, 35, 159], the gain of the BM response relative to the stapes vibrations at CF for 10dB SPL tone is 35 to 40dB higher response in a living animal than the maximum postmortem gain (see Fig. 1.3). Moreover the peak frequency of the dead animal is lower than the CF. At frequencies significantly lower or higher than the frequency of the peak, the response is linear for any intensity of the input. When the magnitude of the stimuli is raised, the BM response becomes less sharp, the gain decreases and the peak shifts to a lower frequency. At 100dB SPL the BM response in a living animal is very similar to the response seen in a dead animal, with a peak at a frequency about half an octave lower than with a lower intensity stimulus, as well as a low gain and quality factor. Despite this nonlinear compressive response of the BM, there is not much harmonic distortion [20, 124] as the second harmonic component is about 30dB lower than the fundamental at CF. Moreover the DC shift is limited at basal locations, except at high intensity [23].

The response of the cochlea at more apical locations is more controversial [24, 83]. It is more difficult to take measurements of the BM vibrations at the apex. Different conclusions about the mechanics of the cochlea at low frequencies have been drawn

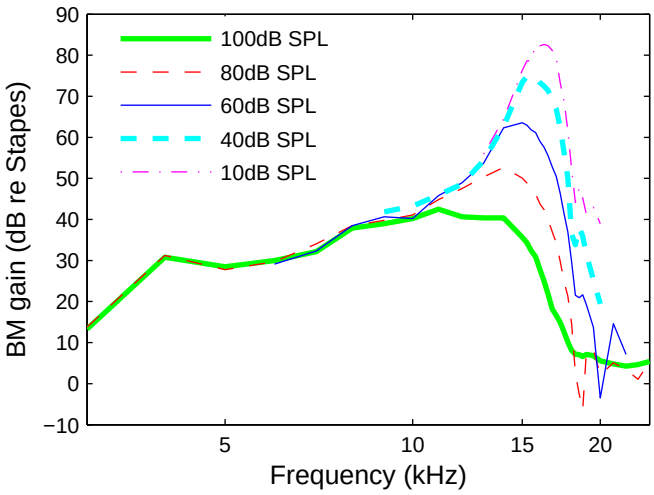

Figure 1.3: Experimental gain of the BM velocity relative to the stapes velocity in response to acoustic stimulation at the 17kHz best place. The gain is plotted as a function of frequency for different sound intensities. The experimental data is from [159]. Away from the characteristic frequency (17kHz) the gain is independent of the sound intensity, which indicates a linear response. Close to the CF, the BM gain is nonlinear as it is more sensitive, more sharply tuned and has a higher peak frequency at low intensity than at high intensity.

from these experiments. The work presented here focuses on the response at basal locations.

1.4.2 Two tone interaction: two tone suppression and distortion products

The response of a linear system to the sum of two harmonic stimuli is the superposition of the response to each stimulus. However in a nonlinear system such as the cochlea the principal of superposition does not apply. For example, an interesting phenomenon, first observed in psychoacoustic experiments, and later measured by Rhode [125] in the BM vibrations, is called two tone suppression [134, 109, 25]. Two tone suppression can be observed if the BM response to the sum of two tones of frequency f_1 and f_2 is measured at the BP of f_1. For these experiments f_1 is called the probe frequency and f_2 the suppressor frequency. The magnitude of the f_1 component of the BM response is reduced by the presence of the suppressor. Another interesting

two tone interaction is the presence of distortion products in the BM response to the sum of two tones of frequency f_1 and f_2 [131, 133]. The BM response can be measured not only at the frequencies primary tones f_1 and f_2, but also at combination frequencies (of the form $n_1 f_1 + n_2 f_2$, where n_1 and n_2 are signed integers).

1.4.3 Otoacoustic emissions

Another interesting characteristic of the cochlea of living animals is the observation of the sound emitted by the ear, called otoacoustic emission (OAE) and discovered by Kemp in 1978 [78]. For instance, in more than 50% of the population [50], sound can be measured at the external canal in the absence of acoustic stimulation (these emissions are called spontaneous otoacoustic emission (SOAE)). When the ear is stimulated simultaneously by two tones with frequency f_1 and f_2, the presence of distortion product otoacoustic emission (DPOAE) can be measured in the ear canal at a cross-product frequency [133] (mostly at the frequency $2f_2 - f_1$). DPOAEs are linked to the generation of distortion products on the BM. Another type of OAEs, electrically evoked otoacoustic emission (EEOAE), are measured if the ear is stimulated by an electrical AC signal [100]. The understanding of the generation and propagation of OAEs is a very important topic in cochlear mechanics since the measurements of OAEs are used as a noninvasive diagnostic tool in humans.

1.5 The cochlear amplifier

1.5.1 Description

Different researchers have analyzed the experimental data and concluded that the high sensitivity of the BM response to low intensity acoustic stimulation, its nonlinearity and the generation of OAEs can only be explained by the presence of an active mechanism called cochlear amplifier [79, 34, 37, 33]. The cochlear amplifier locally

adds energy to the traveling wave to overcome the energy dissipated by viscous drag in the subtectorial space. The cochlear amplifier has been introduced phenomenologically in some cochlear models by a negative damping term [37, 106] to predict the high sensitivity of the BM. In the active cochlea, a wave travels on the BM until it reaches the passive BP. Close to the BP, the cochlear amplifier adds energy to the traveling wave. Because of this active feedback the BM is very sensitive to low intensity acoustic stimuli. This theory can also predict the presence of OAEs. If the active feedback mechanism is too high, the system can become unstable which could explain the presence of SOAEs. The compressive behavior of the BM as well as the generation of harmonic distortion, distortion products on the BM and DPOAEs would be due to the saturating nonlinearity of the cochlear amplifier.

The identity of the cochlear amplifier is one of the major unresolved debates in cochlear mechanics [4]. The cochlear amplifier has been explained alternatively by two different mechanisms, summarized in Fig. 1.4 and described next: OHC somatic motility combined with HB mechanotransduction or HB motility.

1.5.2 OHC somatic motility

In the prevailing theory of cochlear amplification the active mechanism is located in the main body of the outer hair cells (OHCs). Due to vibrations in the organ of Corti caused by the difference in the pressure of the fluid accross the cochlear partition, the HBs of the OHCs (which are directly connected to the TM) are deflected by the relative shear motion between the TM and the RL. When the HBs are deflected, transduction channels opens and current flows through the OHCs which causes a depolarization of the cell. The main body of OHCs (called soma) has been observed to be electromotile by Brownell in 1984 [10, 11] as it generates a force when it is depolarized, due to the action of the motor molecule prestin [158]. This force can act at high frequencies [43] to amplify the BM and TM motion.

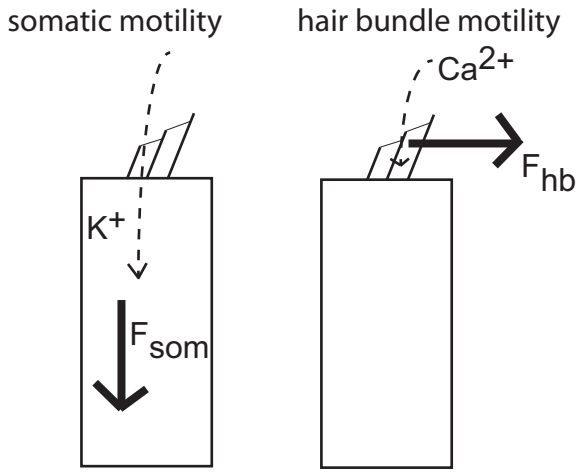

Figure 1.4: The two theories of cochlear amplification. In both theories in response to acoustic stimulation the HB of OHC are deflected and transduction current enters the cell. In the case of somatic motility the presence of potassium causes the main body of the OHC to exert an axial force due to the activity of prestin. In the case of HB motility a calcium binding event closes the transduction channels and generates a force perpendicular to the OHC length.

Some experiments partially validate the theory that somatic motility underlies cochlear amplification. Genetic mutations of prestin in the cochlea of the mouse [87, 46, 32, 16] have given ways to test this theory. The most convincing evidence is with the prestin knock-in mice [32] (these mice do not exhibit somatic motility but have the same passive OHC stiffness as wild-type mice). The cochlea of these mice is less sensitive than the cochlea of wild-type mice, which shows, as claimed by the authors, that prestin-based OHC somatic motility is necessary for cochlear amplification. Perfusion of salicylate in perilymph [141] also shows that somatic motility plays an essential role in cochlear amplification, as salicylate simultaneously alters force production by prestin and reduces the sensitivity of the BM to acoustic stimulation.

One argument against this theory is that the large capacitance and resistance of the basolateral portion of the OHC should act a low-pass filter on the transmembrane voltage [140], with a cutoff frequency of about 1kHz at basal locations [66], much

lower than the CF. Therefore isolated OHC would not be able to produce the force necessary for high frequency cochlear amplification. However theoretical [31, 147, 73] and computational [121, 99] studies have shown that somatic motility might be the cochlear amplifier despite the the basolateral filter. The RC cutoff issue will be analyzed using the computational model of the cochlea developed in this thesis.

1.5.3 HB mechanotransduction and passive HB mechanics

The theory of somatic motility as the cochlear amplifier requires the HB of the OHC to act as a mechanoelectrical transducer. Each HB consists of about 80 stereocilia, organized in three rows of increasing height. The number of transduction channel per stereocilia corresponds approximately to the number of transduction channels [127]. When the HB are deflected, the increase in the tension of an elastic element called gating spring opens the mechanically gated transduction channel [27, 67, 93]. The opening of the channel allows mechano-electrical transduction (MET) to occur. Ionic current (potassium mostly, but also calcium) flows through the channel towards the OHC HB and main body. The MET current is a saturating nonlinear function of the HB deflection. The current reaches its saturating value for a HB deflection of about $1\mu m$ in the mammalian HB in vitro [80]. In the somatic motility theory of cochlear amplification, this saturation of the transduction channel is responsible for the nonlinearity of the cochlear amplifier [108, 90]. Another potential source of nonlinearity is the reduction of the overall stiffness of the HB during channel gating due to mechanism called gating compliance [67].

1.5.4 Active HB dynamics: fast adaptation and HB motility

MET also exhibits a time dependent phenomenon called adaptation that is observed experimentally when the HB are deflected by a flexible or rigid fiber *in vitro*: after an initial rise (due to channel opening) there is a decrease of the current (due to

closing of some of the transduction channels) called adaptation, with two characteristic time constants. Adaptation has been first observed in nonmammalian vertebrates [41, 28] but has recently been discovered in mammals as well [81, 128]. The rate of fast adaptation in the mammalian HB has been measured in a submillisecond time scale [81, 128, 8]; the slower component is in milliseconds [8]. When the HB are deflected by a flexible fiber, force production by the HB can be measured in the mammalian HB simultaneously to the adaptation of the transduction current [80, 8]. Calcium binding to the transduction channel or to an entity closed to the channel has been hypothesized to cause fast adaptation[17, 9, 94]. Slow adaptation and slow force production have been generally assumed to be due to the slipping of a myosin molecule on an actin cytoskeleton [5, 144].

HB motility underlies cochlear amplication in the inner ear of the nonmammalian vertebrate [96]. In these species the HBs have been shown to provide mechanical work on a cycle by cycle basis for small stimuli [95] and to oscillate spontaneously [94] at frequencies of a few Hz in *in vitro* experiments. This has not been observed so far in the mammalian HB but this might be due to the low speed of the experimental techniques. Some authors have claimed that the active HB force could be the mammalian cochlear amplifier [69, 122].

1.6 Mathematical models of the mammalian cochlea

Many computational models of the mammalian cochlea have been developed over the years so as to validate and develop new theories of cochlear mechanics. These models can make predictions than can be compared to measurements or can suggest new experiments. Some models are simple from a theoretical and computational point of view as the fluid in the ducts is reduced to a 1D partial differential equation and the cochlear partition by one degree of freedom, the BM displacement or velocity. For example one series of models from De Boer [75, 74, 77] can make some realistic

predictions of the active and nonlinear stationary response of the cochlea. The advantage of this type of model is the low computational cost and the low number of parameters. However the physics of the cochlea is highly simplified which limits the predictive capacities of these models. Other cochlear models are either fully three dimensional [84, 56] or based on a 1D fluid representation and a model for the organ of Corti micromechanics [2, 15, 14, 91, 108, 48, 49, 52, 105, 104, 90, 68, 148] so as to implement more physiologically relevant mechanisms of cochlear amplification.

The work presented in this thesis is based on the models developed in Professor Grosh's laboratory. Anand Parthasarthi developed the finite element method to simulate the response of the cochlea to acoustic stimulation and a first iteration of the cochlear model [117, 116]. Sriprya Ramamoorthy [120] and Niranjan Deo [38] improved the model to use more physiological models and parameters. The resulting model, described in [121], nicely predicts some of the features of the response of the cochlea to acoustic and electrical stimulation. The model is based on a three dimensional representation of the fluid and includes a micromechanical model of the organ of Corti kinematics. Both somatic motility and mechanoelectrical transduction are linearized so as to predict the active dynamics of the cochlea to low intensity stimuli.

1.7 Motivations and objectives

The mammalian inner ear is an amazing organ that needs to be better understood. The function of the ear is similar to a microphone as it converts sound to an electrical signal. However it has better characteristics than any currently designed microphone. A better understanding of the cochlea might suggest alternative ways to design better microphones or sensors that mimic the mammalian cochlea. Moreover due to our lifestyle and the frequent exposure to potentially harmful sound, as well as to the aging population in developed countries, more and more people suffer from hearing loss (one half of the Americans over 75 years suffer from hearing loss according to

the National Institute of Health). A better understanding of cochlear mechanics is critical to explain the failures of the system (causing deafness) and to find ways to protect and repair hearing.

A mathematical model of the cochlea is used as a tool to test and develop theories of cochlear mechanics. The model predictions can help to validate the existing theories about cochlear mechanics as well as establishing alternative or new theories. In particular, the properties of the mechanical structures and active mechanisms can be easily altered in a mathematical model (contrary to experiments) in order to test their role and effects on cochlear mechanics. This could for example help to design new drugs that could target specific structures or cells of the organ. The active response of the cochlea, both in terms of amplification, distortion and the generation of OAEs is particularly important. The model results could also suggest new experiments or new diagnostic tools for hearing loss.

More specifically, the objective of this work is to pursue the development of a predictive model of the guinea pig cochlea, based on the physiology and physics of the system. The analysis focuses on the basal region of the cochlea and the predictions of more apical locations are for future work. The objectives can be divided into two parts, one on the linear response of the cochlea, and the other on the nonlinear response. For the linear response of the cochlea, the objectives are:

1. To improve the prediction of BM response to low intensity acoustic stimuli. The previous model of the cochlea [121] predicts a too sharply tuned BM response and an impulse response that is too long compared to experimental data. This is an important deficiency of the model as the cochlea needs both to be very sensitive and have a fast transient capture to low intensity stimuli. Introducing structural longitudinal coupling in the model is shown in Chapter III to improve the predictions of the model.

2. Identify the mechanism (somatic motility and/or HB motility) responsible for

the active dynamics of the cochlea. The contribution of the active HB dynamics to cochlear amplification needs to be predicted. A nonlinear model of active HB dynamics (both fast adaptation of the transient current and HB motility) is linearized for small harmonic stimuli and implemented in the macroscopic model of the cochlea in Chapter IV. The effect of the active HB dynamics on cochlear mechanics, as well as of the RC filtering on somatic motility, are analyzed.

The second part of this thesis has for objective the prediction of the nonlinear response of the cochlea to acoustic stimuli. Interesting predictions can be made using a linear model of the cochlea. However some characteristics of the cochlea can only be captured and understood using a nonlinear model:

1. A computationally efficient methodology is used to compute the stationary response of the cochlea to a single tone in Chapter V. The prediction of a realistic compressive response of the BM and well as harmonic distortion validate the previously developed linear approach.

2. The same computational method is used to predict the response to two tones in Chapter VI. The mechanisms underlying two tone suppression and distortion product generation are analyzed.

CHAPTER II

Linear frequency domain model of the cochlea

2.1 Introduction

The computational model of the guinea pig cochlea described in this chapter is based on Ramamoorthy *et al.* [121]. The main addition to the previous model is the addition of structural longitudinal coupling to the BM and TM so as to predict a more broadly tuned BM response to low intensity acoustic stimulation and a shorter impulse response (see Chapter III). The parameters have been changed to use more physiological values and to improve the predictions of the model. This model is also used as a basis for the investigation of the role of HB motility and fast adaptation of the transduction current in cochlear amplification (see Chapter IV). A nonlinear version of the cochlear model is used in Chapters V and VI.

The model of the cochlea includes the fluid (with a three dimensional representation), the structure (with a model for the organ of Corti that includes the BM, and a bending and a shearing mode for the TM) and electrical degrees of freedom (to represent the potentials in the scalae of the cochlea). The structural and electrical degrees of freedom are coupled via somatic motility and HB mechanoeletrical transduction. For completeness, all the elements of the cochlea (included those developed previously) are described briefly in this chapter. A time dependence $exp(-i\omega t)$ is used.

2.2 Structural model and fluidic model

The subsections about the basilar membrane and membrane have been reproduced with permission from Meaud, J. and Grosh, K., Journal of the Acoustical Society of America, 127, p1411-1421, (2010). Copyright 2010, Acoustical Society of America.

2.2.1 Basilar membrane

The BM is an anisotropic and inhomogenous structure, with collagen fibers running in the radial direction [146]. Von Bekesy [7] observed that longitudinal coupling appears to be significant in the BM of dead animals. However in a later study in live guinea pigs Voldrich [156] found that longitudinal coupling in the BM is negligible. Therefore many researchers have modeled the BM as a locally reacting structure [15, 49, 91, 106, 121]. More recent measurements in the cochlea of the mongolian gerbil [101] quantifies longitudinal coupling in the BM and organ of Corti and indicates that longitudinal coupling is significant and increases from the base to the apex of the cochlea. Liu and White [89] used the published experimental data to compute the material properties of the BM described by an orthotropic plate model (and used as a basis for the parameters of the BM, shown in Table B.1. The governing equation for the BM motion modeled as an orthotropic plate is:

$$\begin{aligned} P_{bm}(x,y) =& \frac{2}{b} C_{bm}\dot{u}_{bm} + M_{bm}\ddot{u}_{bm} \\ & - \frac{\partial^2}{\partial x^2}\Big(D_{xx}\frac{\partial^2 u_{bm}}{\partial x^2} + D_{xy}\frac{\partial^2 u_{bm}}{\partial y^2}\Big) - 2\frac{\partial^2}{\partial x \partial y}\Big(D_s \frac{\partial^2 u_{bm}}{\partial x \partial y}\Big) \\ & - \frac{\partial^2}{\partial y^2}\Big(D_{yy}\frac{\partial^2 u_{bm}}{\partial y^2} + D_{xy}\frac{\partial^2 u_{bm}}{\partial x^2}\Big) \end{aligned} \tag{2.1}$$

where P_{bm} is the pressure applied by the fluid and the OHC on the BM [121], C_{bm} is the BM viscous damping per unit area, M_{bm} is the mass of the BM per unit area, b is the width of the BM (see Fig. 1.1) and $u_{bm}(x,y)$ the BM displacement. D_{xx}, D_{yy} , D_{xy} and D_s are the orthotropic plate bending stiffnesses of the BM. The locally reacting

model of the BM used in the previous cochlear model [121] (and for comparison in Chapter III) corresponds to Eq. 2.1 when $D_{xx} = D_{xy} = D_s = 0$.

Cooper observed that the radial profile of the BM deformation in response to acoustic stimulation is similar to a simply supported beam mode shape [21], despite the BM inhomogeneity, the fluid loading and the presence of OHCs and other structures. Therefore, as in Ramamoorthy *et al.* [121], we approximate the BM displacement by a simply supported mode shape: $u_{bm}(x, y) = u^0_{bm}(x) \times \sin(\frac{\pi(y+\frac{b}{2})}{b})$ for $-\frac{b}{2} \leq y \leq \frac{b}{2}$, where b is the width of the BM. The radial dependence is integrated out (see [116]). The width of the BM, b, and the thickness of the BM, t, vary as a function of x and are based on the measurements from Fernandez [42] in the cochlea of the guinea pig. The values of the BM parameters are listed in Table B.1.

2.2.2 Tectorial membrane

The TM is a gelatinous structure with three different noncollageneous glycoproteins (α-tectorin, β-tectorin and otogelin). β-tectorin is an essential structural component providing longitudinal coupling in the TM (as shown by Ghaffari [54]). A mouse with genetically modified β-tectorin exhibits an enhanced tuning and reduced sensitivity in the BM response in the high frequency region [137], which suggests that the TM plays a key role in tuning and that TM longitudinal coupling is important for cochlear mechanics. The mechanical properties of the TM have been measured in gerbils [161, 129] and in guinea pigs [145, 47] as well as in mice [1, 58, 57]. The measurements in [57] show that the TM has frequency dependent properties. Moreover, although direct comparison between different measurements is difficult because of the difference in the experimental methods, the data shows that the TM of mice (that have a higher frequency range than guinea pigs) is much stiffer than the TM of the guinea pigs and gerbils (that have a lower frequency range than guinea pigs). Zwislocki and Cefaratti found that the TM is significantly less stiff than the HBs

[161] in the gerbil cochlea. However some more recent measurements led to contradictory conclusions about the relative stiffness of the TM (which in turn influences the kinematics). Some studies in the mouse cochlea have found that the TM is significantly stiffer than the HB [1, 57]. If this is the case, then the TM would then move as rigid body from the limbal attachment provided that the TM region near the spiral limbus is more compliant than the main body of the TM (see [121]). Recent measurements in the gerbil and guinea pig cochlea found that the TM has a stiffness within an order of magnitude of the HB [145, 129]. In this case, the TM would then deform elastically from the limbal attachment (if the limbal attachment is stiffer than the TM, as suggested by [58, 47]). Richter *et al.*[129] showed that the TM stiffness varies longitudinally with a higher radial stiffness at basal locations than at more apical locations. Shoelson *et al.*[145] did not observe the presence of a stiffness gradient in the TM of the guinea pig but observed a longitudinal and radial inhomogeneity. Estimates of the shear modulus and Young's modulus were derived in [129] and [145] based on an isotropic model of the TM. As noted in these papers some caution must be taken in interpreting these results because of the isotropic and homogenous assumptions of the model. Because of its microstructure the TM is anisotropic as shown by Gavara and Chadwick [47] using atomic force microscopy measurements of the elastic moduli. Ghaffari *et al.* [55] demonstrated that the TM isolated from the mouse cochlea is capable of supporting shear waves that propagate in the longitudinal direction of the cochlea (see Fig. 2.1). Such waves would not be possible without significant longitudinal stiffness in the TM. While the mechanical properties of the TM estimated from these experiments are somewhat different with those from Chadwick's group [47], both estimates of modulus are consistent with a slow shear wave whose phase velocity is comparable to that of the traveling wave in the cochlea near the frequency-dependent peak response location.

As shown in Fig. 2.1, each cross section of the TM is modeled as a two degree of

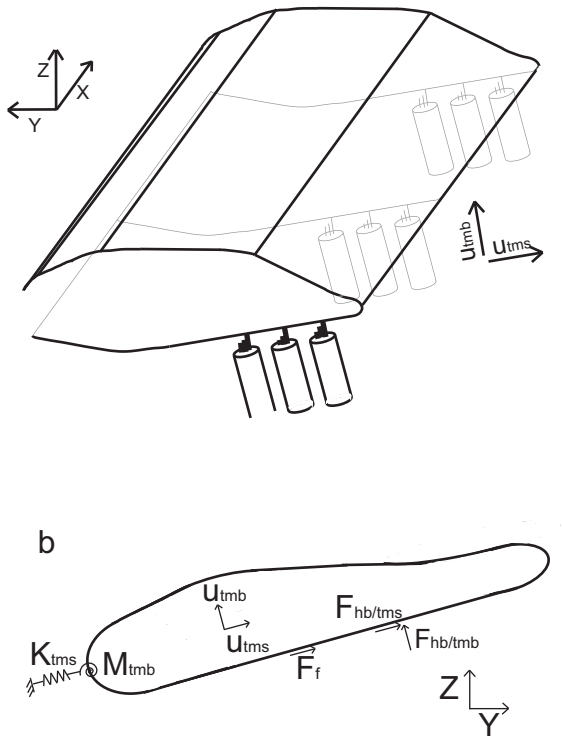

Figure 2.1: Illustration of the TM model. (a) Three dimensional model of the TM. The x-coordinate corresponds to the longitudinal direction. (b) Cross-sectional view of the TM showing external forces (per unit length) acting on the TM. The HBs apply forces in the shear ($F_{hb/tms}$) and bending ($F_{hb/tmb}$) directions. Fluid forcing due to the viscous fluid interaction in the subtectorial space is given by a force ($F_f = C^f_{sub}\dot{u}_s$) in the shear direction proportional to the relative shear velocity between the TM and the RL, $\dot{u}_s$. The TM elasticity in the cross section is modeled by a linear spring (K_{tms}) applying a force in the shear direction and a rotational spring (M_{tmb}) applying a force in the bending direction. The plane sections ($y-z$) shear relative to one another. As in Ghaffari *et al.* [55], internal viscous ($A^{eff}_{tm}\eta_{xy}\frac{\partial \dot{u}_{tms}}{\partial x}$) and elastic ($A^{eff}_{tm}G_{xy}\frac{\partial u_{tms}}{\partial x}$) coupling is included.

freedom system with deformation in the radial or shear direction (u_{tms}) and in the normal or bending direction (u_{tmb}). The TM is characterized at each $(y-z)$ plane by its effective stiffness and mass per unit length. The bending and shear motion varies in the longitudinal direction (x) and hence the cross-sections move relative to one another. Longitudinal viscoelastic coupling of the shear motion of the TM is included (with a shear modulus G_{xy} and a shear viscosity η_{xy}) while TM bending rigidity is neglected. The governing equation for the shear motion of the TM is:

$$\begin{aligned} F_{hb/tms}(x) =& K_{tms}u_{tms} + C^f_{sub}\dot{u}_s + M_{tms}\ddot{u}_{tms} \\ & - \frac{\partial}{\partial x}\Big(A^{eff}_{tm}G_{xy}\frac{\partial u_{tms}}{\partial x} + A^{eff}_{tm}\eta_{xy}\frac{\partial \dot{u}_{tms}}{\partial x}\Big) \end{aligned} \tag{2.2}$$

where $F_{hb/tms}$ is the external force (per unit length) applied by the HB of the OHC in the shear direction [121], C^f_{sub} is the damping coefficient due to the viscosity of the fluid in the subtectorial space, u_s is the relative shear displacement between the TM and the RL, and A^{eff}_{tm} is an effective cross-sectional area of the TM. Because of its inhomogeneity [145], anisotropy [47] and of its frequency dependent properties [1, 57] it is difficult to estimate the values for the effective TM shear stiffness and mass. Here we chose the TM stiffness per unit length, K_{tms}, based on the values published by Richter *et al.* [129] for the radial TM stiffness of the gerbil (as discussed in Appendix A). Hence the TM stiffness is within one order of magnitude of the HB stiffness published in [150]. For the TM shearing mass, we take into account the longitudinal variation observed in the TM cross section area in [129] and choose the value to fit the predictions of the BM response to acoustic stimulation with published experimental data. As in [121], the governing equation for the TM bending motion is:

$$F_{hb/tmb}(x) = K_{tmb}u_{tmb} + C_{tmb}\dot{u}_{tmb} + M_{tmb}\ddot{u}_{tmb}, \tag{2.3}$$

where $F_{hb/tmb}$ is the external force (per unit length) applied by the HB of the OHC

in the bending direction [121], C_{tmb} is the structural damping coefficient of the TM bending mode, K_{tmb} and M_{tmb} are the stiffness and mass per unit length of the TM bending mode. The values of the TM parameters are listed in Table B.2.

2.2.3 Organ of Corti kinematics

The BM mode, the TM bending and shearing modes are linked by the kinematics of the organ of Corti. The pillar cells and Deiter's cells are assumed to be rigid links. The pillar cells rotates around the BM attachment point. The RL lamina is modeled as ridid beam rotating around the attachment to the pillar cells with a rotational spring (with an equivalent stiffness per unit lenth, K_{rl}). With this assumption, the model of the organ of Corti kinematics can be represented by Fig. 2.2. More details about the model for the kinematics can be found in [38, 121].

2.2.4 Passive hair bundle model

As in [38, 121], the effect of mechanoelectrical transduction (gating compliance [67]) and fast adaptation (HB motility) on the HB mechanics is not included. The HB is modeled by a linear stiffness, K_{hb}. The equation for the force applied by the HB on the TM and RL is:

$$(F_{hb})_j = K_{hb} L_{hb} \theta_{hb/rl_j} \tag{2.4}$$

where L_{hb} is the length of the HB and θ_{hb/rl_j} is the rotation of the HB relative to the RL, given by:

$$\theta_{hb/rl_j} = \frac{u_{hb_j}}{L_{hb}} + \frac{u_{rl_j}}{L_{R_0} - \delta_j L_1} \tag{2.5}$$

where u_{hb_j} is the shear displacement of the apical end of the HB relative to its basal end and u_{rl_j} is the displacement of the RL at the attachment of the HB relative to the displacement of the RL at its pivot point (as in [121], and $\delta_j = 1$ if $j = 1$, =0 if $j = 2$ and =-1 if $j = 3$.

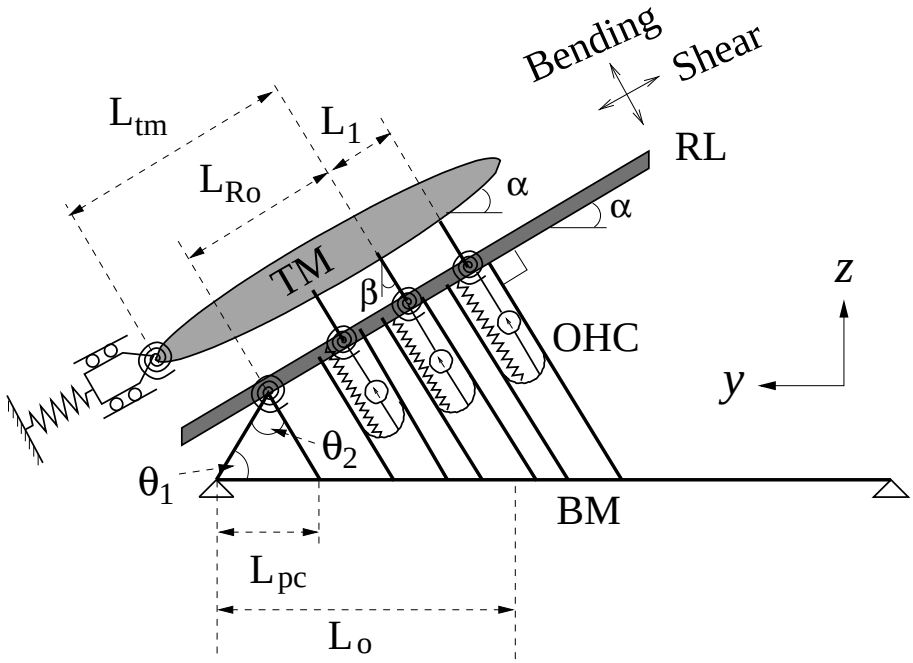

Figure 2.2: Organ of corti kinematics. The BM mode and the TM radial and bending modes are linked by the organ of Corti. The reticular lamina rotates as a rigid beam abound its attachment to the top of the pilar cells. The HB of the OHC rotates around their attachment point at the RL and the TM. The OHCs can compress or elongate along their length. Reprinted with permission from Ramamoorthy S, Deo, N.V. and Grosh, K., Journal of the Acoustical Society of America, 121, 2758–2773, (2007). Copyright 2007, Acoustical Society of America.

The stiffness of the mammalian HB has been measured *in vitro* [151, 80, 8]. Although the stiffness of the HB was measured with a large deflection (about $1\mu m$, which could damage the HB) by Strelioff [151], the values in the simulation is based on his measurements because it is the only measurement in the guinea pig and because the stiffness was measured at different longitudinal locations.

2.2.5 Fluid and fluid/structure interaction

The fluid in the cochlear duct is modeled as inviscid and incompressible and is governed by the Laplace equation:

$$\nabla^2 P = 0 \tag{2.6}$$

Rigid wall boundary conditions are used for the bony walls of the cochlea. The fluid is coupled to the stapes, to the oval window and to the BM via the linearized Euler equation:

$$\nabla P = -i\rho_f \omega V_f \tag{2.7}$$

where ρ_f is the density of the fluid and V_f is the velocity of the fluid (which is equal to the velocity of the structure at the interface). To limit the computational cost, the fluid pressure is decomposed into three symmetric radial mode shapes: $\psi_n(y) = \cos(\frac{n\pi(y+w/2)}{w})$ $(n = 1, 3, 5)$ for $-\frac{w}{2} \leq y \leq \frac{w}{2}$, where w is the width of the duct. The radial dependence is integrated out (see [117]).

2.3 Electrical model and electrical/structural coupling

2.3.1 Electrical model

At each cross section, four degrees of freedom represent the fluctuating part (AC) of the potential in the scala vestibuli (ϕ_{sv}), the potential in the scala media (ϕ_{sm}),

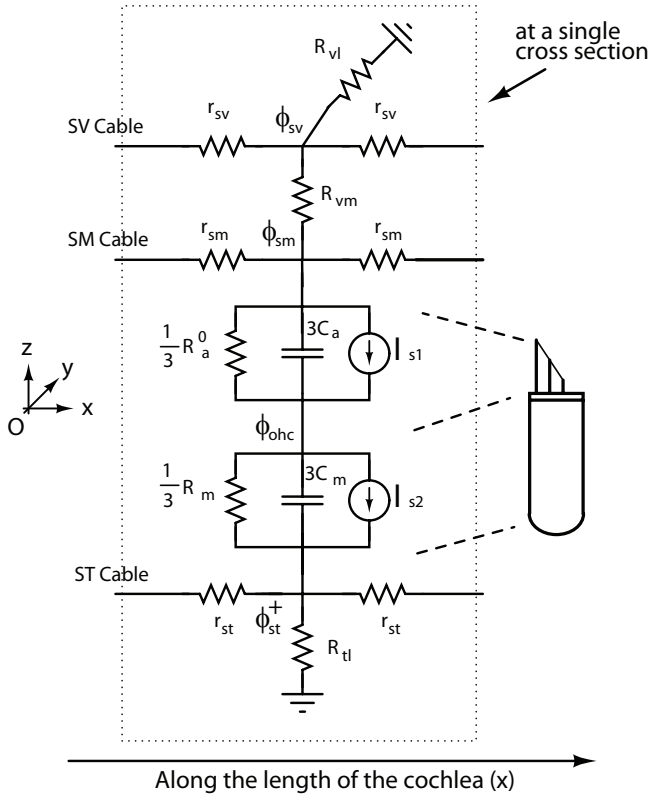

Figure 2.3: Electrical model. At each cross section four degrees of freedom represent the scala vestibuli, scala media, OHC and scala tympani potentials. Longitudinal cables connect the different cross section to model propagation of current along the length of the cochlea. The OHC are represented by an electrical circuit with an apical part (with a conductance proportional to the HB deflection to model mechanotransduction) and basolateral part (with a current source to account for somatic electromechanical coupling). Reprinted with permission from Ramamoorthy S, Deo, N.V. and Grosh, K., Journal of the Acoustical Society of America, 121, 2758–2773, (2007). Copyright 2007, Acoustical Society of America.

the intracellular outer hair cell potential (ϕ_{ohc}) and potential in the scala tympani (ϕ_{st}). The potential in the three scalae are connected by electrical cables to model longitudinal progagation of current in the scalae. Two current sources are included to model HB conductance changes with HB deflection and OHC somatic motility, as described next. The electrical model can be represented by Fig. 2.3. The equations governing the electrical degrees of freedom are then obtained using the Kirchoff laws, as described in [38, 121].

2.3.2 Outer hair cell somatic motility

The properties of somatic motility (the OHC stiffness and capacitance) are nonlinear function of the OHC transmembrane voltage [61]. However, based on experimental [85] and theoretical observations [108, 90], the physiologically relevant variations in the transmembrane voltage are assumed to be small under acoustic stimulation. Therefore, based on the model developed in [154, 39], each OHC is modeled (as in the previous model of the cochlea [38, 121]) by linearized piezoelectric-like expressions relating the OHC deformation, $u_{ohc_j}^{comp}$, and fluctuating part of the transmembrane voltage, $\Delta\phi_{ohc_j}$, to the OHC force (per unit length), F_{ohc_j}, and current (per unit length), I_{ohc_j}:

$$F_{ohc_j} = K_{ohc}\, u_{ohc_j}^{comp} + \epsilon_3\, \Delta\phi_{ohc} \tag{2.8}$$

$$I_{ohc_j} = \frac{\Delta\phi_{ohc}}{Z_m} + i\omega\epsilon_3\, u_{ohc_j}^{comp}. \tag{2.9}$$

where K_{ohc} is the OHC stiffness (per unit length), ϵ_3 is the electromechanical coupling coefficient (per unit length), Z_m is the basolateral impedance of the OHC, and the subscript ohc_j refers to each OHC where j corresponds to the row number, $j = 1, 2, 3$.

2.3.3 Mechanoelectrical transduction

The model for HB mechanoelectrical transduction for the simulations of Chapter III is described here. In contrast to the MET channel model in [38, 121], the transduction current depends here on the rotation of the HB relative to the RL instead of the relative shear deflection of the HB. The transduction current is proportional to the open probability of the transduction channel. The effect of adaptation of the transduction current of mechanotransduction [81, 128] is not modeled. According to the gating spring theory of mechanoelectrical transduction [67, 93], the open probability

can be modeled by the following Boltzman function:

$$P_{0_j} = \frac{1}{1 + \exp\left[- \frac{f_{gs}\gamma L_{hb}\theta_{hb/rl_j}}{k_B T} \right]} \tag{2.10}$$

where f_{gs} is the single channel gating force, γ is the geometrical gain factor (relating the displacement in the tip link direction to the displacement at the top of the HB), k_B is the Boltzman constant and T is the temperature and θ_{hb/rl_j} is the rotation of HB relative to the RL. In the linear model of the cochlea, the transduction current is linearized with respect to the HB deflection for small HB deflections. The linearized expression for the HB conductance change, δG_{a_j}, for a small HB rotation relative to the RL, $\delta\theta_{hb/rl_j}$ is:

$$\delta G_{a_j} = \frac{\partial G_a}{\partial \theta_{hb/rl}} \delta\theta_{hb/rl_j} = G_a^{max} \frac{f_{gs}\gamma}{k_B T} P_0^s (1 - P_0^s) L_{hb} \delta\theta_{hb/rl_j} \tag{2.11}$$

where G_a^{max} is the maximum saturating conductance of the HB and P_0^s is the resting open probability. In response to a larger HB deflection the transduction channel saturates. The HB conductance change ΔG_{a_j} in response to a large HB rotation $\Delta\theta_{hb/rl_j}$ is given by:

$$\Delta G_{a_j} = Act \times G_a^{max} \frac{f_{gs}\gamma}{k_B T} P_0^s (1 - P_0^s) L_{hb} \Delta\theta_{hb/rl_j} \tag{2.12}$$

where Act is a number between 0 and 1. In response to acoustic stimulation the HB deflection is a function of the longitudinal location x. Hence Act should be a function of x. However, as previously [121], Act is considered to be independent of x for the simulations. The response of the cochlea to moderate or high intensity is simulated using the linear model of the cochlea with the following expression for the

transduction current:

$$(I_{hb})_j = (G_a^0 - i\omega C_a)(\phi_{sm} - \phi_{ohc}) + Act \times (V_{sm} - V_{ohc})\frac{G_a^{max} f_{gs}\gamma}{k_B T} L_{hb}\Delta\theta_{hb/rl_j} \quad (2.13)$$

where $(G_a^0 - i\omega C_a)$ is the passive electrical impedance of the apical part of the OHC, $(V_{sm} - V_{ohc})$ is the resting transmembrane potential and Act is a number between 0 and 1 that is called "activity level". The validity of this linearized approach to model the response of the cochlea to moderate or intense stimuli will be discussed in Chapter V.

The parameters of the HB mechanoelectrical transduction are G_a^{max}, γ, f_{gs} and P_0^s. The best estimate of the saturating conductance, G_a^{max}, is the measurement by He [63] in the hemicochlea. He measured a conductance of $34.7nS$ for a basal HB in the adult gerbil hemicochlea and $17.3nS$ for a more apical HB. The experimental values must be corrected to account for *in vivo* conditions including a lower *in vivo* calcium concentration (a factor of 3 [63]), higher temperature (a factor of 1.6 assuming a Q_{10} around 1.3 [81]) and potassium as opposed to the sodium based endolymph for experiment (a factor of 1.25 [81]) for a six-fold increase of the conductance to a value of $208nS$. Even higher *in vivo* values of G_a^{max} are expected for two reasons. First, as shown in Fig. 2c in [63], they were not able to completely saturate the current in their most sensitive cells because of constraints on the maximum displacement to maintain a tight seal for the patch clamp. So larger *in vitro* currents and conductances are possible. Second the hemicochlear preparation likely induces some damage to the OHC; damage that would reduce the maximum current measured. Based on the dimensions of the HB and of a finite element model of the HB, Nam [103] predicted the geometrical gain factor to be about 0.25 for a basal HB and 0.11 for an apical HB. The single channel gating force can be estimated based on measurements of the response of the transduction channel to HB deflection. Published values for the mammalian HB are about

5pN [155, 8]. The transduction channel and therefore the cochlear amplifier would have the maximum sensitivity if the transduction channel resting probability is 0.5 *in vivo*. Two sets of experimental data [160, 20] suggest that the resting probability slightly deviates from its optimal value (0.5); a value of 0.4 is used for the simulations.

2.4 Linear finite element formulation

A Bubnov-Galerkin finite element method [70, 117] is used to discretize and solve the equations. The radial dependence for the BM and fluid equations is first eliminated by integration of the assumed radial mode shapes. The weak form is then derived from the strong form of the equations. With the modal decomposition the three dimensional model is reduced to a series of 2D models which can then be post-processed to synthesize the full result. In this study, a discretization of 741 nodes in the longitudinal direction (x) and 41 nodes in the z-direction was used (this was determined to be sufficiently converged for our purposes [117]). Linear shape functions are used for the TM shear and bending displacements and for the electrical degrees of freedom. Bilinear shape functions are used for the fluid. Hermitian shapes functions are used for the BM displacement (due to the higher order of the BM governing equation). The resulting matrix equation has the form:

$$\begin{bmatrix} \mathbf{K_f} & \mathbf{Q_{fs}} & \mathbf{0} \\ \mathbf{Q_{sf}} & \mathbf{K_s} & \mathbf{Q_{se}} \\ \mathbf{0} & \mathbf{Q_{es}} & \mathbf{K_e} \end{bmatrix} \begin{pmatrix} \mathbf{p} \\ \mathbf{u} \\ \phi \end{pmatrix} = \begin{pmatrix} \mathbf{f_f} \\ \mathbf{0} \\ \mathbf{0} \end{pmatrix}. \tag{2.14}$$

where K_f is the fluid stiffness matrix, K_s is the structural stiffness matrix, K_e is the electrical stiffness matrix, $Q_{sf} = Q_{sf}$ are the fluid/structure coupling matrix, Q_{se} is the structural-electrical coupling matrix, Q_{es} is the electrical-structural coupling matrix and f_f is the fluid forcing due to the vibrations of the stapes. Note that

$Q_{se} \neq Q_{es}$ (because of the current source due to the MET channel) and therefore the matrix of the system is not symmetric. The finite element formulation is coded in Fortran 90.

CHAPTER III

Role of structural longitudinal coupling in cochlear mechanics

3.1 Introduction

Most mathematical models of the cochlea, including [38, 121], consider the structure to be locally reacting. For example, in [121], the only sources of longitudinal coupling are the fluid and the longitudinal electrical cables; the different cross-sections of the BM and of the TM do not interact directly ($G_{xy} = 0$ and $\eta_{xy} = 0$ for the TM in Eq. 2.2, and $D_{xx} = D_{xy} = D_s = 0$ for the BM in Eq. 2.1). The previous model [121] predicts the high sensitivity of the BM to low intensity acoustic stimulation. However the tuning of the BM response is predicted to be much sharper than in experimental data. Moreover the duration of the impulse response is much longer than in measurements. In this chapter it is shown that adding structural longitudinal improves the model predictions.

This chapter has been reproduced with permission from Meaud, J. and Grosh, K., Journal of the Acoustical Society of America, 127, p1411-1421, (2010). Copyright 2010, Acoustical Society of America. The article has been edited to follow the logical order of this thesis.

Table 3.1: Mechanical quality factor (Q_{10dB}) and CF in the different models and in the experimental data.

Model	Q_{10dB}	CF
LR	15.2	16.7Hz
TM-LC	7.0	16.2kHz
BM-LC	9.2	17.5kHz
TMBM-LC	5.7	16.6kHz
Experimental data [159]	6.5	16.5kHz

3.2 Effect of structural longitudinal coupling on the model predictions

In this section the predictions of the response of the cochlea to acoustic stimulation with four different combinations for the TM and BM model are compared so as to predict the effect of longitudinal coupling in active cochlear mechanics. In the first (results shown with a thin solid line in Figs. 3.1, 3.2 and 3.3), a locally reacting model of the TM and of the BM (denoted as the LR model) is used. By this we mean that there is no longitudinal mechanical coupling in the TM or the BM (as in Ramamoorthy *et al.*[121]). The fundamental components of the second model (denoted as the TM-LC model) are identical to the first, except that longitudinal coupling is now included in the representation of the TM according to Eq. 2.2 (results shown with a thick dashed line). In the third model (denoted as BM-LC model), longitudinal coupling is introduced in the BM according to Eq. 2.1 (results shown with a thin dashed line). In the fourth model (denoted as TMBM-LC model), longitudinal coupling is included in both the TM and the BM (results shown in thick solid line). In order to achieve the same BM gain at the characteristic frequency (CF) for the four models, the electromechanical coupling factor of the OHC (ϵ_3 in Eq. 2.9) for the TM-LC, BM-LC and TMBM-LC are respectively about 69%, 27% and 79% higher than for the LR model.

3.2.1 Frequency response of the BM

In Fig. 3.1, frequency domain model predictions of the gain in basilar membrane (BM) velocity relative to the stapes velocity at a basal location ($x = 0.4$cm) with and without longitudinal coupling in the TM and/or in the BM are compared. As shown in Fig. 3.1 and Table 3.1, the LR predicts a high mechanical quality factor ($Q_{10dB} = 15.2$). In the BM-LC model the Q_{10dB} is reduced ($Q_{10dB} = 9.2$). The TM-LC model predicts that the Q_{10dB} ($Q_{10dB} = 7.0$) is much lower than in the LR model and lower than in the BM-LC model. The Q_{10dB} predicted by the TMBM-LC ($Q_{10dB} = 5.7$) is slightly lower than that by the TM-LC model. Longitudinal coupling has a small effect on the CF for a given location. Longitudinal coupling in the TM slightly reduces CF (by about 4%) while longitudinal coupling in the BM slightly increases the CF (by about 5%), as shown in Fig. 3.1 and in Table 3.1. For reference, the magnitudes of the BM gain predicted by the four models with no activity ($Act = 0$) are shown in Fig.3.2. The passive response predictions are almost indistinguishable. The passive LR model is slightly more sensitive than the other models (by less than 2dB).

The prediction for the phase of the BM relative to the stapes in the active models is shown as a function of frequency in Fig. 3.3. In the LR model (shown with a thin solid line) the phase accumulation at high frequency is about 8 cycles while it is only about 5 to 6 cycles in the other three models. The absolute value of the slope of the phase in the LR model and of the BM-LC model (shown with a thin dashed line) is higher than in the TM-LC (shown with a thick dashed line) and TMBM-LC (shown with a thick solid line) models. Hence models with longitudinal coupling in the TM have a different behavior than those with no longitudinal coupling or coupling in the BM only.

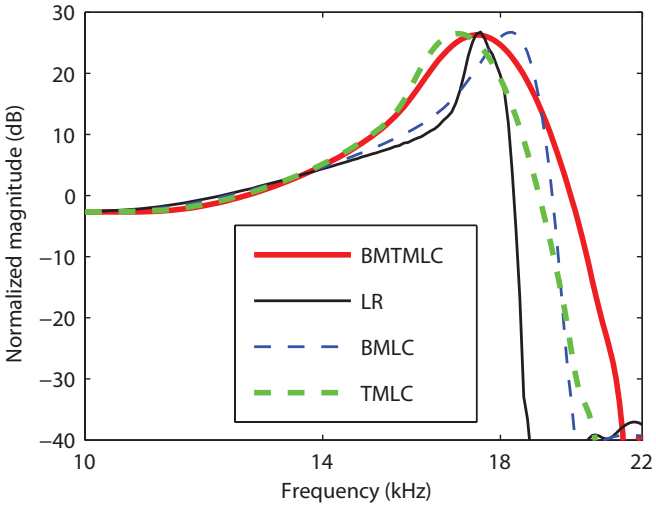

Figure 3.1: Effect of longitudinal on the BM gain. The model preditions for the BM gain in the active case (80% activity) are plotted as a function of frequency. As in Ramamoorthy *et al.* [121], the gain is normalized to the maximum passive model gain. Thin solid line: active LR model response. Thick dashed line: active TM-LC model response. Thin dashed line: active BM-LC model response. Thick solid line: active TMBM-LC model response. The values for $\epsilon_3(x)$ for the different models are given in Table B.5. The four models are capable of predicting realistic maximum gains but at these activity levels the Q_{10dB} for the LR and BM-LC models are always much higher than that predicted by the TM-LC and TMBM-LC models.

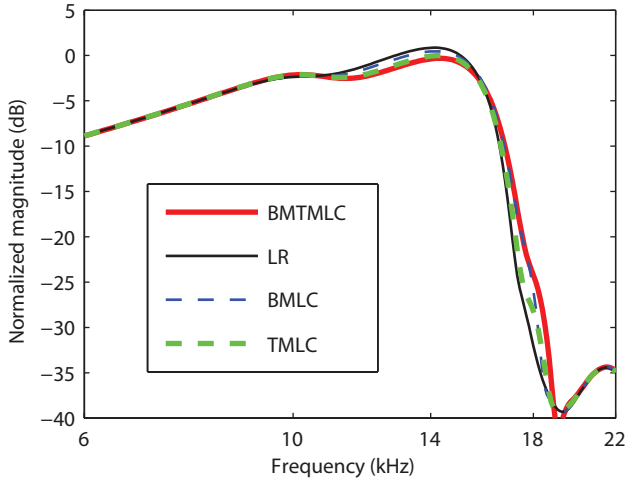

Figure 3.2: Effect of BM longitudinal coupling of the passive predictions. The model preditions for the BM gain in the passive case (0% activity) are plotted as function of frequency. As in Ramamoorthy *et al.* [121], the gain is normalized to the maximum passive gain. Thin solid line: passive LR model response. Thick dashed line: passive TM-LC model response. Thin dashed line: passive BM-LC model response . Thick solid line: passive TMBM-LC model response. The effect of longitudinal coupling (in the BM or in the TM) is not significant on the passive BM frequency response.

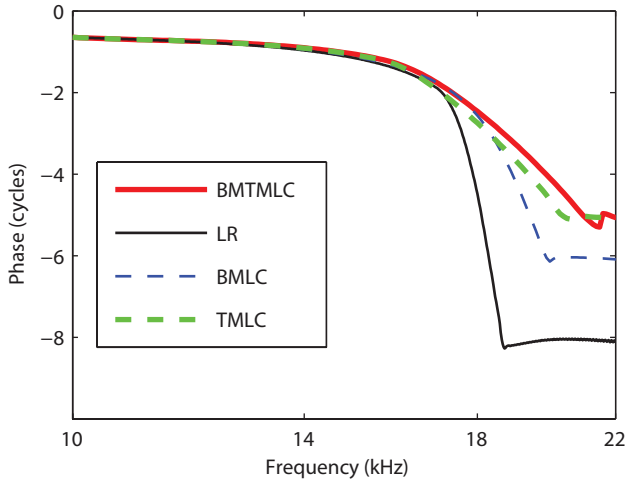

Figure 3.3: Effect of longitudinal coupling on the phase predictions. The model preditions for the BM phase relative to the stapes in the active case (80% activity) are plotted as function of frequency. Thin solid line: active LR model response. Thick dashed line: active TM-LC model response. Thin dashed line: active BM-LC model response. Thick solid line: active TMBM-LC model response.

3.2.2 Uncoupled structural longitudinal coupling space constants

The effect of TM and BM longitudinal coupling on the acoustic response of the BM can be explained by the evaluation of the space constants for the shear motion of the TM and the transverse motion of the BM uncoupled from the other structures and the fluid. The analysis of these predictions allows to estimate the spatial extent of a single row of OHC forcing due to longitudinal mechanical coupling in the TM and BM.

The TM is attached to the reticular lamina by 3 rows of HBs (each with a stiffness per unit length K_{st}) and to the spiral limbus (with a stiffness per unit length K_{tms}). The force applied by the HB on the TM in the shear direction is given by $F_{hb/tms} = -3K_{st}u_s$. Therefore, according to Eq. 2.2, if the longitudinal variations of A_{tm}, G_{xy} and η_{xy} are locally neglected, the complex wavenumber characteristic of TM longitudinal coupling, k_{tms}, is given by:

$$k_{tms} = \Big(- \frac{K_{tms} + 3K_{st} - c_{tms}i\omega - M_{tms}\omega^2}{A_{tms}(G_{xy} - i\omega\eta_{xy})} \Big)^{1/2} \tag{3.1}$$

If we integrate out the radial dependence of the BM displacement and neglect locally the longitudinal variations of b and of the basilar membrane properties, the BM governing equation is reduced to:

$$\begin{aligned} F_{bm}(x) &= C_{bm}\dot{u}^0_{bm}(x) + \frac{b}{2}M_{bm}\ddot{u}^0_{bm}(x) \\ &\quad -\frac{b}{2}\Big[D_{xx}\frac{\partial^4 u^0_{bm}}{\partial x^4} - 2(D_{xy}+D_s)(\frac{\pi}{b})^2\frac{\partial^2 u^0_{bm}}{\partial x^2} + D_{yy}(\frac{\pi}{b})^4 u^0_{bm}\Big], \end{aligned} \tag{3.2}$$

where F_{bm} is the force per unit length applied by the pressure and the OHC [121]. The complex wave number characteristic of BM longitudinal coupling, k_{bm}, is solution

of the following equation:

$$D_{xx}k_{bm}^4 + 2(\frac{\pi}{b})^2(D_{xy} + D_s)k_{bm}^2 + D_{yy}(\frac{\pi}{b})^4 - M_{bm}\omega^2 - \frac{2}{b}C_{bm}i\omega = 0 \tag{3.3}$$

The space constants characteristic of structural longitudinal coupling are then given by:

$$\lambda_{tms} = \frac{1}{|Imag(k_{tms})|} \text{ and } \lambda_{bm} = \frac{1}{|Imag(k_{bm})|} \tag{3.4}$$

where $Imag$ represents the imaginary part of the complex wave number.

The predictions of the space constants for BM longitudinal coupling and TM longitudinal coupling (given by Eqs. 3.1, 3.3 and 3.4) as a function of the frequency (normalized to CF) are shown in Fig. 3.4. These equations represent the effect of the two structures in isolation from the fluid and other structures. Even though the two constants are similar at low frequencies, the space constant characteristic of TM longitudinal coupling is more than three times higher close to CF. The TM resonance frequency is close to the CF whereas the BM resonance frequency is much higher. Hence TM longitudinal coupling couples a higher number of OHC. Longitudinal coupling with a space constant λ can be considered significant over a distance of about $5 \times \lambda$ [102]. Hence, at CF the TM longitudinal coupling can couple about 30 rows of OHC and the BM longitudinal coupling can only couple about 10 rows of OHCs. Therefore, as seen in Fig. 3.1, the presence of TM longitudinal coupling has a more significant impact on the BM response than the presence of BM longitudinal coupling.

Our results (Figs. 3.1, 3.3 and 3.4) show that the dominant source of structural longitudinal coupling in the cochlea is the TM viscoelasticity. Our goal is to develop a mathematical model of the cochlea that is as simple as possible but can accurately predict the measurements of the BM response. Hence in the following results only the TM-LC model is used.

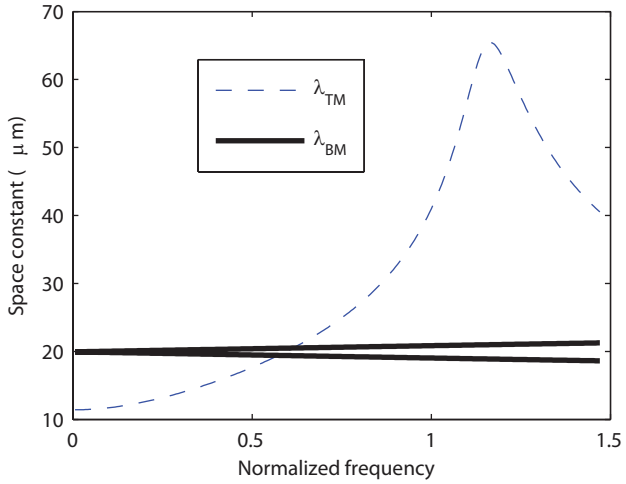

Figure 3.4: Space constants characteristic of BM longitudinal coupling (λ_{BM}) and TM longitudinal coupling (λ_{TM}). The space constants are plotted as a function of the frequency (normalized to the CF). For BM longitudinal coupling there are two space constants because the Eq. 3.3 is quadratic in ${k_{bm}}^2$. At low frequencies the space constants for the BM and the TM are similar (about $20\mu m$ for the BM and $12\mu m$ for the TM). But close to CF, the space constants characteristic of TM longitudinal coupling is more than three times as high as the space constant characteristic of BM longitudinal coupling.

3.2.3 Parameter sensitivity

TM longitudinal coupling is characterized by the shear modulus (G_{xy}) and shear viscosity (η_{xy}) coefficients. Ghaffari et al. [55] determined the longitudinal shear modulus (G_{xy}) and shear viscosity (η_{xy}) using a mathematical model of the TM similar to what we propose and their measurements of the shear traveling wave in a mouse TM at acoustic frequencies. The results show that the shear modulus is higher at the base than the apex. Using the TM material properties measurements, Gavara and Chadwick [47] estimated the shear wave velocity at a basal and more apical location in the guinea pig. Based on their value for the shear wave velocity, the shear modulus ($G_{xy} = v_s^2\rho$) is $0.67kPa$ for a basal location and $0.44kPa$ at a more apical location. We use for the shear modulus the same spatial variation as for the radial stiffness of the TM ($G_{xy}(x) = G_0 \exp(\alpha_{tm}x)$). The values of the shear modulus

are of same order of magnitude as the values in [47]. In Ghaffari et al. [55], the phase angle of the complex shear modulus at the CF of the basal location (about 80kHz) is approximately 65°. For the guinea pig, at x=0.4 (CF=17kHz), and if the phase angle at 17kHz of the shear modulus is the same as in the mouse at 80kHz, the shear viscosity should be about $0.04Pa.s$.

In the theoretical results shown thus far, the shear modulus at the base is $G_0 = 7kPa$ and a constant value of $0.05Pa.s$ is used for the shear viscosity. Varying these parameters affects the predictions of the BM magnitude in response to acoustic stimulations only for frequencies near the CF as the results in Fig. 3.5 show. Increasing the shear modulus G_{xy} reduces the gain at the peak location (a few dB) and makes the response less sharp, as seen in Fig. 3.5(a). Increasing the shear modulus is akin to increasing the longitudinal coupling of the TM, hence this result is consistent with differences seen in the TM-LC and LR models (see Fig. 3.1). Increasing the shear viscosity η_{xy} reduces the gain, Q_{10dB} of the BM response and the phase accumulation at frequencies higher than the CF, as shown in Figs. 3.5(c) and 3.5(d). The TM shear viscosity plays an important role in modifying the slope of the phase at the CF; increasing the shear viscosity reduces the phase slope. For this range of parameters, the overall qualitative nature of the response predictions is not altered even though some of the quantitative details are affected.

3.2.4 Longitudinal coupling stabilizes the linearized cochlear model

Introducing longitudinal coupling, particularly in the TM, stabilizes the linear model. For the parameters chosen in this paper, the linearized LR model is at the limit of stability for a 25 dB BM gain whereas the linearized TM-LC model is well under the stability limit for the BM gains seen experimentally (*e.g.*, 35dB). The stability limit is found by increasing the MET sensitivity until the impulse response is no longer finite and bounded (*i.e.*, the system is unstable). Numerical experiments

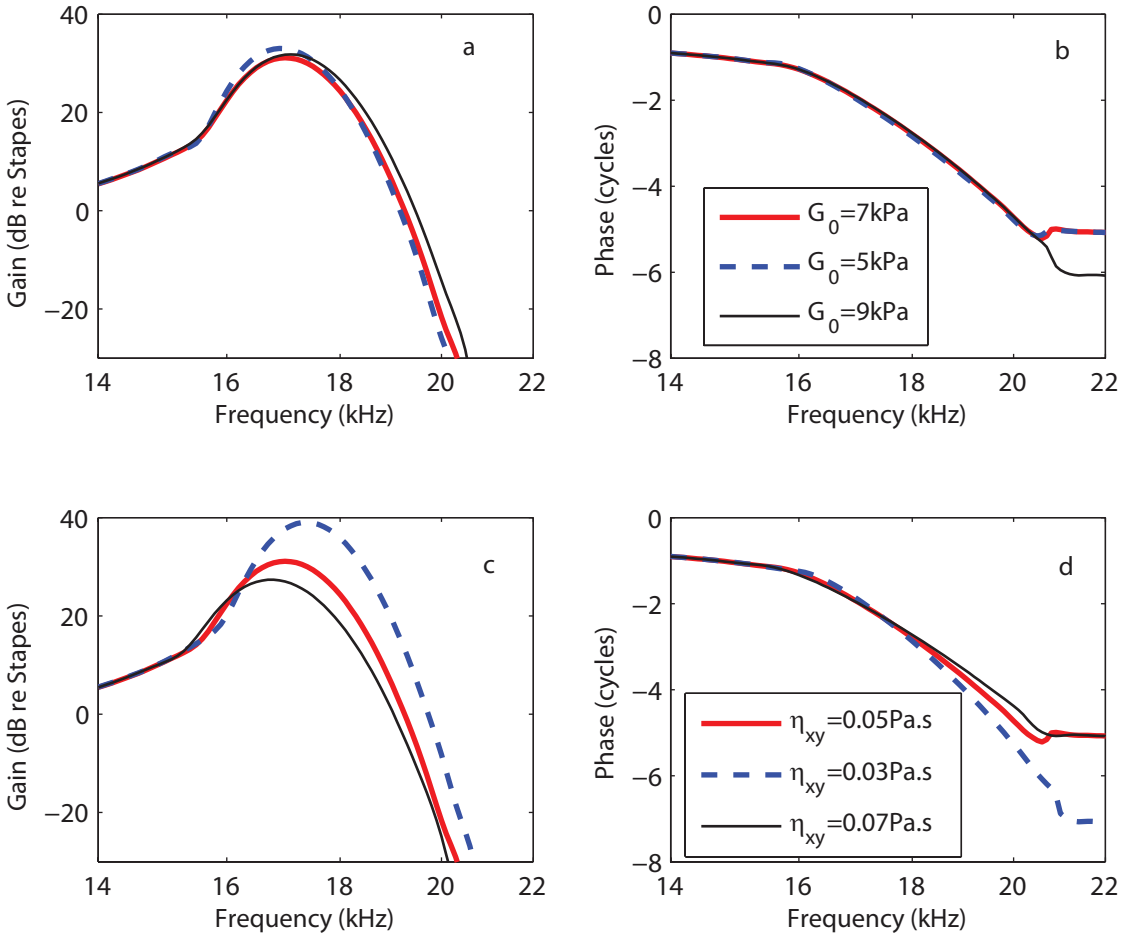

Figure 3.5: Model sensivity to TM parameters variations. (a and b) Effect of changing the shear modulus, G, on the amplitude (a) and phase (b) of the BM gain relative to the stapes (legend in (b)). (c and d) Effect of changing the shear viscosity, η, on the amplitude (c) and phase (d) of the BM gain relative to the stapes (legend in d). For all simulations the activity is kept constant (86% activity).

(results not shown) indicate that this change in the stability of the system is only due to the addition of longitudinal coupling and not to the modifications of the OHC parameters between the two models. A key finding of this work is that the cochlea is stabilized, in part, by the longitudinal coupling of the TM and that this stabilization allows for the cochlea to achieve higher stable levels of gain than would be possible without the longitudinal coupling.

3.2.5 Power delivered by somatic motility to the BM

Further processing of the results for the LR and TM-LC models to determine the power delivered to the BM by the OHC are shown in Fig. 3.6 (results shown with a thin line and thick line, respectively), for a location near the 17kHz best place. For both models, the OHCs are predicted to convert electrical to mechanical power and deliver power to the BM for frequencies lower than the CF. In the LR model, the OHCs deliver significant mechanical power to the BM in a narrower range of frequencies near the CF than in the TM-LC model (as normalized by the maximum mechanical power delivered to the system by the OHC). We attribute this to the coupling of multiple OHCs by the structural longitudinal coupling.

3.3 Comparison to experimental data

Longitudinal coupling in the TM mechanics has been shown in the previous section to have the dominant effect on the BM response to acoustic stimulation. In this section the predictions of the TM-LC model are compared to experimental measurements of the BM response to acoustic stimulation.

3.3.1 Frequency response of the BM

In Fig. 3.7(a) and in Fig. 3.8, predictions of the BM gain by the TM-LC model are compared to experimental data for guinea pigs from de Boer *et al.* [35] and Zheng

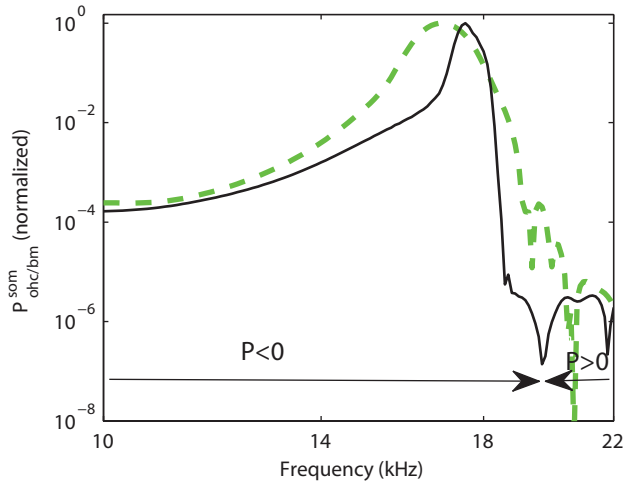

Figure 3.6: Power delivered by the somatic force to the BM. The absolute value of the power of the OHC active (somatic) force on the BM ($P^{som}_{ohc/BM}$), normalized to the value at the CF, is plotted as a function of frequency. Thick dashed line: $P^{som}_{ohc/BM}$ in the TM-LC model. Thin solid line: $P^{som}_{ohc/BM}$ in the LR model. For both models the parameters are the same as in Fig. 2. The sign of the power (P on the figure) is indicated on the figure to show the frequency region where the OHC somatic forces add power to the BM ($P^{som}_{ohc/BM} < 0$) and the frequency region where it removes power from the BM ($P^{som}_{ohc/BM} > 0$). For both models the OHC somatic force adds power to the BM for frequencies less than the CF and up to about 20kHz.

al. [159]. Even though the protocols for these two experiments were different (in de Boer *et al.* [35] bands of flat-spectrum pseudo-random noise stimulations were used while Zheng *et al.* [159] used pure tone acoustic signals), the same model is able to replicate important characteristics for both experiments. The model is a linear model and the variation from the fully active model to the passive model is achieved by decreasing the mechanoelectrical transducer (MET) sensitivity (as discussed in Ramamoorthy *et al.*[121] and in Chapter II). The frequency responses of the basilar membrane track with the experimental data from deBoer *et al.* at different SPLs (Fig. 3.7(a)) when the gain of the MET channels is reduced. The TM-LC model predicts around 35dB gain for low level acoustic stimulation. As seen in experimental results, the shift in the peak frequency between the fully active and passive cases is about half an octave. The BM gain curve becomes sharper as the activity is raised. The mechanical quality factor predicted by the TM-LC model is more consistent with the experimental measurements than the results from the locally reacting model (see Fig. 3.1). The Q_{10dB} values predicted by the TM-LC model at the highest activity match approximately the experimental values for low SPL stimulation. For instance, Q_{10dB} is 7.7 in the fully active TM-LC model compared to 6.5 in Zheng *et al.* experiment [159] (compare the heavy solid and dashed curves in Fig. 3.8). The TM-LC model prediction for the BM phase follows closely the data from de Boer *et al.* (see Fig. 3.7(b)). Note that the phase data are not available from Zheng *et al.* [159]. The phase accumulation at high frequency is about 5.0 cycles in the active TM-LC model compared to 4.5 cycles in the 20dB SPL experiment. The phase accumulation at CF is about 2 cycles in both the model and the experiment. The model predictions for the phase slope at CF are slightly higher than in the experimental data.

For all four models it is possible to choose parameters to replicate the level of gain seen in the experimental results for low level sound (see Ramamoorthy *et al.* [121] and Fig. 3.7(a)). But, as seen in Fig. 3.1, only the TM-LC and BMTM-LC models

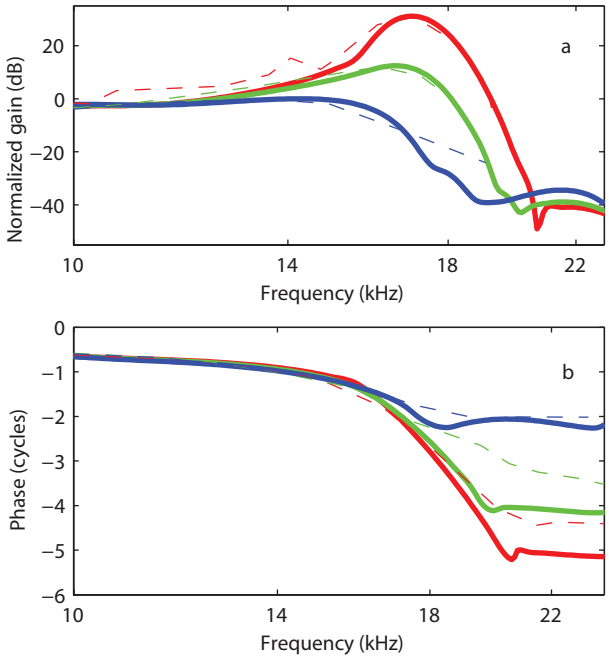

Figure 3.7: Comparison of the TM-LC model response with experimental data from deBoer [35]. The TM parameters are $G_0 = 7kPa$ and η=0.05 Pa.s. Solid lines: model BM gain for 86% activity, 56% activity and 0% activity; dash lines: guinea pig data at 20, 80 and 100dB. (a) Normalized (to the maximum passive response) BM magnitude in dB (b) BM phase relative to the stapes in cycles.

replicates the Q_{10dB}.

The simulations of the gain at different longitudinal locations of the cochlea follow the expected trend, as shown in Fig. 3.9. The peak of the BM gain curves shifts to lower frequency as the location approaches the apex, accompanied by a lower gain and Q_{10dB} (see also Ramamoorthy *et al.*[121]).

3.3.2 Impulse response

By taking the inverse Fourier transform of the frequency response, an impulse response can be derived from the experiments and simulations. Results from the TM-LC theory are compared to measurements from de Boer [35] in Fig. 3.10. The oscillations of the response continue up to about 1ms in experimental data (Fig. 3.10(b)) and 1.4ms (Fig. 3.10(a)) for the model simulations in the active case. This

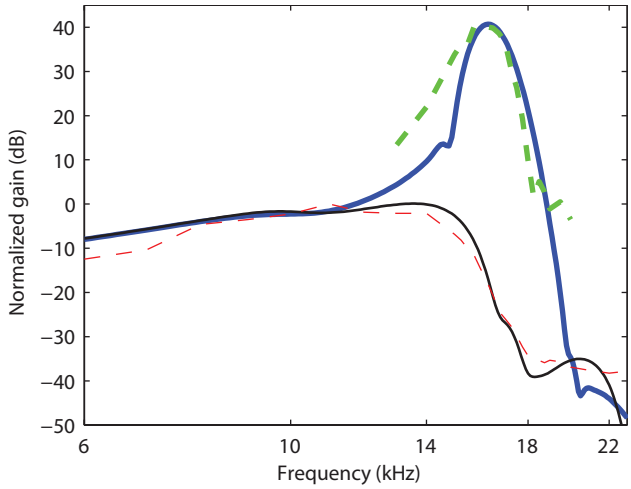

Figure 3.8: Comparison of the TM-LC model response for the gain with experimental data from Zheng *et al.* [159]. The TM parameters are $G_0 = 7kPa$ and η=0.07 Pa.s. Solid lines: model BM responses for 100% activity (thick line) and 0% activity (thin line); dash lines: experimental data at 10dB (thick line) and 100dB SPL (thin line).

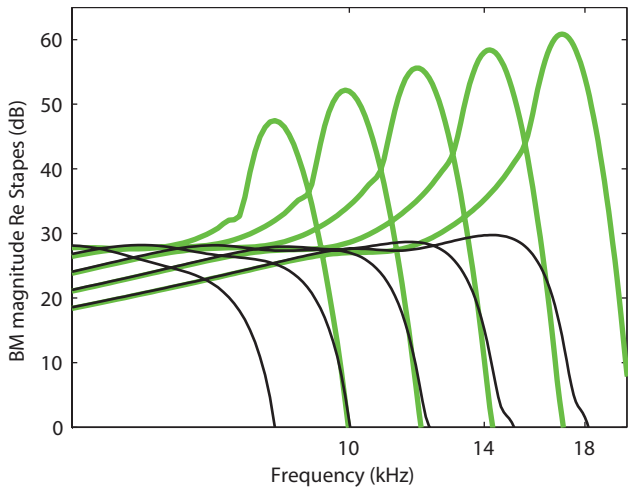

Figure 3.9: Panoramic view of the predictions of the BM gain. The predictions of the BM response relative to the stapes are plotted as a function of frequency in the TM-LC model at different longitudinal locations ($x = 0.4cm$,$0.5cm$,$0.6cm$,$0.7cm$ and $0.8cm$). The active (81% activity) model responses are shown with a thick solid line. The passive model responses are shown with a thin solid line. As the location approaches the apex, the peak of the BM gain curve shift to a lower frequency, the magnitude of the BM gain is lower and the tuning of the response is less sharp.

is a considerable improvement over the LR theory, which incorrectly predicted a much longer impulse response in the active case, with oscillations that continue up to 3ms [121]. In the passive case the oscillations are about 0.4 to 0.5ms both in the experimental results and the model simulations. Note that for the passive case, the model is relatively insensitive to TM longitudinal coupling as both models match the experimental results quite well for the impulse response. The model also predicts the same zero crossings of the passive and active response for the first few cycles, consistent with observations from de Boer *et al.* [35]. Fig. 3.10 shows that the duration of the impulse for the model and experiments are roughly the same. However, there are differences as the predicted maximum amplitude is reached at 0.8ms while experimentally the peak occurs at 0.5ms. This may be due to the slight differences in the signal processing, but more likely it is due to some deficiencies in the model (notably the nonlinearity), as minor differences in phase-frequency relations between theory and experiments are also seen.

3.3.3 Comparison to data from mutant mice

The role of TM longitudinal viscoelastic coupling is partially corroborated by the experimental results of Russell *et al.* [137] where they used a β-tectorin knockout mouse which possesses reduced longitudinal coupling (as measured by Ghaffari [54]) and showed sharper tuning, as we have predicted. Our model shows that the TM properties do not have a significant influence on the shape of the passive frequency response; such a finding is consistent with measurements of the BM response in mutant mice with a detached TM [86]. The BM-LC model predicts a Q_{10dB} that is lower than in the LR model but still much higher than in the experimental data. Since the BM resonance is at a much higher frequency than CF, the effect of longitudinal coupling in the BM equation is not as dramatic on the tuning of the BM response as the effect of longitudinal coupling in the TM. Because of the mechanical connection

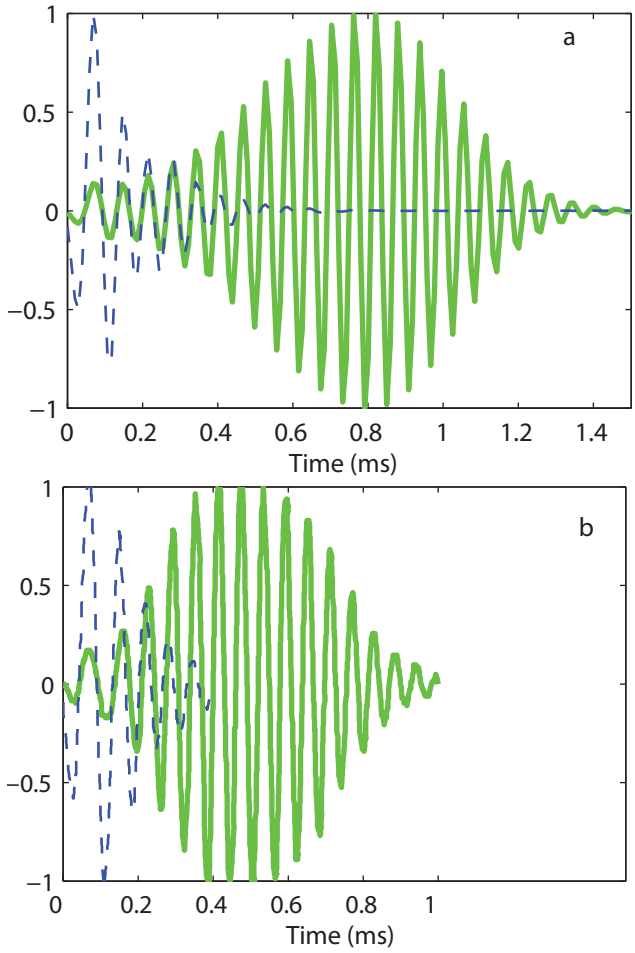

Figure 3.10: Impulse response. The normalized theoretical and experimental impulse response functions are plotted as function of time. (a)TM-LC model impulse response . Dashed line: passive response. Solid line: active response (86% activity) (b) Normalized experimental BM impulse responses from de Boer [35] at 10 dB SPL (solid line) and 100dB SPL (dashed line).

to the HB and the fact that our model predicts that the shear resonance of the TM corresponds to the CF at the base of the cochlea, the TM appears to be the most important structure determining the broadness of the active frequency response (at a basal location).

When we implement our TM-LC model with a significantly reduced shear modulus and shear viscosity while keeping other parameters constant, the BM gain is higher and the cochlear model is unstable at high activity. If such an instability were present when TM longitudinal coupling is reduced, then we should expect an increase in the gain and the presence of broad band otoacoustic emissions. However, in measurements by Russell *et al.*[137], the mutant mouse with reduced TM longitudinal coupling (as shown by Ghaffari [54]) has a reduced BM sensitivity compared to the wild type mouse and broad band otoacoustic emissions have not been reported. This apparent contradiction between model predictions and experimental results indicates that the mutant mouse cochlea might develop with a reduced MET sensitivity and/or OHC somatic force compared to a wild-type mouse. In order to predict the same gain at the CF, a lower value of the electromechanical coupling coefficient of the OHC (ϵ_3 in Eq. 2.9) is used in the LR model than in the TM-LC model. Note that both values of ϵ_3 are realistic, within 50% of the experimental estimate from Iwasa *et al.*[72].

3.4 Conclusions about the role of structural longitudinal coupling in cochlear mechanics

This model demonstrates that the TM is a crucial structure for active cochlear mechanics because of its connectivity to the HBs. Hence the presence of the TM and of OHC somatic motility is essential to assure a high BM sensitivity. Our model predictions for the BM frequency response and impulse response show that TM longitudinal coupling, and to a lesser extent, BM longitudinal coupling, are critical for a

well-functioning cochlea. The human ear needs to have both a high frequency selectivity and a short impulse response as well as a high sensitivity. This tradeoff between frequency discrimination and transient capture is controlled mostly by the longitudinal viscoelastic properties of the TM. The same longitudinal coupling is responsible for stabilizing the highly sensitive cochlea.

CHAPTER IV

Effect of active hair bundle mechanics and fast adaptation on prestin-based high frequency cochlear amplification

4.1 Introduction

The identity of the mammalian cochlear amplifier, whether based on outer hair (OHC) somatic motility (linked to the action of prestin), OHC hair bundle (HB) motility (linked to adaptation of the transduction current, [67, 126]), or some combination of these effects remains an ongoing debate [4, 119] because of the difficulty in isolating the two effects in a conclusive *in vivo* experiment in a sensitive preparation. We approach this problem by constructing a theoretical model including both active modalities in a way that their contributions can be evaluated.

According to the most widely accepted theory, the active process in the mammalian cochlea is driven by the conversion of electrical to mechanical energy by a voltage sensitive transmembrane protein, prestin [158], in the OHC lateral wall (e.g., see [3]). When the HBs of the OHCs are deflected due to vibrations in the organ of Corti (OoC), the HB transduction channel opens and the current depolarizes the OHC. The resulting transmembrane potential produces a force [11] at high frequencies [43]. Recent experiments that alter force production by prestin, either by perfusion

with salicylate [141] or genetic mutation [87, 32], have proven that prestin based motility is necessary for normal cochlear function. The main criticism of the somatic force generation hypothesis is that the lowpass filtering due to the OHC basolateral membrane electrical impedance reduces the potential associated with a HB generated current so that the somatic force is unable to amplify the motion of the structures of the OoC [140]. However, we have previously predicted [121, 97] that the OHC transmembrane potential arising from acoustic stimulation is sufficient for somatic motility alone to provide high frequency amplification. In the present study, we examine the role of HB adaptation on the active process at high frequencies and determine if this prediction still holds once HB forcing is included into the mathematical model.

Of course, the presence of HBs is also requisite as the channels must be activated (i.e., opened) in order for the time varying transduction current to flow. Once opened, calcium mediated fast adaptation will occur. Over that past five years, fast adaptation [81, 128, 80, 8] and force production [80, 8] on a submillisecond time scale have been reported in mammalian HBs. Slow adaptation and force production [8] are also observed, however this modality likely does not play a direct role in cycle-by-cycle amplification. From the measurements, it is now reasonable to assume that HBs can generate forces on a time scale commensurate with high frequency sound, but it is not clear that this force has sufficient authority to influence the response of the BM or other cochlear structures. Different models, based on the gating spring model of transduction [93], have been developed to predict the active HB dynamics. Fast adaptation has been modeled by different mechanisms that promote channel reclosure or reduce tension in the gating spring through the binding of calcium to some moiety in the channel [157, 67, 9, 94]. The theoretical analysis of Sul and Iwasa of an individual HB, calls into question whether HBs can act as the sole source of amplification at high frequencies, as the HB cannot produce enough mechanical energy to overcome the viscous damping in the subtectorial gap in mammals [152].

We reexamine this result in the context of a complete cochlear model.

In this chapter, fast adaptation, and its effect on transduction channel filtering and HB mechanics, is coupled to OHC somatic motility in the linear mechanical-electrical-acoustical mathematical model of the cochlea described in chapter II. The nonlinear dynamics of the HB, based on a six state channel reclosure model of the HB [17], is linearized for small harmonic stimuli and then incorporated into our global model. The advantage of this approach is that we explicitly separate the contributions of each active modality and analyze their influence on the mechanics of the hearing organ, estimating, for instance, if forces are sufficient to modulate the BM response. Moreover, we model the effect of introducing pharmacological agents (such as salicylate [141]) or varying ionic concentrations on the cochlear response.

4.2 Active outer hair cell hair bundle model

4.2.1 Active nonlinear HB model

We describe here the nonlinear model of the HB dynamics used a basis for the linearized HB model. As in [152, 17], fast adaptation is modeled by a reclosure mechanism. The slow adaptation motor is assumed to set the resting tension in the gating spring but not to affect the dynamics of the HB at the frequencies considered here. The six-state transduction channel model, with two calcium binding sites is described in Fig. 4.1. In this model, calcium binding of some moiety in the channel causes a reduction in the intrinsic energy difference between the closed and open states of the channel. When an external force, F_{ext}, is applied to the HB, the differential equation governing the motion of the HB is given by:

$$c_{hb}\frac{du_{hb}}{dt} + N\gamma t_{gs} + K_{sp}(u_{hb} - X_{sp}) = F_{ext}\,, \tag{4.1}$$

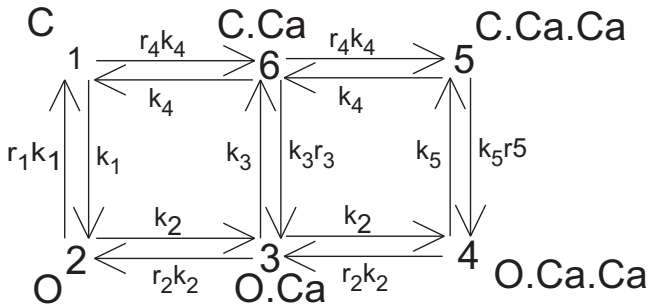

Figure 4.1: Six states channel reclosure model of the HB. The HB has two binding sites and six states: closed (state 1), open (state 2), open and bound to one calcium ion (state 3), open and bound to two calcium ions (state 4), closed and bound to two calcium ions (state 5) and closed and bound to one calcium calcium (state 6). Calcium binding reduces the intrinsic energy difference between the open and closed state of the channel (modeled by r_3 and r_5). The transition rates governing the transduction channel at the operating point $x = 0$ are indicated on the figure.

where c_{hb} is the damping coefficient of the HB due to the viscous fluid, N is the number of transduction channels per HB, t_{gs} is the tension in each gating spring, K_{sp} is the stiffness of the stereocilia pivot, X_{sp} is a constant and u_{hb} is the displacement at the tip of the HB, in a direction perpendicular to the length of the HB ($u_{hb} = 0$ corresponds to equilibrium). The tension in each gating spring is given by:

$$t_{gs} = k_{gs}\Big(x - x_a - P_0 d\Big) \tag{4.2}$$

where k_{gs} is the gating spring stiffness, d is the gating swing, P_0 is the open probability of the transduction channel, x_a is the position of the slow adaptation motor (assumed to be a constant) in the tip link direction, and x is the displacement of the HB in the tip link direction ($x = \gamma u_{hb}$ where γ is the geometrical gain factor).

As in [17, 8], the two binding sites are assumed to have the same affinity to calcium (modeled by the dissociation constant in the open state K_D^o, and in the closed state, K_D^c) and calcium binding coefficient (denoted as K_B^o in the open state and K_B^c in the closed state). The calcium concentration is denoted as C_{fa}^o and C_{fa}^c for the open and

closed states, respectively.

The energy difference between the open and closed states of the channel is given by:

$$\Delta E = f_{gs}x + \Delta E_0 - n_{Ca}\epsilon_{Ca} \tag{4.3}$$

where f_{gs} is the single channel gating force in the tip link direction ($f_{gs} = k_{gs}d$) and ΔE_0 is the energy difference between the unbound open and closed states of the channel at $x = 0$ (due to the resting tension of the gating spring and to the intrinsic energy difference between the open and closed states of the channel), n_{Ca} is the number of calcium ions bound to the channel ($n_{Ca} = 0$, 1 or 2) and ϵ_{Ca} is a constant energy that represents the reduction in the intrinsic energy difference of the channel due to calcium binding (based on a thermodynamic analysis of the HB [152], $\epsilon_{Ca} = k_B T ln(\frac{K_D^o}{K_D^c})$). The equations for the rates of calcium binding and unbinding and of channel opening and closing are detailed Appendix C.

4.2.2 Linearized active HB model

Using a similar approach as in [152], the nonlinear equations governing the dynamics of the HB are linearized for small pertubations about the resting state and reduced to Eq. 4.8. Using the additional constraint $\sum_{i=1}^{6} P_i = 1$, the equations of the kinetic scheme of the six states channel (Fig. 4.1) can be reduced to the following nonsingular matricial form:

$$\frac{d\mathbf{P}}{dt} = \mathbf{A}(\frac{f_{gs}x}{2k_BT})\mathbf{P} \tag{4.4}$$

where $\mathbf{P}$ is the vector formed by the probabilities of each state $\mathbf{P} = [P_1 P_2 P_3 P_4 P_5]$ and $\mathbf{A}$ is a 5×5 matrix that is a function of the HB deflection x. The vector of resting probabilities for $x^s = 0$, $\mathbf{P^s}$, is found by solving $\mathbf{A}(0)\mathbf{P^s} = 0$.

Using the same approach as in [152], the nonlinear differential equations governing the dynamics of the HB (Eqs. 4.1 and 4.4) are consistently linearized around

equilibrium. For small harmonic perturbations δF_{ext}, the nonlinear model response $(\delta x, \delta \mathbf{P})$ around the stationary point $(x^s, \mathbf{P^s})$ can be linearized. We assume a time dependence $e^{-i\omega t}$. Eq. 4.4 becomes:

$$\delta \mathbf{P} = \frac{f_{gs}}{2k_BT}(\mathbf{A}(\frac{f_{gs}x}{2k_BT}) + i\omega \mathbf{I})^{-1}\mathbf{A}'(\frac{f_{gs}x}{2k_BT})\mathbf{P^s}\delta x \tag{4.5}$$

where $\mathbf{I}$ denotes the 5×5 identity matrix and $\mathbf{A}'$ the derivative of $\mathbf{A}$ with respect to its argument. The change in the open probability is given by $\delta P_0 = \delta P_2 + \delta P_3 + \delta P_4$. A description of the optimization of the parameters of the transduction channel model can be found in Appendix E and the computation of the effect of calcium on HB dynamics and cochlear mechanics (Fig. 4.6) can be found in Appendix D. The values for the physical parameters of the HB are given in Table 4.1.

Parameter	Description	Optimal value
K_D^o	calcium dissociation constant in the open state	$12.43\mu M$
K_D^c	calcium dissociation constant in the closed state	$2.0\mu M$
K_B^o	calcium binding coefficient in the open state	$1.23ms^{-1}\mu M^{-1}$
K_B^c	calcium binding coefficient in the closed state	$12.3ms^{-1}\mu M^{-1}$
ΔE_0	energy difference between the open and closed state at rest	$0.2054k_BT$
ΔE_0^{NA}	energy difference between the open and closed when adaptation is not included state at rest	$0.8439k_BT$
k_1	rate of channel opening	$2.89 \times 10^5 s^{-1}$

Table 4.1: Parameters of the transduction channel at the 17kHz best place.

4.2.3 HB model without fast adaptation

Without adaptation, the HB is modeled as a two state channel, with only states 1 and 2 (shown in Fig. 4.2). The intrinsic barrier and resting open probability P_0^s are assumed to be the same as when adaptation is taken into account. This requires the energy difference between the open and closed state (ΔE_0^{NA}) to have a different value than in the case with adaptation (ΔE_0). The rates of channel opening, k_{co}^{NA}

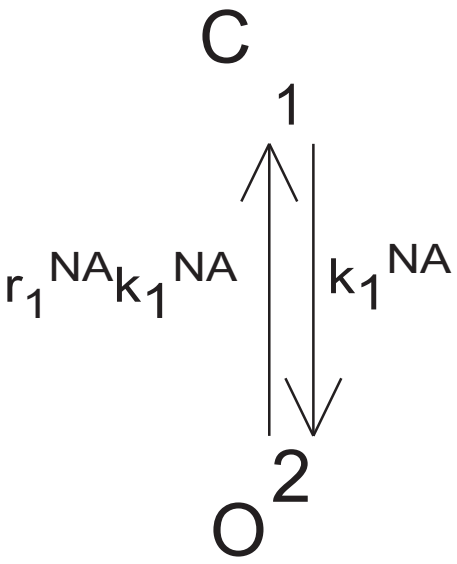

Figure 4.2: Model of the HB when fast adaptation is not taken into account. The channel has two states, open (2) and closed (1). The transition rates at the operating point x=0 are indicated on the figure. They are chosen so that the resting open probability is the same as in the 6 states channel model.

and closing, k_{oc}^{NA} without adaptation are given by:

$$k_{co}^{NA} = k_{co}^{0} \exp(\frac{\Delta E_0^{NA} - \Delta E_0}{2k_B T}) \tag{4.6}$$

$$k_{oc}^{NA} = k_{oc}^{0} \exp(-\frac{\Delta E_0^{NA} - \Delta E_0}{2k_B T}) \tag{4.7}$$

4.3 Isolated hair bundle

4.3.1 The HB MET sensitivity and active HB force are related

In the nonlinear model of the HB, the active reclosure mechanism (see section 4.2) is responsible for the active HB mechanics and fast adaptation of the transduction current. Because the physiologically relevant displacements of the HB are small for low intensity acoustic stimulation, the nonlinear model of the HB is linearized for

small fluctuations about equilibrium (similar to the approach in [152]). The equations relating time harmonic oscillations of radian frequency ω in the HB force, δF_{hb}, transduction channel current, δi_0, and HB displacement, u_{hb}, are:

$$\begin{aligned} \delta F_{hb} &= \Big[K_{pass} - K_{act}(\omega)\Big] u_{hb} \\ \delta i_0 &= G_a^{max} J(\omega) V^s u_{hb} \end{aligned} \tag{4.8}$$

where K_{pass} is the passive HB stiffness, $K_{act}(\omega)$ the complex active dynamic stiffness of the HB due to gating compliance [67] and fast adaptation, $J(\omega)$ represents the sensitivity of the transduction channel to HB deflection, V^s is the resting potential across the HB, and G_a^{max} is the maximum saturating conductance of the entire HB. $J(\omega)$ and $K_{act}(\omega)$ are given by:

$$J(\omega) = \frac{\gamma f_{gs}}{k_B T} TF(\omega) \tag{4.9}$$

$$K_{act}(\omega) = \frac{N \gamma^2 f_{gs}^2}{k_B T} TF(\omega) \tag{4.10}$$

where $TF(\omega)$ is the nondimensional complex valued frequency dependent transduction channel filter (see SI), f_{gs} is the single channel gating force in the tip link direction (chosen to be 5pN [8, 152]), k_B is Boltzmann's constant, T is the temperature, N is the number of transduction channels per HB, and γ is the geometrical gain factor relating HB motion to the tip link motion [67].

The mechanical energy generated by the HB per cycle depends on the imaginary part of the active stiffness in the following manner:

$$E_{hb} = \frac{\pi}{2} Imag\Big[K_{act}(\omega)\Big] |u_{hb}|^2 \tag{4.11}$$

where for this sign convention $E_{hb} > 0$ represents dissipation and $E_{hb} < 0$ generation. These relations reveal that HB energy generation (Eq. 4.11), the mechano-

electric transducer (MET) sensitivity (given by $G_a^{max} J(\omega) V^s$) and the active HB force ($K_{act}(\omega) u_{hb}$) are related and depend on the same frequency dependent filter, $TF(\omega)$, as shown in [152]. HB energy generation is proportional to f_{gs}^2 while the MET sensitivity is proportional to $G_a^{max} V^s f_{gs}$. The parameters of the transduction channel have been optimized to maximize the peak of the mechanical energy delivered by the HB. The HB parameters are then adjusted so that the transduction channel filter varies spatially and is tuned to the local characteristic frequency (CF) (see Appendix E).

4.3.2 The transduction channel is a poorly tuned bandpass filter and the dynamics of fast adaptation reduces the MET channel sensitivity

The magnitude and phase of the transduction channel filter, $TF(\omega)$, are plotted as a function of frequency in Fig. 4.3a-b for an isolated HB at the 17kHz best place (BP). In a model without adaptation, the transduction channel filter is a low pass filter with a cutoff frequency of 126 kHz, limited by kinetics of channel activation. When the fast adaptation mechanism is included, $TF(\omega)$ is a poorly tuned bandpass filter, with a barely discernible peak at 17.0 kHz, the CF. At CF, $|TF(\omega)|$ and hence the MET sensitivity (see Eqs. 4.8 and 4.9), are about 23% lower with adaptation than without adaptation. The phase of $TF(\omega)$ is around 5 degrees so that the MET current lags the HB displacement, but only by a small amount. The broad tuning of the transduction filter is also manifest in the real part of the active HB stiffness, $K_{act}(\omega)$, as shown in Fig. 4.3c. The passive bundle stiffness (0.15 mN/m at this location) is reduced only by 3% by the positive active stiffness.

4.3.3 Energy dissipation and generation by the effects of HB fast adaptation and channel activation are small

The mechanical energy generated by the HB as computed from Eq. 4.11 is shown in Fig. 4.3d for a HB located at the 17 kHz BP. The magnitude of the energy dis-

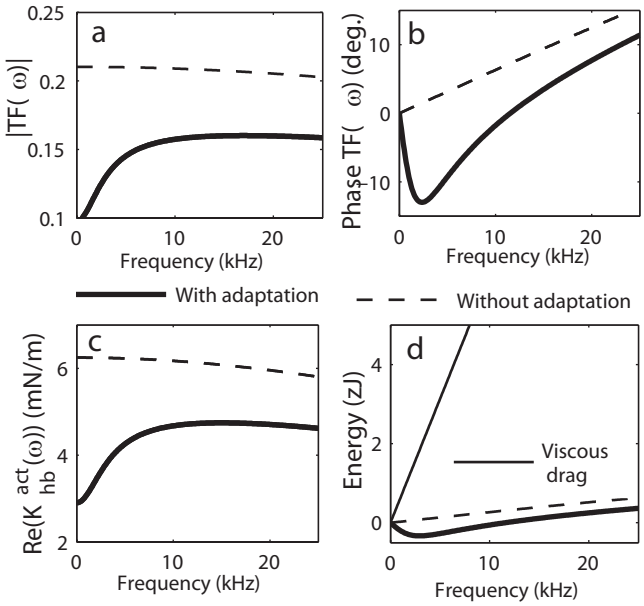

Figure 4.3: Predictions of the transduction filter function, active stiffness and energy generation for a single isolated HB. The predictions are plotted versus frequency for a single isolated HB at the 17 kHz BP. These results vary spatially with frequency in a way described in Appendix E (Fig. E.1). In each plot, the thick solid line represents the predictions with fast adaptation and channel activation included in the model and the dashed line represents the results with only channel activation included. (A) Magnitude and (B) phase of the transduction channel filter, $TF(\omega)$ (defined by Eq. 4.9) which relates the MET current to HB displacement. (C) The real part of the active HB stiffness, $K_{hb}^{act}(\omega)$. (D) Mechanical energy (positive is dissipation, negative generation) by the HB for a $0.5nm$ HB displacement. The energy dissipated by viscous drag in the subtectorial space is shown in a thin solid line.

sipated or generated by the HB is predicted to be much smaller than the energy dissipated by viscous drag of the HB through the surrounding fluid, except at the lowest frequencies. As in [152], the model without fast adaptation predicts that the HB dissipates mechanical energy over all frequencies. With fast adaptation, the HB delivers mechanical energy at frequencies less than CF, with a peak at 2.9 kHz. However, the magnitude of the energy generated at this frequency is less than the energy dissipated by viscous drag. At frequencies above 11.5 kHz, the HB dissipates energy, but the amount of energy dissipated is small, more than two orders of magnitude less than viscous drag at CF, for instance.

4.4 Simulations of the acoustic response of the cochlea

4.4.1 A complete cochlear model including somatic motility and HB activity predicts the BM response to low intensity sound stimulation

The response of the BM to low intensity acoustic stimulation is simulated using the macroscopic mathematical model of the cochlea described in Chapter II. The model includes HB mechanoelectrical transduction and can include any combination of somatic motility and HB activity (fast adaptation and HB motility, modeled by Eq. 4.8). The predicted frequency dependence of the normalized BM displacement at the 17kHz BP is shown in Fig. 4.4. The passive model of the BM response (without somatic motility or HB activity) exhibits a broad peak, as observed in measurements at high intensity or postmortem [159]. With HB activity and somatic motility, the BM response approximately matches the sensitivity (with a 35dB gain relative to a passive model), tuning (with a mechanical quality factor, Q_{10dB}, of 7.7 versus 6.5 in the experiment) and peak frequency (about 17kHz) of the experimental response to low intensity acoustic input [159]. However, when HB activity is included and somatic motility is not included, the response reverts nearly to that of a passive model. If

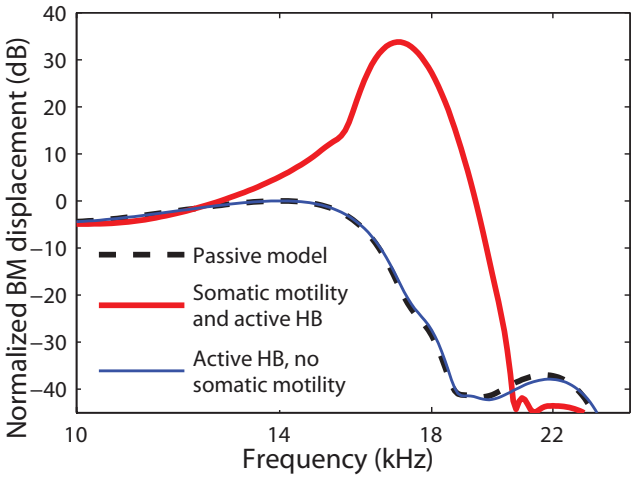

Figure 4.4: BM response to acoustic stimulus for three different cochlear models. Displacement of the BM in dB normalized to the maximum passive response due to acoustic stimulation at the 17kHz best place. Thick solid line: prediction with somatic motility and HB activity (fast adaptation and active HB mechanics). Thick dashed line: prediction of a passive model. Thin solid line: theoretical prediction of HB activity only without somatic motility.

somatic motility is included in the model but HB activity is not included, the model actually predicts an unstable response (determined using the inverse Fourier transform of the frequency response as in [121]) and hence we do not show this result. The presence of fast adaptation reduces the MET sensitivity (Fig. 4.3(a)) which makes the system with somatic motility and HB activity less sensitive and more stable.

4.4.2 Somatic motility, not HB motility, amplifies motion for frequencies near CF

When we speak of energy generation, we mean net conversion to mechanical energy from some other form of energy on a cycle-by-cyle basis. Somatic motility can convert electrical energy (in the form of the resting endocochlear potential) to mechanical energy (e.g., [121]) in a nearly reciprocal fashion [71] while HB activity can transfer chemical energy to mechanical energy during the binding process [17, 152]. The results for an individual HB presented in Fig. 4.3d are now revisited by making predictions

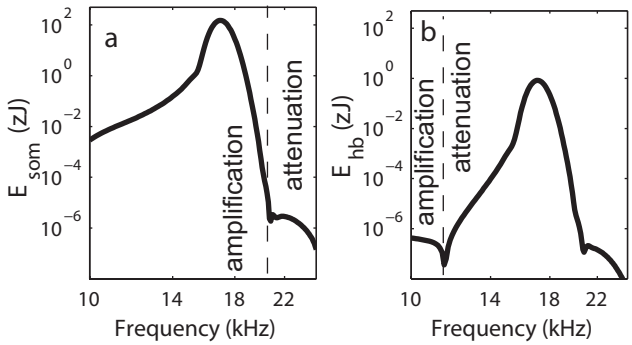

Figure 4.5: Mechanical energy generated by the active processes per cycle. The energy for a 0.5nm BM displacement is plotted as a function of frequency. (A) Energy generated by somatic electromotility. (B) Energy generated by HB activity. The active process generates mechanical energy on the left of the dashed line and dissipates mechanical energy for higher frequencies.

in a global cochlear model. The mechanical energy delivered per cycle by the somatic force is given by:

$$E_{som} = \pi Im\Big[\epsilon_3 \, \Delta\phi_{ohc} \times (u_{ohc}^{comp})^*\Big], \tag{4.12}$$

where * denotes the complex conjugate and $Im[\cdot]$ the imaginary part of a complex number. The mechanical energy delivered per cycle by the somatic force and the HB force is plotted as a function of frequency in Fig. 4.5 for a 0.5nm BM displacement. The upper limit of energy generation derived from somatic motility is 20.5 kHz while that for HB motility is 11.5 kHz. Hence, the HB dissipates mechanical energy at CF. Moreover, the energy dissipated by the HB is about two orders of magnitude lower than the energy delivered by the somatic motility at CF.

4.4.3 The gain of the BM response to acoustic stimulation depends on the somatic electromechanical coupling coefficient and on the calcium concentration

We varied the electromechanical coupling coefficient (ϵ_3 in Eq. 2.9) in order to determine the effect of a small reduction in prestin activity, as might be induced by

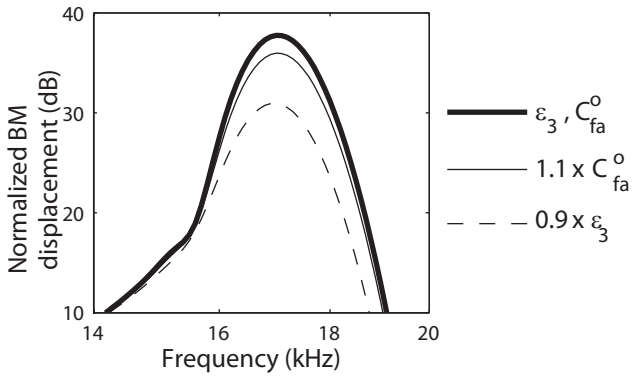

Figure 4.6: Effect of changes in the OHC somatic electromechanical coupling coefficient, ϵ_3, and in the endolymphatic calcium concentration, C^o_{fa}, on the predictions of the BM response to acoustic stimulation. The normalized BM gain is plotted as a function of frequency. Thick solid line: initial values for ϵ_3 and C^o_{fa}. Thin solid line: C^o_{fa} is increased by 10%. Thin dashed line: ϵ_3 is reduced by 10%.

intracellular perfusion of salicylate [141]. In Fig. 4.6, the BM gain in response to low intensity acoustic stimulation is reduced by 6.5 dB when ϵ_3 is reduced by 10%, similar to reductions seen in salicylate perfusion experiments. A small increase of the calcium concentration at the fast adaptation site (when the channel is open), C^o_{fa}, by 10% results in a 2.3 dB reduction in the gain through a reduction of the amplitude of $TF(\omega)$. Alterations of the calcium concentration can be induced by disturbance of endolymph calcium homeostasis (for example due to endolymphatic hydrops in Meniere's disease [139]) or exposure to loud sounds [45] although the relation between these conditions and the calcium concentration is less clear than for the effect of salicylate on electromotility.

4.5 Discussion

In our model we can explore a variety of ways for HB and somatic force generation and HB filtering to alter the mechanics and response of the cochlea. At the outset we envisioned several potential scenarios for their interaction at high frequencies, including some sort of synergistic amplification by both processes. We found a very different

cooperation between the two modalities. Somatic motility provides the amplification at CF. Fast adaptation serves to reduce the MET channel sensitivity and assist in the maintenance of the system's stability. HB amplification somewhat ameliorates the dissipative effects of channel gating, but neither the added energy nor the amount of dissipation are significant compared to dissipation by the HB moving through the fluid (see Fig. 4.3d). The analysis concluding that the energy generated per cycle by an isolated HB was not sufficient to influence high frequency global cochlear mechanics was confirmed by our simulations (see Fig. 4.5). The somatic-based amplification mechanism proposed here is consistent with measurements where intracochlear perfusion of salicylate [141] or prestin-knockin mutation [32], interventions known to disrupt the prestin-based transduction, also reduce cochlear output (either in the BM gain or auditory thresholds) as in our model (Fig. 4.6).

4.5.1 RC filtering of the OHC transmembrane voltage does not preclude somatic motility from acting as the cochlear amplifier

Our results show that somatic motility can be the underlying source of high frequency mammalian cochlear amplification despite lowpass filtering of the transducer currents by the basolateral membrane of the OHC. In our model, the OHC cutoff frequency is 280Hz at the 17 kHz BP. At this location, in a sensitive cochlea, a sound input at 17kHz of around 20 dB SPL gives rise to a BM displacement of 0.5 nm [20]. For such a displacement, we predict a transduction current of 0.75 nA and a transmembrane potential of 310 μV for an OHC at this location. There is strong evidence that these are physiologically realistic values. In our model, the value of the HB saturating conductance, G_a^{max}, is set to 323 nS at the 17 kHz BP. Using the *in vitro* hemicochlea preparation at room temperature, He *et al.* [63] measured a conductance of 34.7nS for a basal HB in the adult gerbil hemicochlea. If this value is corrected for the differences between the experimental conditions and the *in vivo*

conditions (as discussed in Chapter II), the expected *in vivo* value is $208nS$. This value is about 50% lower than the value we used. Even higher *in vivo* values of G_a^{max} are expected *in vivo*, as discussed in Chapter II. The largest *in vitro* current measured by [63] is 2.4 nA. Using the same temperature and ionic corrections as above, along with a factor of 2 for a larger *in vivo* resting DC potential, our estimate of the largest current is 28 nA, larger than our theoretical estimate near threshold of 0.75 nA. Moving to a discussion of the voltage, we predict an OHC transmembrane potential that is higher than the only *in vivo* transmembrane measurements [85] at these frequencies. This is expected, as discussed in [63, 29, 136, 44], because the microelectrode measurement underestimates the receptor potential due to the leak conductance around the electrode, the piercing of the OHC membrane (which may reduce the driving DC receptor potential), the loss of sensitivity due to the overall surgical preparation, and any mechanical constraints due to the microelectrode penetration. Extracellular potential measurements are less invasive and our prediction (0.1mV for a 0.5nm BM displacement) is in good agreement with the measurement based estimate of [44] (about 0.08mV for a 0.3nm BM displacement) for a cochlea in good physiological condition.

Our theoretical model predicts the response that would be measured in a pristine sensitive cochlea. Hence, the quantitative differences are reasonable in view of the differences between the model and measurement configurations. We show that a submillivolt transmembrane potential is converted to an active somatic force of 34 pN at CF (less than 1% of the *in vitro* maximal values of about $10nN$ [72]), a force sufficient to provide for the 35-40 dB gain difference between sensitive and insensitive conditions *in vivo*.

In order to achieve a transduction current of 0.75 nA, two additional factors are of central importance. First, an electromechanical resonance of the OoC-TM system, due to the interaction of the TM mass [162, 59], the compliance and kinematic

constraints of the structures of the OoC, and the active somatic force, magnifies the HB shearing motion and maintains the appropriate phase of the HB transducer current. This electromechanical resonance is responsible not only for the sharp tuning of the transducer current, but also for that of the BM motion. This tuning does not arise from either the intrinsic tuning of somatic electromotility (which is not tuned [43]) nor from HB filtering (which was shown here to be poorly tuned in Fig.4.3(a)). The second important factor is the longitudinal propagation of electrical current in the scalae and interstitial space. By artificially altering the numerical values of the fluid conductances in our model, we tested the effect of longitudinal propagation of current in the scalae and the interstitial space on our predictions. Including this conductance path provides for roughly 5 dB of additional gain in the present model due to an increase in the transmembrane potential that drives somatic motility.

4.5.2 Could HB motility be the amplifier?

In our model, we find that if we use a higher single channel gating force, such as 24pN as used in [103], and faster kinetics for adaptation that active HB force can have a more prominent role in high frequency cochlear amplification. Higher values of f_{gs}, however, are not supported by the literature [8, 155]. The calcium binding coefficients we use at the base of the cochlea are near the upper limit for a diffusion limited reaction [6]; hence it is unlikely that the kinetics can be much faster. Therefore, it does not appear that HB forcing is responsible for cochlear amplification at high frequencies. For lower frequency hearing, nearer to the apex of the cochlea, HB forcing may play a more important role [122]. Continued system level and cellular level biophysical measurements along with fully nonlinear mathematical models are still needed to completely describe the response of the cochlea. In light of our small-signal modeling results, we conclude that, in the base of the mammalian cochlea, prestin mediated somatic motility of outer hair cells is the mechanism by

which stored electrical energy is converted into mechanical energy driving cochlear amplification and providing for acoustic compression so essential to normal hearing.

CHAPTER V

Nonlinear response of the cochlea to a single tone: compressive nonlinearity, harmonic distortion and DC shift

5.1 Introduction

In the previous chapters the dynamics of the cochlea were linearized for small harmonic stimuli around the operating point so as to simplify the analysis and limit the computational cost. However, the cochlea is a weakly nonlinear system. In this chapter we are interested in the prediction of the stationary nonlinear response of the cochlea to a single tone. The nonlinear model and the method used to compute the nonlinear dynamics of the cochlea in response to stationary acoustic stimulation are first described. Simulations of the response to a single tone are then presented and compared to experimental measurements and to the linear formulation so as to validate the model and method.

5.2 Nonlinear finite element formulation and algorithm

5.2.1 Problem formulation

The analysis of Chapter IV showed that the active HB forcing does not underlie cochlear amplification and can be ignored. Moreover, somatic motility and the basolateral membrane capacitance depend nonlinearly on the OHC transmembrane voltage [62], but the changes in the transmembrane voltage are small under acoustic stimulation (based on experimental [85] and theoretical observations [90]) so that somatic motility and membrane capacitance can be described *in vivo* by linearized relations. Therefore, as in other models of nonlinear active cochlear mechanics [108, 90], the nonlinearity of mechanotransduction is hypothesized to be the dominant source of nonlinearity in the cochlea. In the time domain, the current flowing through the HB, I_{hb}, is given by:

$$I_{hb} = G_a(\theta_{hb/rl})V + C_a\dot{V}, \tag{5.1}$$

where $G_a(\theta_{hb/rl})$ is the conductance of the HB and is a nonlinear function of the rotation of the HB relative to the RL, $\theta_{hb/rl}$, C_a is the OHC apical capacitance and V is the HB transmembrane potential. The pertubation in the HB current, i_{hb}, is given by:

$$i_{hb} = G_a^0 v_{hb} + C_a \dot{v_{hb}} + \Big[G_a(\theta_{hb/rl}) - G_a^0\Big]V_{hb}^s + \Big[G_a(\theta_{hb/rl}) - G_a^0\Big]v_{hb} \tag{5.2}$$

where V^s is the resting HB transmembrane potential, v is the pertubation of the HB transmembrane potential from its resting value and G_a^0 is the resting value of the HB conductance. The nonlinear term $\Big[G_a(\theta_{hb/rl}) - G_a^0\Big]v_{hb}$ is ignored, as it is small. The validity of this approximation as well as of the linearization of somatic motility can

be verified *a posteriori*. Eq. 5.2 is reduced to:

$$i_{hb} = G_a^0 v_{hb} + C_a \dot{v_{hb}} + \Big[G_a(\theta_{hb/rl}) - G_a^0 \Big] V_{hb}^s \tag{5.3}$$

where the HB conductance, $G_a(\theta_{hb/rl})$, is modeled by a nonlinear function. The effect of fast adaptation on mechanotransduction [128] is not included for simplicity. In agreement with experimental measurements of the response of the transduction channel to deflection [80], the transduction current is modeled by a simple saturating Boltzman function:

$$G_a(\theta_{hb/rl}) = G_a^{max} \frac{1}{1 + \exp\Big[- \frac{L_{hb}\theta_{hb/rl} - X_0}{\Delta X} \Big]}, \tag{5.4}$$

where G_a^{max}, X_0 and ΔX are defined as in Chapter II and L_{hb} is the length of the HB. In the time domain, the equations governing the nonlinear dynamics of the cochlea have the following form:

$$\mathbf{M}\ddot{\mathbf{d}} + \mathbf{C}\dot{\mathbf{d}} + \mathbf{K}\mathbf{d} + \mathbf{nl}(\mathbf{d}) = \mathbf{F} \tag{5.5}$$

where $\mathbf{M}$, $\mathbf{C}$ and $\mathbf{K}$ are the mass, damping and stiffness matrices (derived from the equations of Chapter II), $\mathbf{d}$ is the vector of the degrees of freedom (structural displacements, fluid pressures and potentials), $\mathbf{nl}(\mathbf{d})$ is a vector that is a nonlinear function of the vector $\mathbf{d}$ (due to mechanoelectrical transduction) and $\mathbf{F}$ is the external force vector.

5.2.2 Harmonic decomposition in the frequency domain

The Fourier components of any variable x are denoted as X_m. The values of the variable x at the discrete time $t_q = \frac{(q-1)T}{N_{FFT}}$, where q = 1,...,N_{FFT} and N_{FFT} is an integer, are denoted as x_p. The stationary response of the cochlea can be written as

$\mathbf{d(t)} = \sum_{m=0}^{\infty} \mathbf{D_m} exp(-im\omega_0 t)$ where ω_0 is the radian frequency of the excitation and each Fourier component $\mathbf{D_m}$ satisfies the following equation:

$$\Big[\mathbf{K} - im\omega_0\mathbf{C} - (m\omega_0)^2\mathbf{M}\Big]\mathbf{D_m} + \mathbf{NL_m}\Big[\mathbf{d}(t)\Big] = \mathbf{F_m} \tag{5.6}$$

Only a few Fourier components are used for the computation, as for any variable x,

$$x(t) = \sum_{m=0}^{\infty} X_m exp(-im\omega_0 t) \approx \sum_{p=1}^{N_h} X_{m(p)} exp(-im(p)\omega_0 t) \tag{5.7}$$

where N_h is the number of harmonic components used for the simulations and m is a function mapping the index p to one of the nonnegligible harmonic components.

For the problem solved here, the only nonlinear term is in the structural electrical coupling (due to the nonlinearity of mechanoelectrical transduction). Therefore we have solve N_h nonlinear systems of size N_{dof}, given by:

$$\begin{pmatrix} \mathbf{K_s} & \mathbf{Q_{sf}} & \mathbf{Q_{se}} \\ \mathbf{Q_{fs}} & \mathbf{K_f} & \mathbf{0} \\ \mathbf{Q_{es}^{Lin}} & \mathbf{0} & \mathbf{K_e} \end{pmatrix} \begin{pmatrix} \mathbf{U_m} \\ \mathbf{P_m} \\ \mathbf{\Phi_m} \end{pmatrix} + \begin{pmatrix} \mathbf{0} \\ \mathbf{0} \\ \mathbf{NL_m(u)} \end{pmatrix} = \begin{pmatrix} \mathbf{0} \\ (\mathbf{F_p})_\mathbf{m} \\ \mathbf{0} \end{pmatrix} \tag{5.8}$$

where $\mathbf{K_s}$, $\mathbf{Q_{sf}}$, $\mathbf{Q_{fs}}$, $\mathbf{K_f}$ and $\mathbf{K_e}$ are defined in Chapter II, $\mathbf{Q_{es}^{Lin}}$ is the part of the electrical structural matrix due to somatic electromechanical coupling and $(\mathbf{F_p})_\mathbf{m}$ is the m^{th} harmonic component of the forcing on the fluid due to the stapes vibrations. For a single tone stimulation, $(\mathbf{F_p})_\mathbf{m} = \mathbf{0}$ except for the fundamental.

5.2.3 Algorithm: alternating frequency/time scheme

An iterative algorithm, named alternating frequency time (AFT) method and developed by Cameron [13], is used to solve Eq. 5.8. The nonlinear forcing from the transduction current is calculated the time domain and then the solution of the

system is computed in the frequency domain. The algorithm alternates between the frequency and the time domains using the Fourier and inverse Fourier transforms. For the problem considered here, the algorithm, based on a fixed point iteration, is the following:

1. Start with an initial guess ($k = 0$) in the frequency domain $\mathbf{D}^{(\mathbf{0})}_{\mathbf{m(p)}}$ where p=1,...,N_h. We chose to start with $\mathbf{D}^{(\mathbf{0})}_{\mathbf{m(p)}} = \mathbf{0}$.

2. Start of iteration k. Calculate the HB deflection in the frequency domain $(\mathbf{U_{hb}})^{(\mathbf{k})}_{\mathbf{m(p)}}$, where p = 1,...,N_h, using the kinematic relation between the HB deflection and the BM and TM displacements.

3. Calculate the inverse fast Fourier transform (IFFT) of the HB deflection to obtain $(\mathbf{u_{hb}})^{(\mathbf{k})}_{\mathbf{q}}$, where $q = 1,...,N_{FFT}$.

4. Calculate the nonlinear function $\mathbf{nl(u)}$ at the discrete times t_q, $\mathbf{nl}(\mathbf{u_{hb}})^{(\mathbf{k})}_{\mathbf{q}}$, where $q = 1,...,N_{FFT}$, using Eq. 5.4.

5. Calculate the fast Fourier transform (FFT) of the funtion $\mathbf{nl(u)}$ to obtain the nonlinearity in the frequency domain $\mathbf{NL}(\mathbf{u})^{(\mathbf{k})}_{\mathbf{m(p)}}$

6. Solve the N_h linear systems given by Eq. 5.8. The nonlinear term is set to $\mathbf{NL}(\mathbf{u})^{(\mathbf{k})}_{\mathbf{m(p)}}$. The solution of the system is denoted as $\mathbf{D}^{(\mathbf{k+1})}_{\mathbf{m(p)}}$

7. Check for convergence. If converged, stop. If not, start the iteration $k + 1$.

For the DC shift, the algorithm described here does not converge. Therefore, a modified Newton's iteration is used instead of the fixed point iteration. To limit the computational cost, the matrix $\frac{\partial \mathbf{NL(u)}}{\partial \mathbf{U}}$ is calculated only once, at the start of the first iteration. The other components of the response are computed with a fixed point iteration.

5.2.4 Implementation of the algorithm

At each iteration, the algorithm requires the solution of a $n_{dof} \times n_{dof}$ linear system (where n_{dof} is the number of degrees of freedom) for each harmonic component. However, the matrix of the system depends only on the frequency but is independent of the magnitude of the degrees of freedom and of the iteration. A LU decomposition algorithm is used to solve the linear systems. A typical simulation requires the computation of the solution for different magnitudes of stapes displacement (N_{input} different magnitudes of stapes displacement) at different frequencies (N_{freq} different frequencies). To mimimize the computational cost, the computation is carried out in the following order:

1. For one input frequency, calculate the matrices of the system for each harmonic component.

2. Compute the LU decomposition of the systems.

3. Compute the harmonic component of the solution for each magnitude of stapes displacement using the AFT algorithm and the LU decomposition previously computed.

4. Repeat the process for the next input frequency.

This implementation of the algorithm requires the storage in memory of the LU decomposition of N_h matrices of size $n_{dof} \times n_{dof}$. The matrices are stored in memory using profile storage. The number of operations necessary to factorize each matrix is $c_1 = O(n_{dof} b^2)$ where b is the bandwidth of the matrix. The number of operations required to solve the system is $c_2 = O(n_{dof} b)$ for each iteration of the algorithm. The overall computation cost is:

$$c_{tot} = \Big[n_{dof} b^2 + N_{iter} N_{input} n_{dof} b \Big] N_h N_{freq}, \tag{5.9}$$

where N_{iter} is the number of iterations required for convergence. The required memory and the computation time grow linearly with the number of harmonic components. From a convergence study a low number of harmonic components is required (see 5.3.1). Instead of checking for convergence using a convergence criterion, the algorithm is considered to have converged when the number of iterations, N_{iter}, reaches 30 (for reasons discussed in 5.3.1).

5.3 Nonlinear response of the cochlea to single tone

5.3.1 Convergence and performance of the algorithm

The alternating time/frequency method introduces numerical error in the solution, due to three approximations: the finite number of discrete time points used for the FFT calculations, N_{FFT}, the finite number of harmonic components, N_h, and the finite number of iterations, N_{iter}. N_{FFT} does not really affect the computational cost of the algorithm for the problem considered here and can be chosen sufficiently high (128 in the simulations) to obtain accurate results.

The relative error in the BM displacement (see Appendix F) is plotted as a function of the number of iterations in Fig. 5.1, at CF and at CF/2. The fundamental does not require a high number of iterations to converge to the solution. After 20 iterations the relative error in the fundamental is already less than 0.1. However for the DC shift, 2nd and 3rd harmonic components, a higher number of iterations is required for better accuracy (especially at the 2nd harmonic). After 30 iterations the error is less than 0.1 at CF and about 0.1 at CF/2, which is sufficient for our simulations. The relative error is plotted as a function of N_h in Fig. 5.2 at CF and at CF/2. For all the harmonic components the relative error tends to decrease as the number of computed harmonic component increases. Obtaining the fundamental with a reasonable accuracy only requires the computation of the fundamental, as

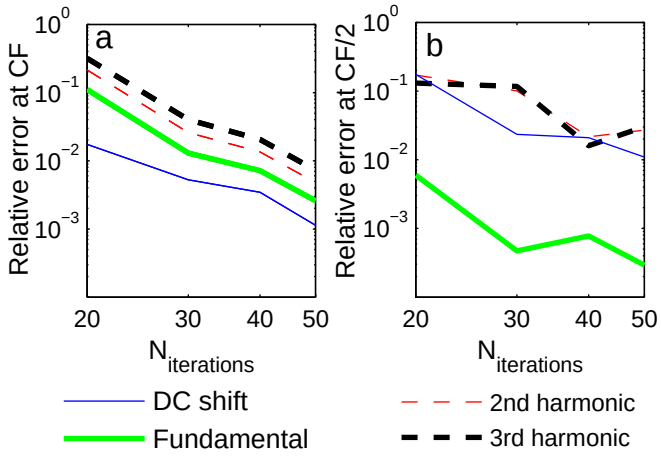

Figure 5.1: Relative error in the BM displacement as a function of the number of iterations. The error is computed at CF (a) and at CF/2 (b) for the different harmonic components. The converged solution used as a reference for the computation of the relative error (see Appendix F) is the solution after 60 iterations. For all the simulations four harmonic components (the DC shift, the fundamental, the 2nd harmonic and the 3rd harmonic) are computed.

the relative error is about 0.01 both at CF and CF/2. The DC shift and the 2nd harmonic component requires the computation of three components (the DC shift, the fundamental and the 2nd harmonic). The 3nd harmonic requires the computation of four components. The number of iterations and harmonic components required to obtain the converged components of the response of the BM, as well as the required memory and computational time are summarized in Table 5.1. If the simulation is run for only one magnitude of stapes displacement the nonlinear model is more expensive than the linear model. However if the simulation is run for many different magnitude of stapes displacement (or many different activity levels with the linear model) the computational cost per harmonic component in the nonlinear model is lower than the cost for the fundamental in the linear model.

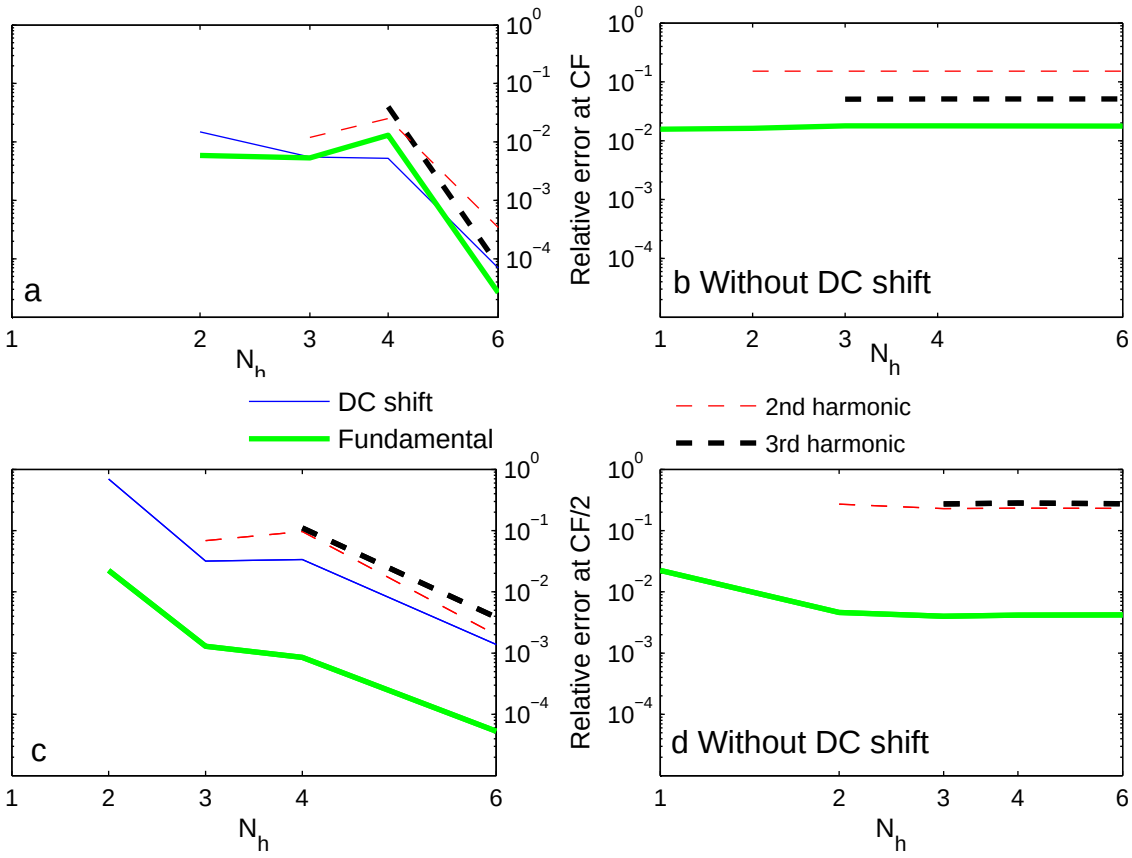

Figure 5.2: Relative error in the BM displacement as a function of the number of harmonic components. The error is computed at CF (a and b) and at CF/2 (c and d). In a and c the DC shift is one of the computed component. In b and d the DC shift is not computed. The converged solution used for reference for the computation of the relative error (see Appendix F) is the solution with with 8 harmonic components (including the DC shift). All simultations are with 30 iterations.

Table 5.1: Number of harmonic components, number of iterations, memory and computational time required for convergence.

Component	N_h	N_{iter}	Required RAM	Computational time $N_{freq} = 1$ $N_{input} = 1$	Computational time $N_{freq} = 200$ $N_{input} = 15$
Fundamental	1	< 20	1.40GB	13s	4.5 hours
DC	3	30	2.32GB	52s	22.0 hours
2nd harmonic	3	30	2.32GB	52s	22.0 hours
3rd harmonic	4	30	3.77GB	68s	28.2 hours
Linear	1	1	0.688GB	10s	8.4 hours

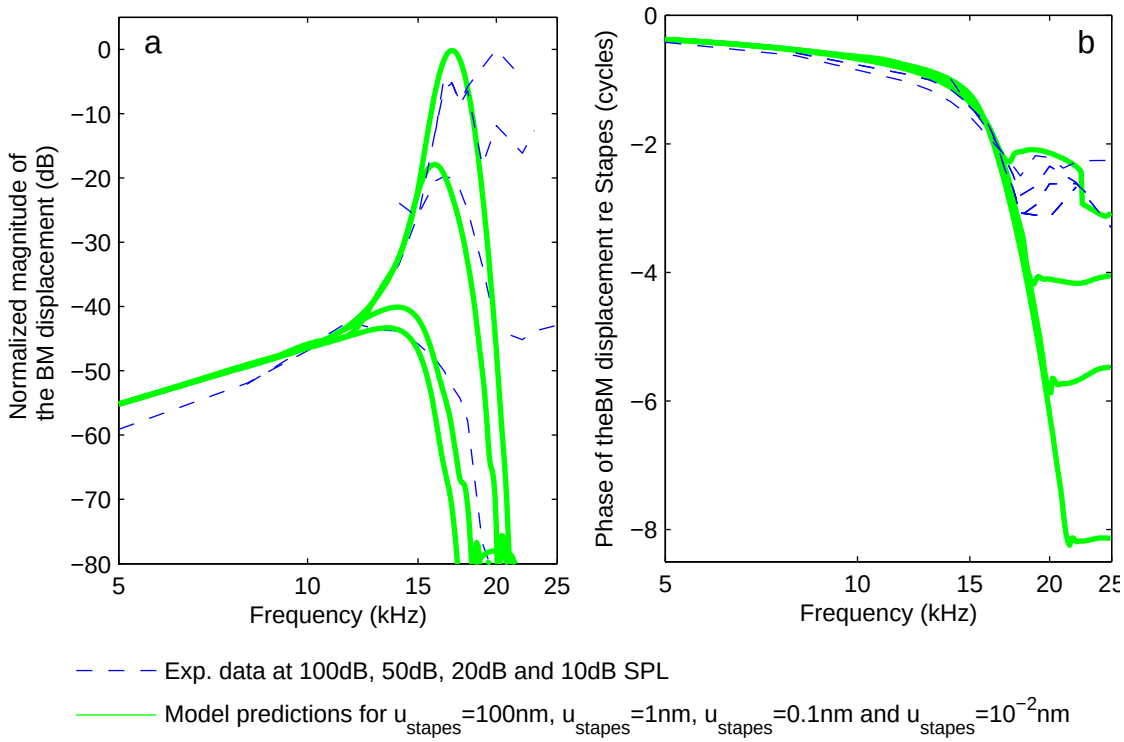

Figure 5.3: Magnitude and phase of the fundamental of the BM displacement at the 17kHz BP in response to a single tone. a. Normalized magnitude of the gain and b. phase of the the fundamental of the BM displacement (relative to the stapes) at the 17kHz BP in response to a single tone, plotted as a function of frequency. Solid lines: model predictions for a $10^{-4}nm$, $10^{-2}nm$, $1nm$, and $100nm$ stapes displacement. Dashed lines: experimental data from Cooper [20] for a 100dB, 50dB, 20dB and 10dB SPL acoustic stimulation. Both for the experimental data and for the model predictions, the gain are normalized to the value of the gain at the lowest intensity of stimulation.

5.3.2 Fundamental of the BM displacement in response to a single tone

The magnitude and phase of the fundamental of the BM displacement in response to harmonic vibrations of the stapes are plotted as a function of frequency at the 17kHz BP in Fig. 5.3. The model predictions compare nicely with the measured magnitude of the BM displacement (Fig.5.3(a)) to acoustic stimulation by Cooper [20]. At low intensity, the response is sharp and highly sensitive. As the intensity of the stimulation is increased, the response peak shifts to a lower frequency, the response is less sharply tuned and less sensitive, as seen in the experimental data. At frequencies significantly lower than the CF, the gain is independent of the intensity of the stimulus; this indicates a linear response. At CF, the gain is higher at low intensity than at high intensity, indicative of a compressive nonlinearity. The predictions for the phase of the BM displacement relative to the stapes, shown in Fig. 5.3, exhibit the commonly observed trends in the BM response to acoustic stimulation [110, 20, 159]. The slope of the phase curve at CF is steeper and the value of the phase at CF is slightly higher at low intensity than high intensity; the phase slope and the value of the phase at CF (about 3 cycles) are similar to the values from Cooper [20]. Compared to the experimental data, the phase accumulation at frequencies higher than CF is predicted to be higher (about 8 cycles) than in the measurements (about 3 cycles); however the measurements at frequencies significantly higher than the CF at low intensity of stimulation are not reliable, as the magnitude of the BM displacement is very small.

The dependence of the BM response on the intensity of stimulation is quantitatively analyzed in Fig. 5.4. In Fig. 5.4(a) the BM displacement at CF (17kHz) is plotted as a function of the stapes displacement. In agreement with the results of Fig. 5.3(a), the model predicts a compressive nonlinearity at CF, as observed in the experimental data from Zheng *et al.* [159] and Cooper [20]. However, contrary to both sets of experimental data, the BM response is linear at very low intensity (up to

about $2 \times 10^{-4} nm$ of stapes displacement). Moreover, the BM displacement is also predicted to be linear at very high intensity (more than 2nm of stapes displacement); this cannot observed in the experimental data as such a high intensity of stimulation would likely damage the cochlea. The phase of the BM displacement relative to the stapes at CF is plotted as a function of the stapes displacement in Fig. 5.4(b). As observed in [110] the phase lag of the BM displacement relative to the stapes is reduced as the intensity of stimulation is increased. However the change in the phase is limited (less than 140 degrees). The mechanical quality factor, Q_{10dB}, is shown to decrease as the magnitude of the stapes displacement is increased in Fig. 5.4(c), from a value of 6.5 to 1.4. The peak frequency at the 17kHz best place decrease from 17kHz at the lowest intensity of excitation to 13.3 kHz at the highest intensity (Fig. 5.4(d)).

5.3.3 Comparison of the predictions of the nonlinear model to the predictions of the nonlinear model

The predictions of the magnitude and phase of the BM displacement in response to acoustic stimulation by the linear model (described in Chapter II) and by the nonlinear model of the cochlea are compared in Fig. 5.5. The activity levels of the linear model are chosen so that the gain of the BM displacement predicted by the linear model matches the gain of the BM displacement predicted by the nonlinear model. The linear model with an activity of 100% corresponds to the consistent linearization of the nonlinear model for small harmonic stimuli. Therefore, as expected, the 100% active linear model and the nonlinear model with a very small stapes displacement predict the same sharply tuned and highly sensitive BM response. For very large stimuli (a $100nm$ stapes displacement), the passive linear model (0% activity) and the nonlinear model also predict the same poorly tuned response. However, at intermediate intensity, the predictions of the linear model with the appropriate activity

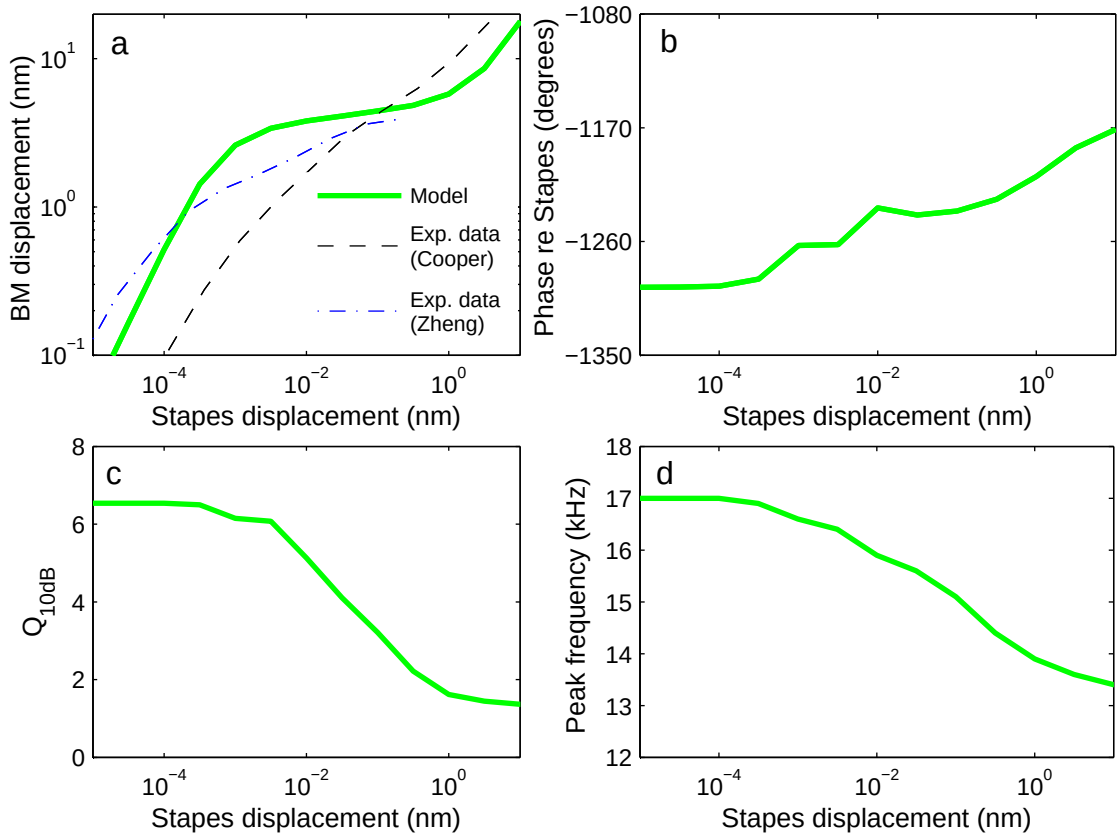

Figure 5.4: Dependence of the BM response to single tone acoustic stimulation at the 17kHz BP on the magnitude of stapes displacement. a BM displacement at CF. The model predictions (thick solid line) are compared to the measurements from Zheng [159] (dashed-dotted line) and Cooper [20] (dashed line) in the guinea pig cochlea. b Phase relative to the stapes at CF. c Mechanical quality factor Q_{10dB}. d Peak frequency. The predictions are plotted as a function of the stapes displacement.

have small quantitative differences with the predictions of the nonlinear model. The peak frequency predicted by the linear model is slightly higher than predicted by the nonlinear model. Moreover, the phase accumulation at high frequencies does not match the predictions by the nonlinear model. In the linear model the saturation of the MET channel is assumed to be uniform (and modeled by an activity level between 0% and 100%), which is not the case in the nonlinear model. Therefore differences in the predictions by the two models are to be expected. But overall there is good qualitative agreement between the nonlinear and linear models.

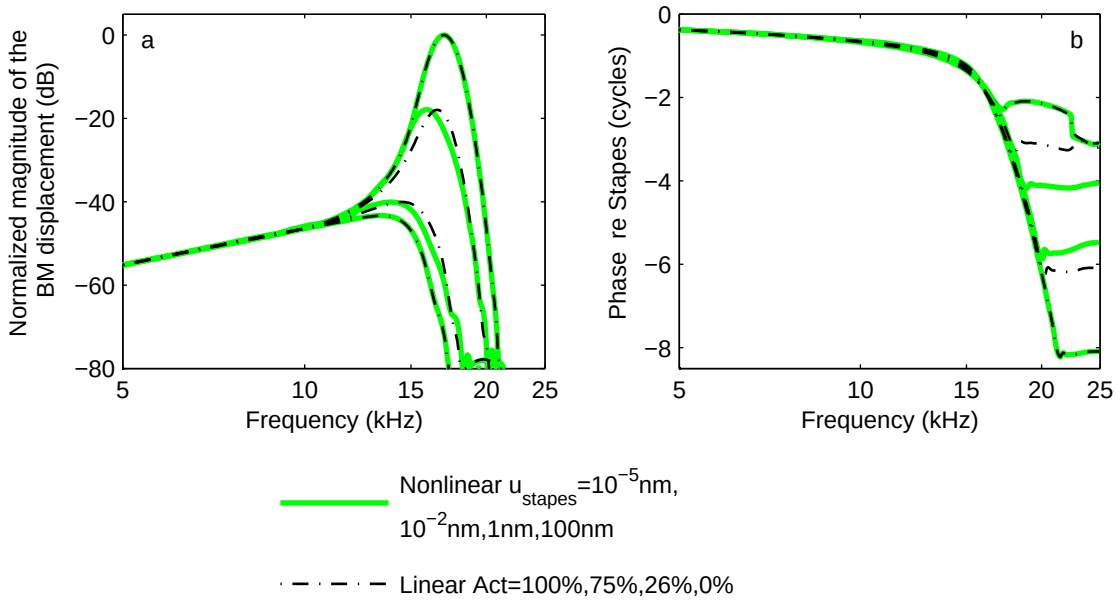

Figure 5.5: Comparison of the predictions by the nonlinear and linear models of the magnitude and phase of the BM displacement at the 17kHz BP. a. Normalized magnitude and b. phase of the fundamental of the BM displacement at the 17kHz BP predicted by the nonlinear and linear models, plotted as a function of the frequency of the fundamental. Thick solid lines: nonlinear model predictions for a stapes displacement of $10^{-5}nm$, $10^{-2}nm$,$1nm$ and $100nm$. Thin dashed lines: linear model predictions with an activity (see Chapter II) of 100%, 75%, 26% and 0%.

5.3.4 Harmonic distortion on the BM response to acoustic stimulation

Harmonic distortion has been reported in the BM response to acoustic stimulation [23, 20, 124, 118]. The nonlinearity of the MET channel generates harmonic distortion in the model. The magnitudes of the fundamental, 2nd harmonic and 3rd harmonic of the BM displacement at the 17kHz best place in response to stapes displacement are plotted as a function of the frequency of the fundamental in Fig. 5.6(a), for a large stapes displacement ($3.16nm$). The model predictions are in good qualitative agreement with the experimental data from Cooper in the base of the guinea pig cochlea [20]. At this intensity of stimulation, the peak of the fundamental is at about 15kHz. The 2nd harmonic has two main peaks: one for a fundamental frequency close

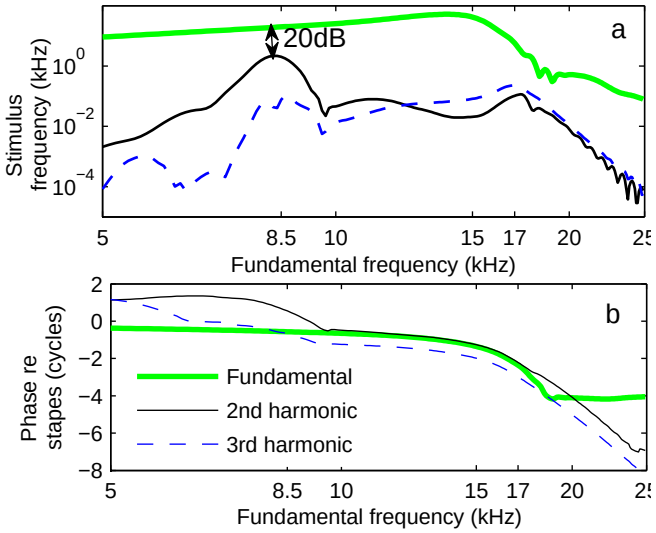

Figure 5.6: Magnitude and phase of the harmonic distortion components as a function of frequency. The magnitude of the fundamental, 2nd harmonic and 3rd harmonic of the BM displacement in response to stapes vibrations at the 17kHz best place, are plotted as a function of the frequency of the fundamental, for a 3.16nm stapes displacement. Thick solid line: fundamental. Thin solid line: 2nd harmonic. Thin dashed line: 3rd harmonic. a Magnitude b. Phase. The phase of the 2nd harmonic has been divided by two and the phase of the 3rd harmonic has been divided by three

to CF (17kHz) and one for a fundamental frequency equal to CF/2 (8.5kHz). The peak at CF/2 is predicted to be 20dB lower than the value of the fundamental at the same frequency; Cooper [20] measured a difference of 11dB. The 3rd harmonic has three peaks: one at CF, one at CF/2 and one at CF/3. To analyze the propagation of the 2nd and 3rd harmonic on the BM, the phase of the 2nd harmonic and 3rd harmonic have been respectively divided by two and three and plotted as a function of the fundamental frequency along with the phase of the fundamental in Fig. 5.6(b). The fundamental and the 2nd harmonic (respectively 3rd harmonic) have the same group velocity if the phase of the 2nd harmonic divided by two (resp. of the 3rd harmonic divided by three) has the same slope as the phase of the fundamental. The phase predictions of Fig. 5.6 indicate that for frequencies between 10 and 15kHz, 2nd harmonic and 3rd harmonic propagate along with the fundamental. This means that as the wave travels on the BM, the signal is distorted but the distorted components do not travel indepently of the fundamental; distortion is locally generated, as suggested by the fluid pressure measurements in [114]. However, for frequencies between 7 and 10kHz and between 15 and 25kHz, the 2nd harmonic travels indepently of the fundamental as the phase slope of the 2nd harmonic divided by two does not match or run parallel to the phase of the fundamental.

The generation and propagation of harmonic distortion can be better analyzed by looking at the spatial plot of magnitude and phase of the fundamental and 2nd harmonic, shown in Fig. 5.7. In Fig. 5.7(a) and (b) the magnitude and phase of the fundamental and 2nd harmonic are plotted as a function of x for a 8.5kHz tone with a $3.16nm$ stapes displacement; in Fig. 5.7(c) the fundamental and 2nd harmonic component of the force delivered by somatic motility are plotted as a function of x for a 8.5kHz tone. From $x = 0.2$ to $x = 0.3$ the fundamental travels on the BM and generates locally harmonic distortion; the 2nd harmonic does not propagate indepently of the fundamental. However, as the wave approaches the 17kHz BP

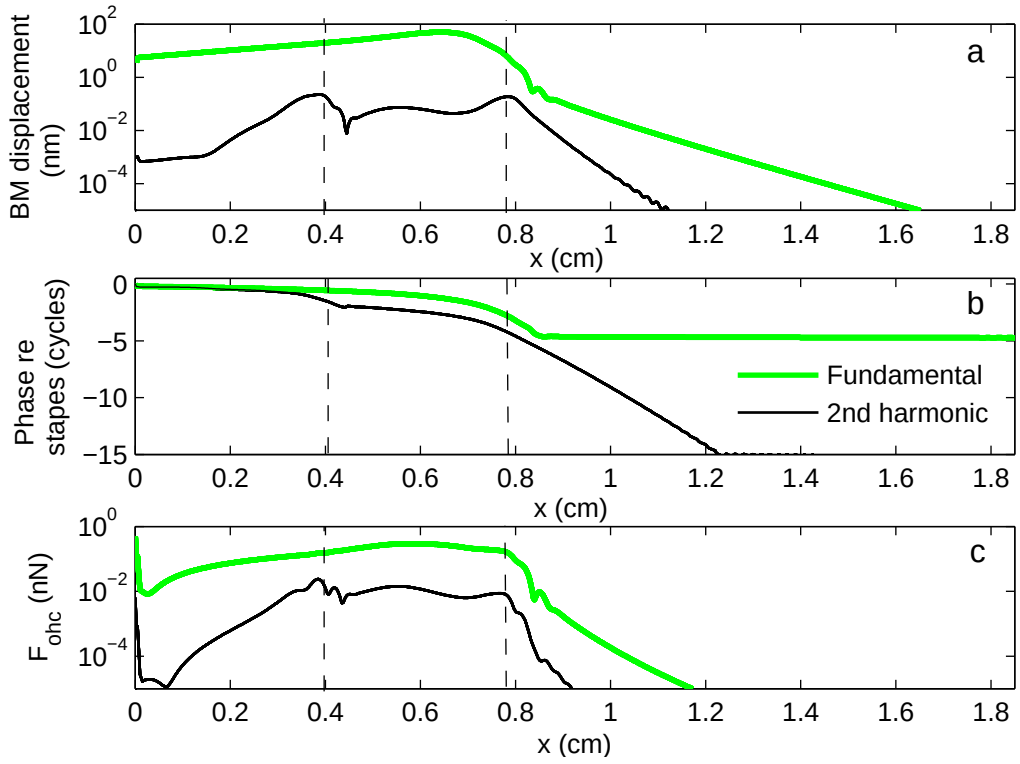

Figure 5.7: Magnitude of the fundamental and 2nd harmonic of the BM displacement and force delivered by somatic motility in response to stapes vibrations plotted as a function of the distance x. The magnitude of the stapes displacement is $3.16nm$. Thick solid line: fundamental. Thin solid line: 2nd harmonic. a Magnitude of the BM displacement b. Phase of the BM displacement relative to the stapes. The phase of the 2nd harmonic has been divided by two. c. Force delivered by somatic motility. The BP for a 8.5kHz tone ($x = 0.78cm$) and for a 17kHz ($x = 0.4cm$) tone are indicated by a dashed vertical line.

(x=0.4cm), the 2nd harmonic is amplified (because the frequency of the 2nd harmonic is close to the CF) by the somatic force (the 2nd harmonic of the somatic force reaches a maximum slightly basally of the 17kHz BP) and can travel indepently of the fundamental. The traveling wave of the 2nd harmonic becomes an evanescent wave after the 17kHz BP since its magnitude decreases quickly as x increases. Distortion is again locally generated from $x = 0.45cm$ to $x = 0.75cm$. Then the 2nd harmonic propagates indepently of the fundamental and reaches a peak close to the 17kHz BP.

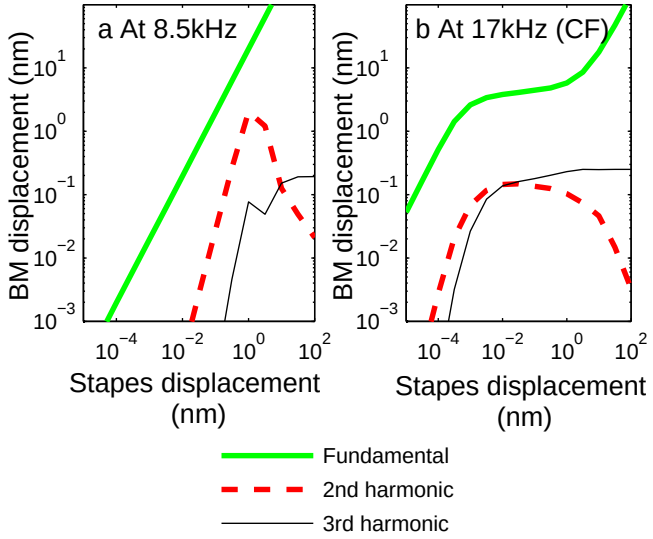

Figure 5.8: Magnitude of the fundamental and 2nd and 3rd harmonic components of the BM displacement as a function of the stapes displacement at the 17kHz BP. a. For a 8.5kHz tone. b. For a 17kHz tone

The level and frequency dependent characteristics of harmonic distortion, can also be analyzed in a plot of the magnitude of the fundamental and harmonic distortion components at different frequencies as a function of the stapes displacement, as shown in Fig. 5.8. For a fundamental frequency of 8.5kHz (Fig. 5.8(a)) the response of the fundamental is linear. The 2nd and 3rd harmonic exhibit an expansive nonlinearity (as the slope is greater than $1dB/dB$) at moderate intensities, as observed in [20]. When the intensity of the stimulus is further raised, the magnitude of the harmonic distortion components decreases. At CF (Fig. 5.8(a)), the fundamental exhibits a compressive nonlinearity, as shown in Fig. 5.4(a). The 2nd and 3rd harmonic are

predicted to have a fast growth with respect to increase in the stapes displacement for small stapes displacement. For higher stapes displacement the 3rd harmonic grow slowly with respect to the stapes displacement, and the 2nd harmonic decreases for stapes displacement greater than about $1 \times 10^{-2} nm$. In the data from Cooper at CF [20], the 2nd and 3rd harmonic are lower than the noise floor for low SPL and both grow slowly as the level of stimulation is increased.

5.3.5 DC shift

Despite the presence of even order distortion on the BM [23, 20], there is only limited evidence for a DC shift in the BM displacement [23] at the base. Due to the nonsymmetry of the MET channel (a non zero value for X_0 in Eq. 5.4), the model predicts a DC shift in the BM displacement. The fundamental and the DC shift in the BM displacement are plotted as a function of the stapes displacement at the 17kHz BP for a 17kHz single tone in Fig. 5.9(a). At all intensities the DC shift is predicted to be positive, which means that the BM moves toward the scala vestibuli. At very low intensity of stimulation, the DC shift is very small compared to the fundamental. In the data from Cooper and Rhode [23] in the hook region (very high frequency) region of the cochlea the DC shift is under the noise floor and cannot be measured at low intensity. At higher intensity the DC shift is predicted to have the same order of magnitude as the fundamental, with a value of about $3nm$ for a $10^{-2} nm$ BM displacement. For very high intensity the DC shift saturates and reaches a value of about 6 nm. This prediction is significantly higher than the value measured by Cooper and Rhode in the hook region of the cochlea of the cat (a DC shift toward the scala vestibuli of 0.2nm at 100dB SPL for a 20kHz tone at the 30kHz BP). However, in addition to a possible difference due to the different frequency region and species, higher values of the DC shift are expected closer to or at CF since the cochlear amplifier has a more dramatic effect on the BM vibrations close to the CF,

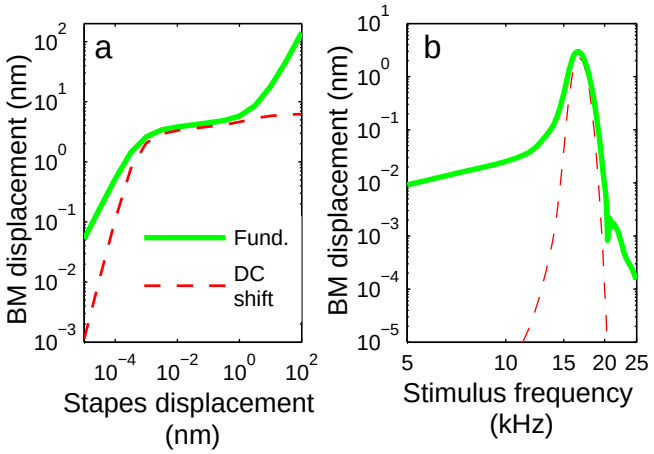

Figure 5.9: Fundamental and DC shift in the BM displacement. The fundamental is shown with a thick solid line and the DC shift with a thin dashed line. (a) at CF as a function of the stapes displacement (b) as a function of frequency for a $3.16 \times 10^{-2} nm$ stapes displacement.

as shown in Fig. 5.9(b). The fundamental and DC shift are plotted as function of frequency for a small stapes displacement in Fig. 5.9(b). At low intensity the DC shift is predicted to be tuned to the same frequency as the fundamental, with a sharper tuning than the fundamental.

5.3.6 OHC transmembrane potential

In the model cochlear amplification is due to somatic motility driven by the OHC transmembrane potential. The DC shift and harmonic distortion in the BM response arise from the DC shift and harmonic distortion in the transmembrane potential caused by the the saturation of the MET channels. Therefore the transmembrane potential is an important prediction of the model. Unfortunately due to the difficulty in measuring the OHC intracellular potential in a sensitive preparation, there is only one set of *in vivo* experimental data, from Kössl and Russell [85], that can be used for comparison. The fundamental of the transmembrane potential is predicted to grow linearly at low intensity in Fig. 5.10(a). The model predicts a fundamental of about 2.5mV and a positive DC shift of about 20mV at high intensity. Kössl and Russell[85]

measured a similar level dependence for the transmembrane potential, but a lower magnitude, with an AC part of about 1mV (if uncorrected for the RC cutoff) and a positive DC shift of about 5mV at 100dB SPL. As discussed in Chapter IV, the measurements are likely to underestimate the *in vivo* transmembrane potential. The 2nd and 3rd harmonic in the transmembrane potential exhibit the same level dependence as the same components of the BM response. In Fig. 5.10(b) the transmembrane potential is shown to be sharply tuned to CF at low intensity of stimulation.

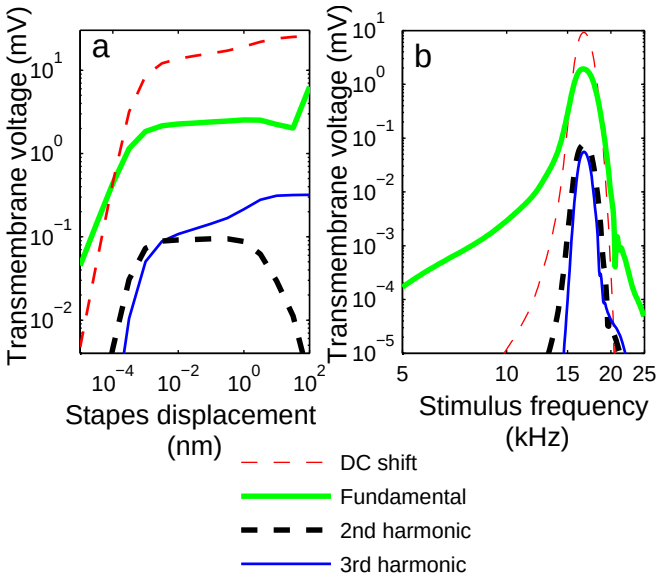

Figure 5.10: DC shift, fundamental, 2nd harmonic and 3rd harmonic in the OHC transmembrane potential. (a) at CF as a function of the stapes displacement (b) as a function of frequency for a $3.16 \times 10^{-2} nm$ stapes displacement.

5.4 Discussion

5.4.1 The saturation of the HB mechanotransduction channel is the dominant source of nonlinearity

The model predicts the nonlinear compressive response of the BM response to acoustic stimulation because of the saturation of the MET channels. All other sources

of nonlinearity are neglected, including the nonlinearity of somatic motility. The validity of this approximation can be assessed based on the value of the transmembrane potential predicted by the model. The fundamental and DC shift in the OHC transmembrane potential are predicted to be about respectively $2.5mV$ and $20mV$ at very high intensity. For a $20mV$ transmembrane potential change He and Dallos [61] measured a change in the somatic stiffness of less than 10%. Therefore, given the predicted magnitude of the DC and AC values of the transmembrane potential in response to acoustic stimulation *in vivo*, somatic motility can be approximated to be linear. The same conclusion was reached by Liu and Neely [90], although their model did not include BM displacement and transmembrane potential DC shifts.

The second linear approximation concerns the term $\left[G_a(\theta_{hb/rl}) - G_a^0\right] v_{hb}$ that is neglected in Eq. 5.2. At high intensity ($u_{stapes} = 1nm$) the value of the DC shift and fundamental in the HB transmembrane potential are predicted to be respectively $25mV$ and $9mV$. These values are about one order of magnitude lower than the resting HB transmembrane potential (146mV at the 17kHz BP). Therefore the term $\left[G_a(\theta_{hb/rl}) - G_a^0\right] v_{hb}$ can be neglected as a first order approximation.

As discussed in Chapter IV, the HB force cannot contribute signicantly to cochlear amplification and nonlinearity and does not need to be included in the computation. However fast adaptation of the transduction current (which is not included in the nonlinear model) can have a significant effect on amplification by somatic motility (as discussed in chapter IV). In addition to its effect on the amplification at the lowest intensity of stimulation, fast adaptation could have an effect on the nonlinear growth of the fundamental of the BM response since fast adaptation depends on the magnitude of the HB deflection.

5.4.2 Harmonic distortion generation and DC shift

The model predictions for harmonic distortion on the BM are in good agreement with the data from Cooper [20]. The highest distortion component is the 2nd harmonic, which is mostly present in the response at frequencies close to CF and close to CF/2. Moreover the predictions of the phase of harmonic distortion show that the 2nd harmonic can travel indepently of the fundamental, as shown by the pressure measurements from Olson[114] in a sensitive cochlea. However, note that, contrary to the experimental data [20], the 2nd harmonic main peak is at different frequency than the peak of the fundamental at high intensity of stimulation. The origin for this discrepancy between the model predictions and the experimental data is not clear, but might be due to some deficiencies in the micromechanical model of the organ of Corti.

The generation of the 2nd harmonic requires the nonlinearity of the MET channel to be noncentered (X_0 not equal to 0) which generates a DC shift in the BM displacement. A DC shift was observed by Cooper and Rhode [23] but the magnitude of the DC shift predicted by the model is higher than the measured value. One of the possible reason for this quantitative difference is that slow adaptation of the transduction current, which is not included in the model, might act as a high pass filter that filters out the DC component. Much larger DC shifts have been measured at apical locations [24].

5.4.3 Efficient method to compute the stationary response of the cochlea

The AFT method used here to compute the response of the cochlea to a single tone is computationally efficient. As the number of nonlinear equations is very low in cochlear mechanics, the computational cost of the FFT calculations is not significant. Moreover, because the nonlinearity in cochlear mechanics is weak, only a few harmonic components are required for good accuracy. Therefore the method is much faster than

a time domain method [90] and is more flexible and accurate than the Quasi-Linear method [75]; it is reduced to the Quasi-Linear method if only the fundamental of the response is computed. It is simpler to implement than the harmonic balance method [88]. The AFT scheme is similar to the algorithm used by Nobili and Mammano [108]. However a convergence study was carried out here to compute only the harmonic components that have an effect on the BM vibrations. The algorithm presented here can be extended to predict the stationary response of the cochlea to two tones, such as two tone suppression and distortion products.

CHAPTER VI

Nonlinear response of the cochlea to two tones: two tone suppression and distortion products

6.1 Introduction

Two tone suppression and distortion products are interesting nonlinear characteristics of the response of the cochlea to two tones. Two tone suppression has been observed in the auditory nerve fibers [138] and in the response of OHC and IHC [143, 109] and of the BM [135, 111, 19, 51, 124] to acoustic stimulation. In this chapter we are interested in the prediction of suppression in the BM response to acoustic stimulation. Two types of suppression are observed in response to two tones, depending on the value of the suppressor tone compared to the probe tone. High side suppression is the case where the frequency of the suppressor is higher than the frequency of the probe; low side suppression is the case where the frequency of the suppressor is lower than the frequency of the probe. Two tone suppression on the BM is hypothesized to arise from the saturation of the cochlear amplifier [53, 76].

The other type of nonlinear two tone interaction, distortion products, has been recorded in the nerve fibers [12], IHC [113], BM [131, 132, 26, 64, 124] and intracochlear pressure [40] and is considered to be the source of DPOAEs. Both in DPOAEs measurements and in BM displacement measurements, the distortion prod-

uct most commonly measured in response to two tones of frequencies f_1 and f_2 and with the highest magnitude are the cubic terms $2f_1 - f_2$ and $2f_2 - f_1$. The generation and propagation of distortion products on the BM are simulated in this chapter.

Due to the nonlinearity of mechanotransduction, the model of the cochlea presented in Chapter V can be used to predict the stationary response of the cochlea to two tones. The adaptation of the method of Chapter V to the simulation of two tone interaction is first described. Then the predictions of the model of two tone suppression and two tone distortion on the BM are analyzed. The comparison to measurements of suppression and distortion products on the BM as well as the mechanisms for suppression, distortion products generation and propagation are discussed.

6.2 Methods

6.2.1 Algorithm and choice of the harmonic components

As in Chapter V, the Alternating Frequency/Time [13] scheme is used to compute the stationary nonlinear response of the cochlea. When the cochlea is stimulated by two primary tones, of frequency f_1 and f_2 (where f_1 and f_2 are not incommensurate frequencies), the cochlea generates distortion products at combination frequencies (of the form $n_1 f_1 + n_2 f_2$, where n_1 and n_2 are signed integers). Since f_1 and f_2 are not incommensurate frequencies, we can find a radian frequency ω_0 such that f_1 and f_2 are multiples of $2\pi\omega_0$. The response of the cochlea is decomposed as $\mathbf{d}(\mathbf{t}) = \sum_{p=1}^{N_h} \mathbf{D_m}(\mathbf{p}) exp(-im(p)\omega_0 t)$. The N_h harmonic components are chosen in the following order:

1. The first three components are the DC shift and the response to the two primaries.

2. The two cubic distortion components, $2f_1 - f_2$ and $2f_2 - f_1$ are computed, if they correspond to a positive frequency.

3. If there are other components to be computed, the component with the lowest minimum of the difference between its radian frequency ($m(p)\omega_0$) and the radian frequency $2\pi f_1$ and of the difference between its radian frequency and the radian frequency $2\pi f_2$ is first computed. The same criterion is then applied to choose among the remaining components, until N_h components have been computed.

6.2.2 Convergence and performance of the algorithm

Similarly to single tone simulations (Chapter V), the accuracy of the solution depends on the number of iterations, $N_{iterations}$, and on the number of harmonic components, N_h. The influence of the number of iterations for two tone simulations is not studied here; 30 iterations are used for all the simulations. The convergence of the algorithm with respect to the number of harmonic components, N_h, for the computation of two tone interaction is described next.

The objective of the two tone supression simulations is to accurately predict the magnitude of the probe tone, particularly at its BP. The relative error in the probe and suppressor components of the BM displacement at the BP of the probe component ($x = 0.4cm$) and the root mean square (RMS) value (over the length of the cochlea) of the relative error are plotted as a function of the number of harmonic components in Fig. 6.1 for a high side (23kHz) and for a low side suppressor (10kHz). The equations used to compute the relative error and the RMS value of the relative error are in Appendix F. Both for the low side and for the high side suppressor, only the computation of the probe and suppressor components are necessary to accurately compute the probe and suppressor components of the response, as the relative error is than 10^{-2} at the probe BP and the RMS value of the relative error is less than 0.1, which is sufficient for our analyses.

The primary goal of the distortion products simulation is to compute the cubic distortion component, $2f_1 - f_2$. The convergence of the algorithm for the simulations

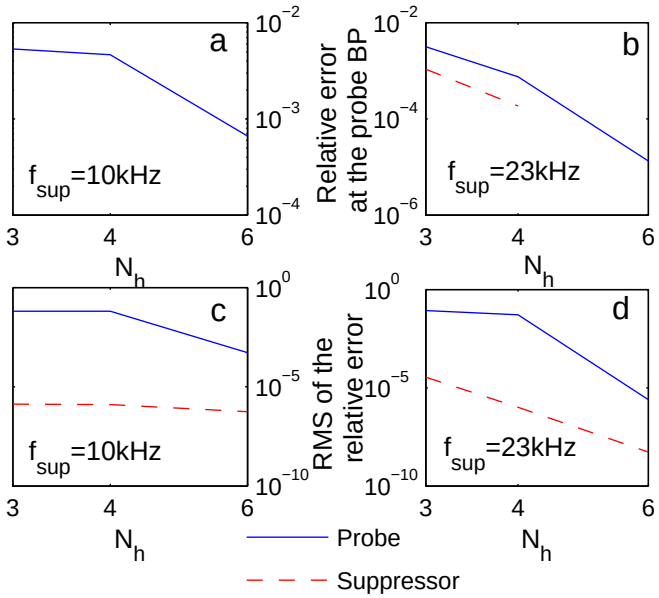

Figure 6.1: Error in the BM displacement as a function of the number of harmonic components for two tone suppression simulations. The magnitude of the probe component of the stapes displacement is 0.01nm; the magnitude of the suppressor component is 3.16nm. In a and c the frequencies of the primaries are f_{probe} = 17kHz and $f_{suppressor}$ = 10kHz. In b and d the frequency of the primaries are f_{probe} = 17kHz and $f_{suppressor}$ = 23kHz. The error in the probe component of the BM displacement at the 17kHz BP ($x = 0.4cm$) is plotted in a and b; the root mean square (RMS) value (over the length of the cochlea) of the relative error is plotted in c and d. The converged solution used as a reference in the computation of the error (see Appendix F) is the solution with 10 harmonic components. The points that do not appear on the plot correspond to errors that are too small too be measured.

of distortion products on the BM is analyzed in Fig. 6.2. If the frequency of the primaries are not too close to each other (for example a ratio f_2/f_1 of 1.26 in Figs. 6.2(a) and (b)), only four components (the DC shift, the two primaries and the $2f_1-f_2$ component) are required to accurately compute the value of the $2f_1 - f_2$ component (the RMS value of the relative error is about 10^{-6} with four harmonic components). The solution with four harmonic components is indistinguishable from the solution with 14 components in Fig. 6.2(e). However, if the frequencies of the two primaries are closer to each other (a ratio f_2/f_1 of 1.1 in Fig. 6.2(c) and (d)), a higher number of harmonic components is required. At the 17kHz BP, the error is reasonable for 4 harmonic components (the relative error is less than 0.1); but the RMS value of the relative error is almost 0.1 with 4 harmonic components. Some small differences can be seen in Fig. 6.2(f) between the solution with four components and the solution with 14. With 12 harmonic components, the RMS value of the relative error is less than 10^{-2}.

6.2.3 Energy delivered by somatic motility

The average power delivered by somatic motility to the harmonic m of the solution is given by:

$$(P_{som})_m = \frac{1}{2} Re\Big[\epsilon_3 \, \Delta\phi_{ohc_m} \times (-i\omega_m (u_{ohc}^{comp})_m)^*\Big], \tag{6.1}$$

where $*$ denotes the complex conjugate. In order to analyze the model predictions, we are interested in the power delivered to the probe tone, denoted as $(P_{som})_{probe}$, in the case of two tone suppression simulations; we are interested in the power delivered to the two primaries and to the cubic distortion component $(2f_1 - f_2)$ in the case of distortion products simulations.

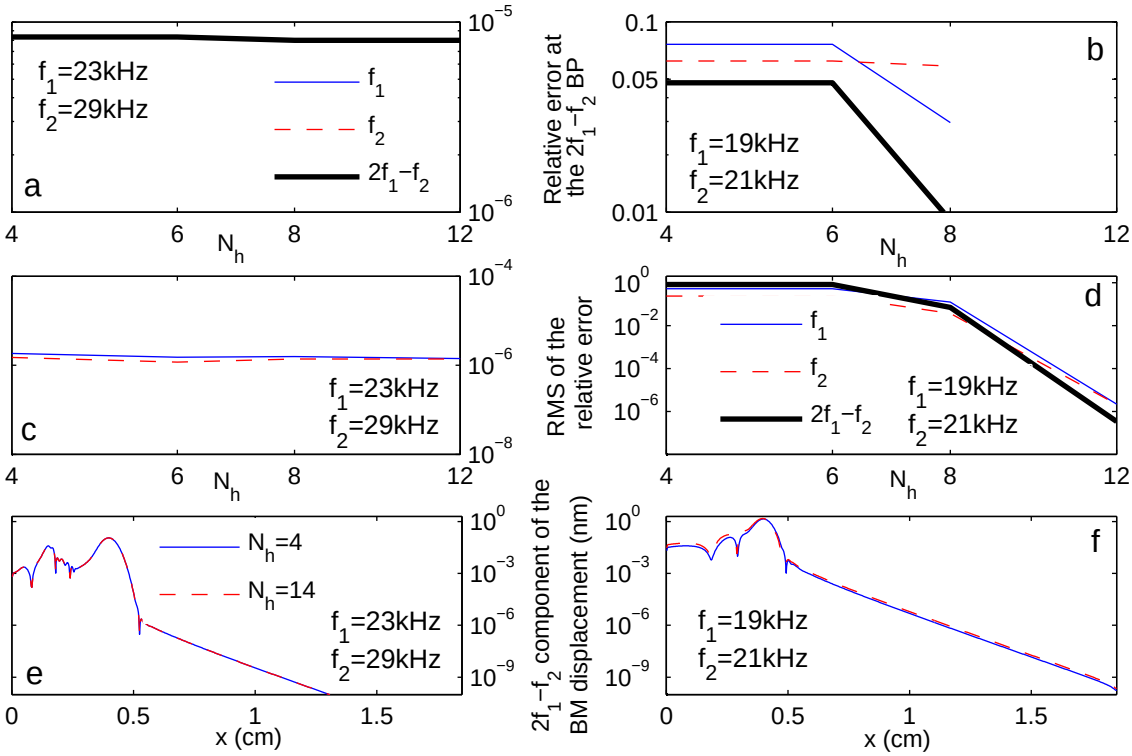

Figure 6.2: Convergence of the algorithm for two tone distortion products as a function of the number of harmonic components. In the left panels the frequencies of the primaries are $f_1 = 23$kHz and $f_2 = 29$kHz; in the right panels the frequency of the primaires are are $f_1 = 19$kHz and $f_2 = 21$kHz. The relative error in the BM displacement at the $2f_1 - f_2$ BP ($x = 0.4cm$) is plotted in a and b as function of the number of harmonic components, N_h; the root mean square (RMS) value of the relative error in the BM displacement, over the length of the cochlea, is plotted in c and d as a function of N_h. The converged solution used as a reference in the computation the error (see Appendix F) is the solution with 14 harmonic components. Thin solid line: for the f_1 component; thin dashed line: for the f_2 component; thick solid line: for the $2f_1 - f_2$ component. The $2f_1 - f_2$ components of the BM displacement is plotted as a function of x in e and f. Solid line: approximate solution (using 4 harmonic components); dashed line: converged solution (using 14 harmonic components).

6.2.4 Definition of suppression

In this chapter, the suppression in the BM diplacement, S_{bm}, and in the power delivered by somatic motility to the probe component, S_{power}, (in the case of two tone suppression) is defined as the difference in dB between the probe component of the BM diplacement (respectively in the power delivered to the probe component) when the cochlea is stimulated only with the probe tone, $u_{bm}^{probe}\Big|_{\text{no suppressor}}$ (respectively $P_{ohc}^{probe}\Big|_{\text{no suppressor}}$) and its value when the cochlea is stimulated by the probe and suppressor tones, $u_{bm}^{probe}\Big|_{\text{with suppressor}}$ (respectively $P_{ohc}^{probe}\Big|_{\text{with suppressor}}$):

$$S_{bm} = 20log_{10}\Big[\frac{\Big|u_{bm}^{probe}\Big|_{\text{no suppressor}}}{\Big|u_{bm}^{probe}\Big|_{\text{with suppressor}}}\Big] \tag{6.2}$$

$$S_{power} = 20log_{10}\Big[\frac{\Big|P_{ohc}^{probe}\Big|_{\text{no suppressor}}}{\Big|P_{ohc}^{probe}\Big|_{\text{with suppressor}}}\Big] \tag{6.3}$$

For single tone stimulation, we define self-suppression, SS, as the difference in dB between the gain of the BM relative to the stapes for a reference value of stapes displacement, u_{stapes}^{ref} to the gain of the BM relative to the stapes for the given value of stapes displacement, u_{stapes}:

$$SS(u_{stapes}) = 20log_{10}\Big[\frac{u_{bm}(u_{stapes}^{ref})}{u_{stapes}^{ref}}\Big] - 20log\Big[\frac{u_{bm}(u_{stapes})}{u_{stapes}}\Big] \tag{6.4}$$

6.3 Two tone suppression

6.3.1 Effect of a suppressor on the response to the probe tone

The predictions of the model for the displacement of the BM at the 17kHz BP with a 17kHz probe tone and a suppressor are shown in Fig. 6.3. Both for a high side suppressor (23kHz, shown in the right panels) and a low side suppressor (10kHz,

shown in the left panels), the model predicts that the presence of the suppressor reduces the magnitude of 17kHz component of the BM diplacement for low intensity of probe stimulation, in agreement with experimental data [135, 111, 19]. At higher intensity of the probe tone the effect of the suppressor becomes more limited. Therefore the suppressor reduces the nonlinearity of the response of the BM to the probe tone. The plot of Fig. 6.3(c) and (d) of the probe and suppressor components of the BM diplacement and of their sum show that the suppressor displacement at the 17kHz is a linear function of the suppressor displacement at the stapes, which is expected because of the frequency separation between the probe (17kHz) and the suppressor (23kHz and 10kHz). Consistently to the results of Fig. 6.3(a) and (b), the magnitude of probe component on the BM decreases as the intensity of the suppressor is increased. Despite the prediction of suppression both for a high side and a low side suppressor, they are some quantitative differences between the two cases. In the case of a 23kHz suppressor (Fig. 6.3(d)), the suppressor starts to suppress the probe component of the BM displacement for a suppressor component lower than the probe component; moreover there is a range of suppressor component of stapes displacement where the sum of the suppressor and probe components of the BM displacement is lower than the unsuppressed response to the probe tone. These observations are in agreement with the measurements of high side suppression from Cooper [19]. For a 10kHz suppressor (Fig. 6.3(c)), the sum of the suppressor and probe components of the BM displacement is always greater than the unsuppressed probe component, and the suppressor starts to reduce the magnitude of the probe displacement when the magnitude of the suppressor component of the BM displacement is higher than the probe component as observed experimentally [19].

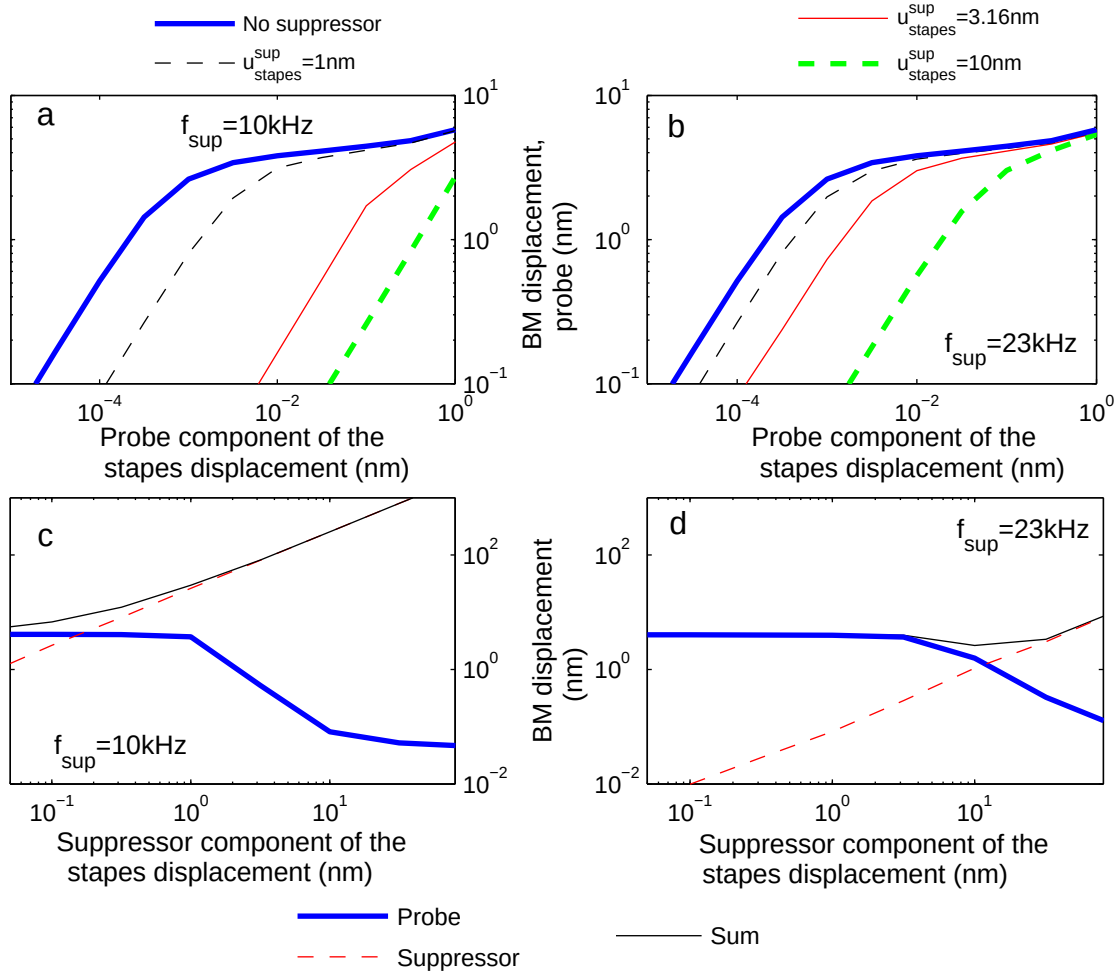

Figure 6.3: Predictions of the model for the magnitude of the BM displacement at the 17kHz BP with a probe tone of 17kHz and a suppressor. In a and c a low side suppressor of 10kHz is used. In b and d, a high side suppressor with a frequency of 23kHz is used. In a and b the probe component of the BM displacement is plotted as a function of the the probe component of the stapes displacement without a suppressor (thick solid line), with a $1nm$ (thin dashed line), $3.16nm$ (thin solid line) and $10nm$ (thick dashed line) suppressor component of the stapes displacement. In b and d, the probe component (thick solid line), the suppressor component (thin dashed line) and the sum of the two components (thin solid line) are plotted as the function of the suppressor component of the stapes displacement, for a $3.16 \times 10^{-2} nm$ probe component of the stapes displacement.

6.3.2 Effect of the suppressor on the spatial response

The mechanism of high side and low side two tone suppression can be analyzed using the spatial plots of Fig. 6.4 of the BM displacement, power delivered by somatic motility to the probe component and suppression in the BM displacement and in the power delivered by somatic motility, as a function of x. Without the suppressor, for the intensity of stimulation considered here, the probe component of the BM displacement has a peak at $x = 0.35cm$ (Fig. 6.4(a) and (b)) and somatic motility delivers energy from the base of the cochlea to a location slightly apical of the peak of the BM displacement, $x = 0.5cm$ (Fig. 6.4(c) and (d)).

The peak of the 10kHz suppressor is at $x = 0.6cm$ (Fig. 6.4(a)). In that case the effect of the suppressor is to slightly reduce the magnitude of the BM displacement at locations basal to the peak of the probe and reduce more significantly the displacement at the peak and locations slightly apical of the peak (Fig. 6.4(a)). The suppressor reduces the power delivered by somatic motility around the peak of the probe component of the BM displacement. (Fig. 6.4(c)). Moreover with the suppressor somatic motility delivers power only up to $x = 0.4cm$. The maximum of the suppression in the displacement and in the power is slightly apical ($x = 0.4cm$) of the peak of the probe (Fig. 6.4(e)).

The situation is different in the case of a 23kHz suppressor. The peak of the suppressor is at $x = 0.2cm$ (Fig. 6.4(b)). Because the transduction channels saturates when both the suppressor and the probe components of the BM displacement are high, the suppressor reduces the BM displacement (Fig. 6.4(b)) and the power delivered by somatic motility (Fig. 6.4(d)) at locations basal to the peak of the probe and apical of the peak of the suppressor, with a maximum suppression at $x = 0.25cm$ for the energy and $x = 0.3cm$ for the BM displacement (Fig. 6.4(f)). Although both high side and low side suppression are due to saturation of the transduction channel, quantitative differences in the predictions and measurements for high side and low

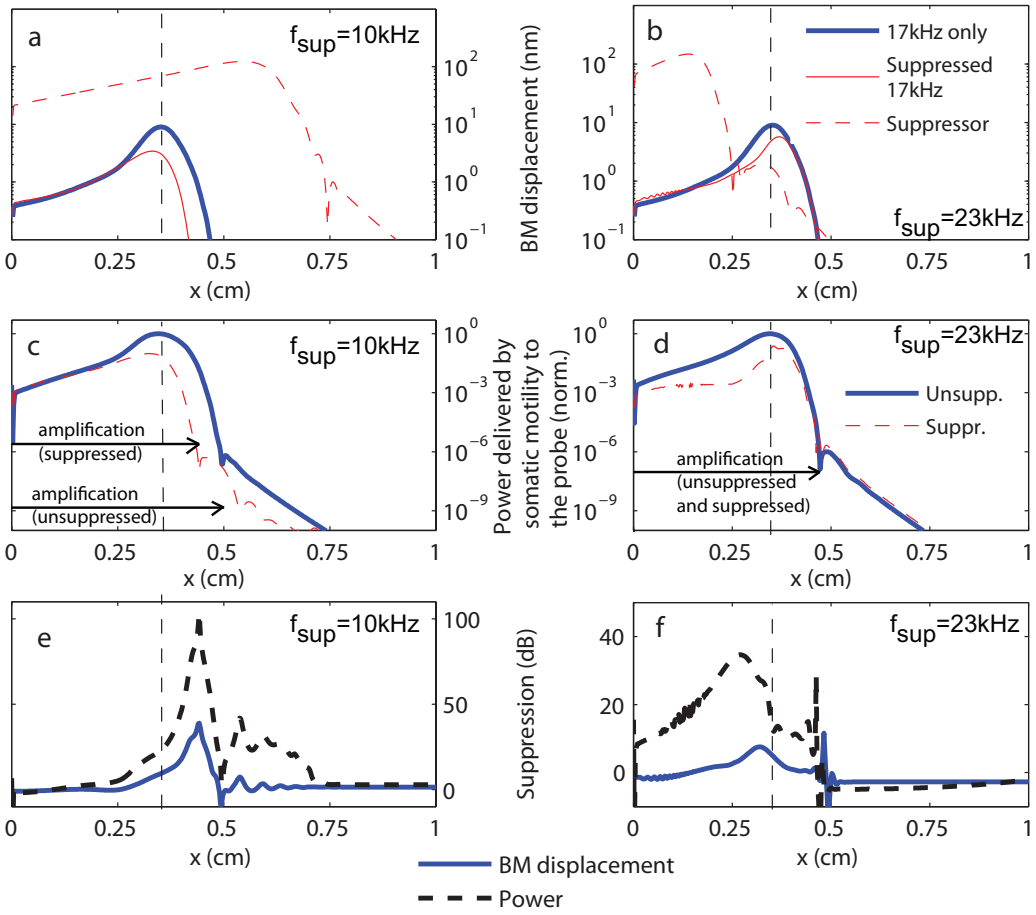

Figure 6.4: Predictions of the model for high side and low side suppression as a function of x. As previously, the probe frequency is 17kHz. In a,c and e the suppressor frequency is 10kHz (low side suppression); in b, d and f the suppressor frequency is 23kHz (high side suppression). For all plots, the probe component of the stapes displacement is $3.16 \times 10^{-2} nm$ and the suppressor component of the stapes displacement is $3.16 nm$. The vertical dashed line indicates the location of the peak of the unsuppressed probe component at this intensity of stimulation. In a and b, the unsuppressed probe component of the BM displacement (thick solid line), of the probe component in the presence of the suppressor (thin solid line) and of the suppressor component are plotted as a function of x. In c and d, the power delivered by somatic motility to the probe component of the response without the suppressor (thick solid line) and with the suppressor (thin dashed line) are plotted. The powers are normalized to the maximum power delivered when the suppressor is not present. The region of amplification, determined by looking at the sign of the power, are indicated on the figure. In e and f, the suppression in the BM displacement and in the power delivered by somatic motility are plotted.

side are to be expected due to the difference in the location of maximal suppression.

6.3.3 Effect of the suppressor on the phase of the probe tone

Two tone suppression reduces the gain of the BM response to the probe tone. A similar reduction of the gain, called self-suppression, is observed in a single tone stimulation when the intensity of the stimulation is increased (see Chapter V); self-suppression is accompanied at CF by a phase lead since a slight reduction in the phase lag of the BM relative to the stapes is seen as the BM gain relative to the stapes is reduced. If two tone suppression had the same effect on the BM displacement as self-suppression, we should expect suppression to be accompagnied by a phase lead at the BP of the probe. However, the model simulations show that this simple theory is not sufficient to predict the effect of the suppressor on the response of the BM to the probe tone. The effect of the suppressor on the phase of the probe tone relative to the stapes is analyzed in Fig. 6.5. The predictions of the phase change as a function of the suppression for a low side suppressor (represented by circles in Fig. 6.5) follow approximately the predictions for self-suppression, both in the fully active model (Fig. 6.5(a)) and in the model with reduced activity (Fig. 6.5(b)). Most of the model data for low side suppression predict a phase lead, as observed in experimental data [111, 19]. However the predictions are different for high side suppression (shown with the crosses in Fig. 6.5). For the fully active model (Fig. 6.5(a), the model predicts a phase lag for low levels of suppression (less than 20dB) and a phase lead for higher levels of suppression. When the activity of the model is reduced (by reducing the value of the somatic electromechanical coupling coefficient, ϵ_3, in Fig. 6.5(b)), the phase lag for low level of suppression is reduced (less than 0.05 cycles) and the phase lead for high level of suppression is increased (up to 0.25 cycles).

Measurements are contradictory for high side suppression [135, 111, 19], as Ruggero *et al.* [135] and Nuttall *et al.* [111] measured a phase lag, whereas Cooper[19]

measured a phase lead. The model predictions might give an explanation for this discrepancy. In the fully active cochlea high side suppression is predicted to be accompanied by phase lag at low level of suppression (for suppression of less than 20dB), as measured by Ruggero *et al.* [135] and Nuttall *et al.* [111]), and phase lead at higher intensity; note that, as discussed and predicted by Kanis and de Boer [76], that the phase data in [111] seems to transition from phase lag to phase lead when the suppression is about 20dB. In the model with reduced somatic force generation (Fig. 6.5(b)) (which could be due to damage during the recordings) the phase lag at low intensity is very small; the difference between the data in [19] and in [135, 111] might be due to some differences in the health of the cochlea during the measurements.

6.4 Distortion products

6.4.1 Generation and propagation of distortion: analysis in the spatial domain

The generation and propagation of the cubic distortion component, $2f_1 - f_2$, is analyzed in Fig. 6.6 using a spatial plot of the magnitude of the distortion and primary components of the BM displacement, of their phase relative to the stapes, and of the power delivered by somatic motility to these components of the response. The frequencies of the primaries, $f_1 = 19$kHz and $f_2 = 21$kHz, are chosen so that the frequency of the cubic distortion component, $2f_1 - f_2$ is 17kHz. The peak of the f_2 component is at $x = 0.23cm$; the peak of the f_1 component is at $x = 0.32cm$. Distortion is generated in the region where the f_1 and f_2 components overlap. Consistent with this idea, a local peak can be observed at $x = 0.3cm$ in the power delivered by somatic motility to the $2f_1 - f_2$ component; this peak corresponds to the location of maximal distortion generation.

The phase of the $2f_1 - f_2$ component has a positive slope to the left of this location;

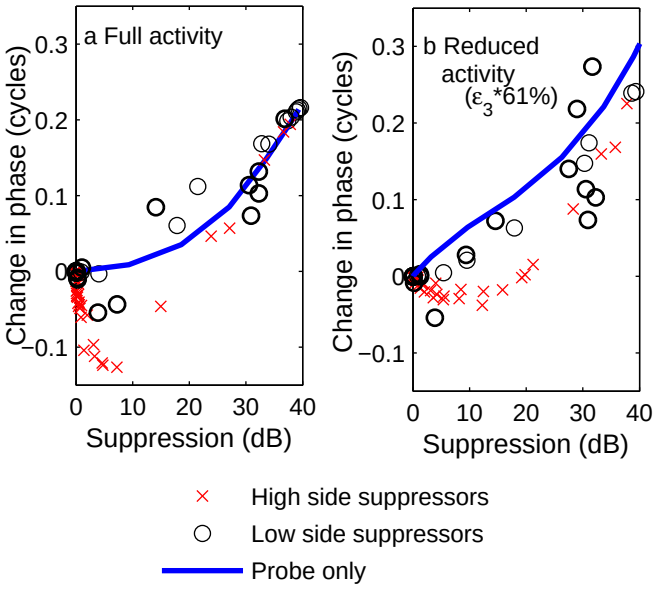

Figure 6.5: Effect of the suppressor on the phase of the probe component of the BM displacement at the probe BP. The frequency of the probe is 17kHz. The change in the phase is plotted as a function of the suppression in dB. Circles: low side suppressors. Crosses: low side suppressors. Solid line: self suppression. a. In a fully active model. b. In a model with reduced activity (the OHC electromechanical coupling coefficient ϵ_3, is reduced to 61% of its initial value. For two tone suppression, the probe component of the stapes displacement is $3.16 \times 10^{-2} nm$; the change in the phase is defined as the difference in the phase of the probe component of the BM displacement relative to the stapes with the suppressor compared to its value without the suppressor. For the case of self-suppression, the reference for the stapes displacement is $3.16 \times 10^{-2} nm$; the change in the phase is defined as the difference in the phase of the BM displacement relative to the stapes for a given probe displacement and its value for the reference stapes displacement.

this means that the distortion propagates as a slow backward propagating wave on the BM toward the stapes. The magnitude and phase of the distortion components are complicated between $x = 0.3cm$ and $x = 0cm$ because the BM displacement is the sum of the slow backward propagation of distortion, of the local distortion of the primaries (that propagates in the forward direction), of the reflection of the slow backward wave on the stapes (this reflection propagates as a slow forward traveling wave) and possibly of the reflection of a fast compressional backward wave (that also propagates on the BM as a slow forward traveling wave).

The phase of the $2f_1 - f_2$ component has a negative slope to the right of $x = 0.3cm$; this means that the distortion propagates in the forward direction. As the traveling wave of the distortion component propagates in the forward direction it approaches the 17kHz BP (which is apical of the location of the location of maximal distortion generation). The distortion component is amplified close its BP as the power delivered by somatic motility is maximum. Therefore the $2f_1 - f_2$ component reaches a maximum magnitude close to the 17kHz BP ($0.4cm$), at $x = 0.395cm$ for this intensity of stimulation.

6.4.2 Spectrum of the BM response to two tones

The frequency spectrum of the BM displacement predicted by the model for primary tones of 19kHz and 21kHz is shown in Fig. 6.7. At the location of maximum distortion products generation (results shown in the left panels) the primary components have the highest magnitudes. Odd order distortion products (cubic distortion, $2f_1 - f_2 = 17$kHz and $2f_2 - f_1 = 23$kHz, and 5th order distortion at 15kHz and 25kHz) are generated. Even order distortion products are also present but have a much lower magnitude. Note the constrast with the results of Fig. 5.6 for single tone stimulation in Chapter V; the 2nd order distortion has the highest magnitude in single tone stimulation while the cubic distortion components have the highest

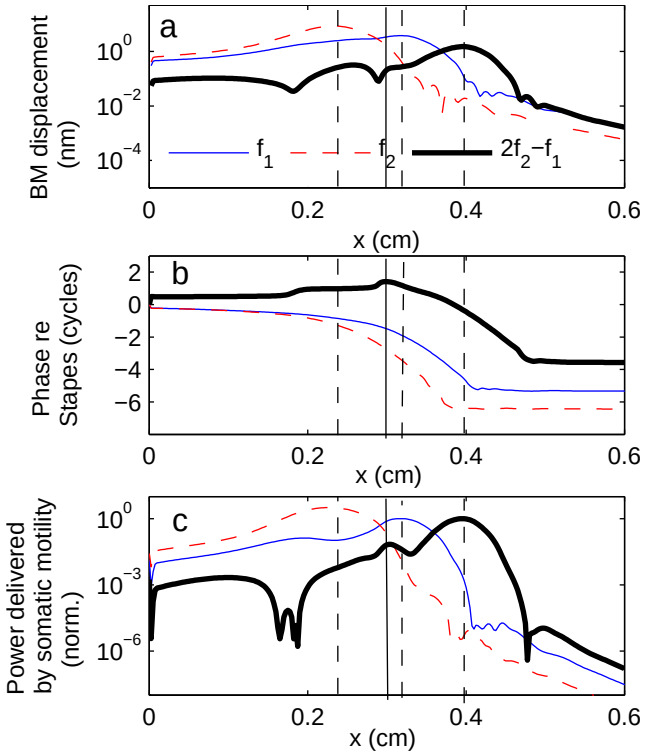

Figure 6.6: Spatial plot of the primaries and cubic distortion product $2f_1 - f_2$. The frequencies of the primaries are $f_1 = 19$kHz and $f_2 = 21$kHz, the cubic distortion product frequency $2f_1 - f_2$ is 17kHz. The two primary components of the stapes displacement are both $3.16 \times 10^{-9} nm$. Thin solid line: f_1 component; thin dashed line: f_2 component; thick solid line: $2f_1 - f_2$ component. a. Magnitude of the BM displacement as a function of x. b. Phase of the BM displacement relative to the stapes. c. Power delivered by somatic motility to the different components of the response. The location of the peak displacement of the f_1, f_2 and $2f_1 - f_2$ components are indicated by vertical dashed line. The location of the maximum $2f_1 - f_2$ generation (which corresponds to a local maximum in the power)is indicated by a solid vertical line.

magnitude in two-tone stimulation. The components of highest order have a lower magnitude. At the $2f_1 - f_2$ best place (shown in the right panels), frequencies close to 17kHz are amplified by the cochlear amplifier while the other components are filtered out. Therefore at low intensity the $2f_1 - f_2$ cubic distortion component has a higher magnitude than the primary components and then 5^{th} order 15kHz component has a higher magnitude than the 3^{rd} order 23kHz component.

6.4.3 Dependence of DP on the level of the primaries

The predictions of the cubic distortion component, $2f_1 - f_2$, depends on the magnitude of the primary components of the stapes displacement, as shown in Fig. 6.8. If the value of the two primary components are kept the same, as in Fig. 6.8(a), the DP component of the BM displacement is predicted to grow at a fast rate with respect of the stapes displacement (2.8dB/dB) for very low magnitude of stapes displacement (less than 5×10^{-4}nm) then grows with a slower rate, until a maximum is reached for primary components of stapes displacement of magnitude $10^{-2}nm$ to $1nm$, depending on the value of the ratio f_2/f_1. The predictions are in good agreement with the data from Robles *et al.* [131, 132] who observed (in the chinchilla) a monotonic growth of the cubic distortion product from about 30dB SPL to 70dB SPL, with a rate of 1.3dB/dB at relatively low intensity of stimulation (about 30dB SPL), and a decrease for higher level of stimulation. In Fig. 6.8(b) the magnitude of the f_2 component of the stapes displacement is kept constant and the magnitude of the f_1 component is varied. The model predictions are in very good agreement with experimental data [26, 132]. The distortion product grows at low intensity of the f_1 component with the same rate as in the measurements (2dB/dB), then reaches a maximum (that depends on the value of the f_2 displacement), and decreases at higher intensity of the f_1 component. The magnitude of the $2f_1 - f_2$ component is plotted as a function of the f_2 component of the stapes displacement for a fixed f_2 component at the stapes in Fig.

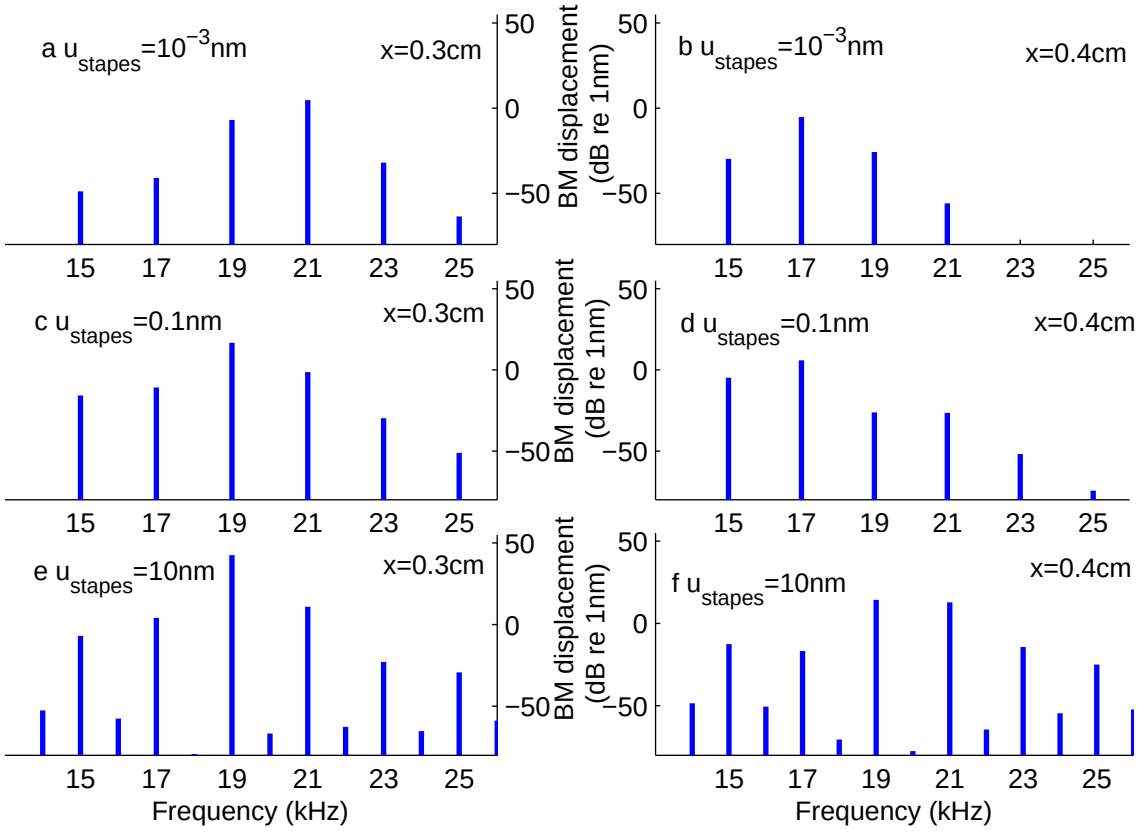

Figure 6.7: Predictions of the frequency spectrum when the cochlea is stimulated by two tones of frequencies $f_1 = 19$kHz and $f_2 = 21$kHz. Left panels: at the location of maximum distortion products generation (x=0.3cm). Right panels: at the $2f_1 - f_2$ BP (x=0.4cm). The magnitude of the two primary components of the stapes displacement are the same, and is increased from $10^{-3}nm$ (a and b) to $10nm$ (e and f). The magnitudes of the different components of the BM displacement, in dB relative to 1nm, are plotted for the different harmonic component; the frequency of the components is indicated on the horizontal axis.

6.8. In that case the distortion product is a linear function of the f_1 component at low intensity of stimulation, as the rate of growth is 1dB/dB, as in the experimental data [132]. The distortion product reaches a maximum and then decreases at higher intensity of stimulation.

6.4.4 Dependence of the $2f_1 - f_2$ distortion component on the ratio of the frequencies of the primaries

The generation and the amplification of distortion products, and particularly of the cubic distortion component $2f_1 - f_2$, depend on the ratio of the frequencies of the primaries, f_2/f_1, a shown in Fig. 6.9. For low or moderate intensity of the primary components of the stapes displacement (10^{-4}nm or 10^{-2}nm), the model predicts that the cubic distortion is maximum for a ratio of 1.15 to 1.2, which is similar to the experimental data in [132]. For larger stapes displacement, the magnitude of the $2f_1 - f_2$ is also a nonmonotonic function of the frequency ratio but the model predictions are significantly different from the experimental data, with a maximum magnitude predicted to be for high values of the frequency ratio.

6.5 Discussions

6.5.1 The model predicts a realistic response of the cochlea to two tones

The predictions of nonlinear two tone interactions is a good test of the model as there is extensive published experimental data. By introducing a nonlinearity in the mechanoelectrical transduction channel the model predicts two tone suppression and two tone distortion products in good agreement with the measurements. These predictions are a further validation of the theory that somatic motility is the cochlear amplifier and that the nonlinearity of the cochlea arises from the nonlinearity of the transduction channels. Both in the model predictions and in the experimental

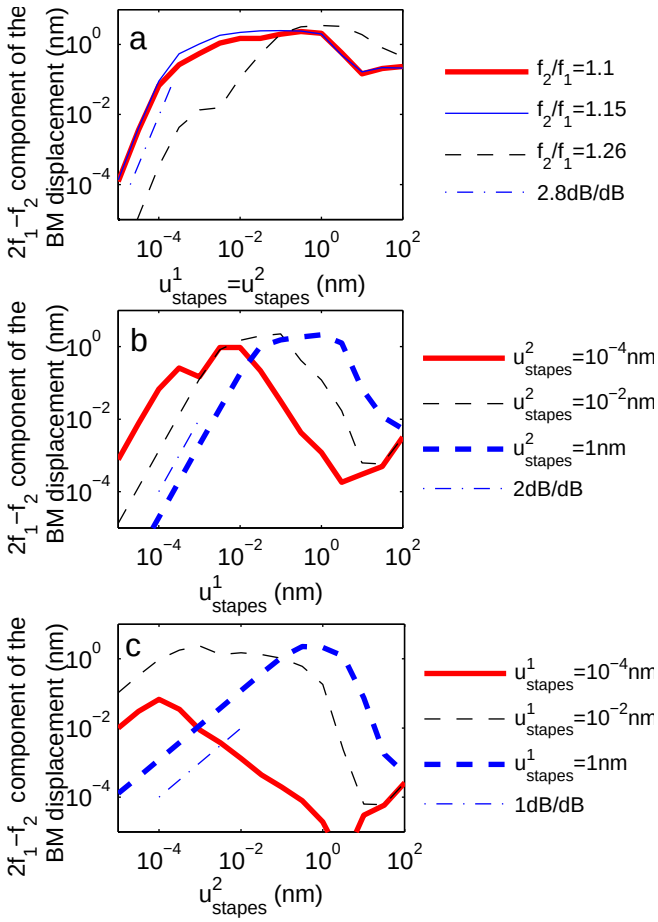

Figure 6.8: Dependence of the $2f_1 - f_2$ component on the magnitude of the primary components of the stapes displacement at the $2f_1 - f_2$ BP. The magnitude of the $2f_1 - f_2$ component of the BM displacement is plotted as function of the stapes displacement a. The magnitude of the two primary components at the stapes are the same. The horizontal axis is the magnitude of each of the primary components of the stapes displacement. Thick solid line: $f_2/f_1 = 1.1$; thin solid line: $f_2/f_1 = 1.15$; thin dashed line: $f_2/f_1 = 1.26$. b. The magnitude of the f_2 component of the stapes displacement is fixed, to $10^{-4}nm$ (thick solid line), $10^{-2}nm$ (thin dashed line) and $1nm$ (thick dashed line). The ratio f_2/f_1 is 1.1. The horizontal axis is the f_1 component of the stapes displacement. c. The magnitude of the f_1 component of the stapes displacement is fixed to $10^{-4}nm$ (thick solid line), $10^{-2}nm$ (thin dashed line) and $1nm$ (thick dashed line). The ratio f_2/f_1 is 1.1. The horizontal axis is the f_2 component of the stapes displacement.

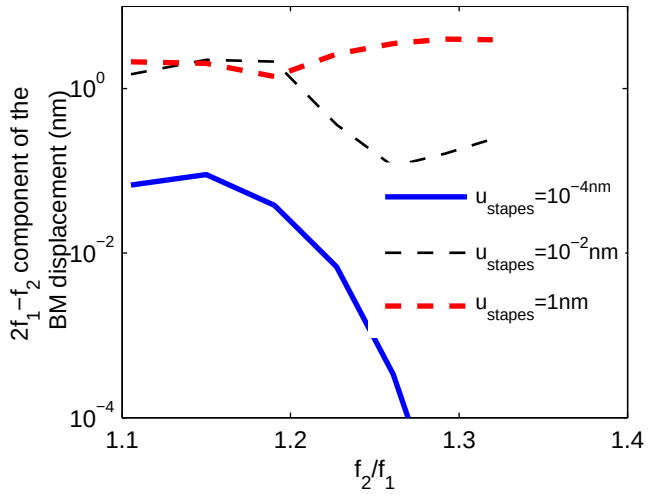

Figure 6.9: Effect of the frequency ratio f_2/f_1 on the prediction of the cubic distortion term, $2f_1 - f_2$. The magnitude of the $2f_1 - f_2$ component of the BM displacement is plotted as a function of the ratio f_2/f_1 at the $2f_1 - f_2$ BP for f_1 and f_2 components of the stapes displacement of the same magnitude. Thick solid line: for a $10^{-4}nm$ stapes displacement. Thin dashed line: for a $10^{-2}nm$ stapes displacement. Thick dashed line: for a $1nm$ stapes displacement.

data, the magnitude of the cubic distortion product is a nonlinear function of the level of the primaries and of the frequency ratios; three mechanisms contribute to the complex nature of distortion products: the generation of distortion products (due to the nonlinearity of the transduction channels in the region where the two primaries overlap), the amplification of the distortion product close to its BP and the suppression of the primaries and of the distortion products. The nice predictions of the characteristics of distortion products suggest that the model captures well the dynamics of the cochlea (including the vibrations of the organ of Corti) at high frequencies.

6.5.2 Deficiencies of the model for low side suppression

Despite some realistic predictions about two tone suppression and a good capture of the quantitative differences between high side and low side suppression there are some deficiencies in the results for a low side suppressor. If the frequency of the

suppressor is less than about 5kHz, the displacement required to suppress the BM displacement is much higher than in experimental data. Moreover phasic suppression (modulation of the response to the probe component by a low frequency suppressor) is not as pronounced in the model predictions (results not shown) as in experimental data [19, 51]. These deficiencies of the model could be due to an incorrect prediction of the HB deflection (which induces an inaccurate prediction of the transduction current) at low frequencies for basal locations, since the effect of a low frequency suppressor on a high frequency probe depends on the prediction of the transduction current at low frequencies. At low frequency compared to the CF, the transduction current does not influence the prediction of the fundamental of the BM displacement; therefore a wrong value of the HB deflection at low frequency does not affect the low frequency response of the cochlea (of the fundamental) to a single tone at basal locations.

6.5.3 Propagation of distortion products in the cochlea

The way distortion products propagate from its location of generation to the stapes to emit DPOAEs is controversial as two alternative theories coexist. One theory, supported notably by measurements of the DPOAEs delay [98], is that a slow backward traveling wave propagates on the BM toward the stapes; the other, supported by measurements of the phase of the BM motion at different longitudinal locations [64] or at different frequencies on the BM [36], is that a fast compressional wave travels in the cochlear fluids (at the speed of sound). In the second theory a slow forward propagating wave is seen on the BM as the fast wave is reflected on the stapes and round window. The model results are in agreement with the first theory. Some further investigation of the directions of wave propagation using different boundary conditions at the stapes is needed. In the current formulation the stapes are forced to vibrate with a prescribed displacement; a more realistic model for acoustic stimulation

would be to apply a force or to couple the stapes to a middle ear model. Another reason of the difference between the model predictions and the measurements of the phase of the distortion product on the BM could be due to coupling of the fluid to the TM that could induce a nonsymmetry in the intracochlear fluid pressure field; in the current model the fluid is not directly coupled to the TM.

CHAPTER VII

Conclusions and future work

7.1 Conclusions

In this thesis a mathematical model of the cochlea has been used to simulate the response of the mammalian cochlea to acoustic stimulation so as to analyze and improve our understanding of cochlear mechanics. The model is based on the physiology of the cochlea and includes the acoustic, mechanical and electrical domains and active feedback from somatic motility. The analyses were focused on the response at basal locations. The parameters of the model are based on measured properties of the mammalian cochlea, and more specifically of the guinea pig cochlea when the data is available. Significant insight has been gained regarding the role of structural longitudinal coupling, the identity of the cochlear amplifier, the role of fast adaptation in cochlear amplification and the nonlinear response of the cochlea using this theoretical approach.

To analyze the role of structural longitudinal coupling, models for the BM and the TM, based on experimental data, were implemented in a linear version of the macroscopic model of the cochlea. Structural longitudinal coupling was found to be critical for normal hearing as it controls the sharpness of tuning, the sensitivity of the BM and the speed of transient capture of the BM response to acoustic stimuli. Although the classical theory of cochlear mechanics is based on a locally reacting

representation of the cochlear partition, the locally reacting version of the cochlear model results in a BM response much sharper than experimental data; therefore longitudinal coupling is necessary for more realistic predictions. In the formulation used in this thesis, introducing longitudinal coupling in the BM and TM mechanics does not increase the computational cost. The viscoelasticity of the TM is particularly important to broaden the response of the BM as it can couple a large number of OHCs. Several research groups have recently tried to measure the material properties of the TM [58, 55, 129, 47]. These measurements have been essential to implement a realistic model of the TM in this thesis. The TM plays an important role in this model of the cochlea, as the resonance of the TM shear mass enhance the transduction current close to the CF; moreover the IHC are deflected by the fluid motion due to the relative shear motion betwen the TM and RL. Unfortunately, measurements of the response of the cochlea to acoustic stimulation have been focused on the BM and not on the TM, due to historical reasons and to the difficulty in accessing the TM. Because of the critical role of the TM in cochlear amplification and IHC stimulation, measurements of the TM response (as well of the organ of Corti vibrations) to acoustic stimulation seem necessary to improve our understanding of the cochlea. These measurements would give important information to validate and improve this cochlear model.

The highly debated issue of the identity of the cochlear amplifier was addressed in this thesis. The theoretical approach used here, with the linearized version of an active HB model implemented in the linear macroscopic model of the cochlea, gives some good insight regarding the role of the two active processes (active HB dynamics and prestin based somatic motility) in mammalian cochlear mechanics. In the theory of mammalian cochlear amplification developed here, somatic motility is the cochlear amplifier as the active HB does not deliver enough energy to modulate the BM vibrations. However, fast adaptation of the transduction current, due to the active HB dynamics, controls the sensitivity of the transduction channel to HB

deflection, and thereby stabilize the cochlea by reducing the energy delivered by somatic motility. The RC filtering of the OHC transmembrane potential does not preclude somatic motility from acting as the cochlear amplifier, mostly because of the high value of the HB conductance as well as of a resonance in the organ of Corti. The values used as a parameter for the HB conductance, and predicted for the OHC transmembrane potential, are somewhat higher (but within a reasonable range) than the best experimental estimates [63, 85]. Efforts to measure these quantities in a sensitive *in vivo* setup would give data to test the theory. The model predicts that somatic motility is necessary to assure a sensitive and tuned BM response to acoustic stimulation, which is consistent with experimental manipulations of prestin activity [141, 32].

Finally, the nonlinear mechanics of the cochlea have been predicted using a nonlinear version of the model of the cochlea. An iterative frequency domain approach (alternating frequency/time method [13]) was used to limit the computational cost. Due to the weak nonlinearity of the cochlea and to the low number of nonlinear equations governing its dynamics, this method is particularly efficient. Introducing a physiologically relevant nonlinearity in the transduction channel results in realistic predictions of the compressive nonlinearity and harmonic distortion in response to a single tone and of two tone suppression and distortion products on the BM in response to two tones. Nonlinear predictions are a good test of the model because of the extensive amount of experimental data to compare the predictions to. The parameters have been slightly modified to better match the measurements of the nonlinear response of the cochlea. There are still some quantitative differences between experimental data and the model predictions, most significantly for the threshold of nonlinearity in single tone stimulation and the characteristics of low side suppression. This could be do to some deficiencies in the micromechanical model, possibly in the prediction of the HB deflection as a function of frequency. But overall the model predictions are

consistent with the theory that somatic motility is the cochlear amplifier and that the nonlinearity of the cochlea is due to the nonlinearity of the MET channels.

A computational model such as this one relies on experimental measurements. One

7.2 Future work and unresolved issues

Significant progress in the understanding of mammalian cochlear mechanics has been gained using the analyses presented in this thesis. However, the model of the cochlea could be extended and improved.

The effect of the fast adaptation mechanism on the nonlinear mechanics of the cochlea still needs to be investigated since it has been ignored in the nonlinear cochlear model. Using the linear analysis, the active HB force has been shown to be too small to significantly modulate the BM response to acoustic stimulation. However, the reduction in the MET sensitivity due to fast adaptation plays an important role in the sensitivity of the cochlea to low intensity stimulation. The effect of fast adaptation of mechanotransduction is nonlinear, as no adaptation is seen for very large HB deflection. Implementation of a nonlinear version of the active HB dynamics in the nonlinear model of the cochlea is still needed to further validate and refine the theory established in this thesis about the role of the active HB dynamics in cochlear mechanics.

Another part of the model that could be improved concerns the micromechanics of the organ of Corti. The lack of current experimental data about the dynamics of the organ of Corti makes it difficult to validate the micromechanical model. Some ongoing research in Freeman's group [65] and Nuttall's group [18] focus on the *in vivo* imaging and measurements of the vibrations of the organ of Corti during acoustic stimulation. These measurements could be used to improve the micromechanical model. Some potential improvements include introducing longitudinal coupling in

the RL, the modeling of the phalangeal process, and including a mass for the RL, OHC and Deiter's cells. The micromechanical model could also be extended to model the fluid in the subtectorial space and the fluid forcing on the IHCs.

The model predictions at apical locations are not very realistic and still require some effort. One of the important question at the apex is the role of HB motility and somatic motility at these locations. There are some qualitative differences between the mechanics of the cochlea at basal and apical locations according to experimental measurements of the mechanical vibrations at apical locations [24, 22, 82, 83], which could be due to a more prominent role of HB motility at the apex of the cochlea. The improvement of the model at apical locations and the investigation of the role of the two active processes at low frequency are still needed.

Finally, the predictions of distortion products on the BM could be pursued to analyze in details their propagation on the BM and the generation of DPOAEs. Reverse wave propagation of DPOAEs on the BM is a controversial topic in cochlear mechanics due to the different conclusions based on the measurements of the characteristics of DPOAEs [98] and of the phase of distortion products on the BM [64, 36]. A better understanding of the way distortion products leave the cochlea (as a slow backward propagating wave on the BM or as fast compressional fluid in the fluid) is needed for a better use of DPOAEs as a noninvasive diagnostic tool of abnormal hearing. The influence of different boundary conditions and of fluid forcing on the BM on the predition of wave propagation and the coupling of the cochlear model to a middle ear model could be studied. If the model can successfully replicate experimental data of distortion products generation and propagation on the BM and DPOAEs emission, the predictions of the spectrum and delays of DPOAEs could be then used to test different hypothesis of abnormal emissions in relationships with the mechanics of the cochlea.

APPENDICES

APPENDIX A

Estimation of the TM stiffness per unit length, K_{tms}.

Richter et al.[129] measured the TM radial stiffness in the gerbil hemicochlea using a piezolectric probe of diameter $d = 25\mu m$. For static measurements, the governing equation Eq. 2.2 for the TM radial displacement of the TM is given by (neglecting the variations of A_{tm}^{eff} and G_{xy} as a function of x):

$$f_{ext}(x) = K_{tms}u_{tms} - A_{tm}^{eff}G_{xy}\frac{\partial^2 u_{tms}}{\partial x^2}, \tag{A.1}$$

where f_{ext} is the force per unit length applied by the probe. The probe deforms the TM with the following mode shape:

$$\begin{aligned} u_{tms}(x) &= U \text{ if } |x - x_0| < \frac{d}{2} \\ u_{tms}(x) &= Ue^{-\frac{|x-x_0|}{\lambda}} \text{ if } |x - x_0| > \frac{d}{2} \end{aligned} \tag{A.2}$$

where x_0 is the center of application of the probe force, U is the displacement of the TM at the probe tip and $\lambda_{tm} = \sqrt{\frac{A_{tm}^{eff}G_{xy}}{K_{tms}}}$. Therefore the stiffness measured by the

probe is:

$$K = \frac{\int_{(x_0-d/2)^-}^{(x_0+d/2)^+} f_{ext}(x)dx}{U} = K_{tms}d\Big(1 + 2\frac{\lambda_{tm}}{d}\Big) \tag{A.3}$$

With the parameters used in our simulations, at $x = 0.4cm$ (which corresponds to the 17kHz BP in the guinea pig), $K_{tms} = 4.2kPa$, $G_{xy} = 2.1kPa$, $A_{tm}^{eff} = 3120\mu m^2$, so that $\lambda_{tm} = 40\mu m$ and $K = 4.2 \times K_{tms}d = 0.44N/m$. In the gerbil cochlea, at the 17kHz BP, Richter et al. measured $K = 0.255N/m$ (when the TM is detached from the stereocilia).

APPENDIX B

Parameters of the macroscopic model of the cochlea.

Table B.1: Basilar membrane properties (x is in m)

Properties	Value in Chapters III and IV	Value in Chapters V and VI	Ref
$D_{xx}(N.m)$	0 in LR and TM-LC 6.5×10^{-11} in BM-LC and TMBM-LC	4×10^{-11}	[89]
$D_{xy}(N.m)$	0 in LR and TM-LC 3.1×10^{-11} in BM-LC and TMBM-LC	10×10^{-11}	[89]
$D_s(N.m)$	0 in LR and TM-LC 4.3×10^{-11} in BM-LC and TMBM-LC	4.3×10^{-11}	[89]
$D_{yy}(N.m)$	$1.9 \times 10^{-9}(\frac{h_{bm}}{7\times10^{-6}})^3$	$1.8 \times 10^{-9}(\frac{h_{bm}}{7\times10^{-6}})^3$	[60, 121]
M_{bm}	$\rho_{bm}h_{bm}$ where $\rho_{bm} = 1000kg/m^3$	$\rho_{bm}h_{bm}$ where $\rho_{bm} = 1000kg/m^3$	[121]
$C_{bm}(N.s/m^2)$	$A_{21}^2 0.01\frac{L_{tm}}{L_{st}} + 0.85 \times 10^{-1}$	$A_{21}^2 0.01\frac{L_{tm}}{L_{st}} + 0.5 \times 10^{-1}$	
b (m)	$(80 + 54 \times 10^{-2}x) \times 10^{-6}$	$(80 + 54 \times 10^{-2}x) \times 10^{-6}$	
h (m)	$(7 - 2.86 \times 10^{-2}x) \times 10^{-6}$	$(7 - 2.86 \times 10^{-2}x) \times 10^{-6}$	

Table B.2: Tectorial membrane properties (x is in m)

Properties	Value in Chapters III and IV	Value in Chapters V and VI	Reference
A_{tm}^{eff}	$A_{tm}^0 e^{50x} kg/m$ $A_{tm}^0 = 2600\mu m^2$	$A_{tm}^0 e^{50x} kg/m$ $A_{tm}^0 = 2600\mu m^2$	based on[129]
K_{tms}	$1.4 \times 10^4 e^{-\alpha_{tm}x} N/m^2$ with $\alpha_{tm} = 300m^{-1}$	$0.42 \times 10^4 e^{-\alpha_{tm}x} N/m^2$ with $\alpha_{tm} = 300m^{-1}$	based on [129], see Appendix B
M_{tms}	$0.9\rho_{tm}A_{tm}^{eff}$ $\rho_{tm} = 1200kg/m^3$	$0.9\rho_{tm}A_{tm}^{eff}$	
G_{xy}	$7.0e^{-\alpha_{tm}x} kPa$	$8.0e^{-\alpha_{tm}x} kPa$	[47]
η_{xy}	$0.05Pa.s$	$0.02Pa.s$	0.20 Pa.s in the mouse TM [55]
$C_{tms}(N.s/m^2)$	$0.01 \times \frac{L_{tm}}{L_{st}}$	$0.01 \times \frac{L_{tm}}{L_{st}}$	
K_{tmb}	$1.4 \times 10^4 e^{-\alpha_{tm}x} N/m^2$ with $\alpha_{tm} = 300m^{-1}$	$0.42 \times 10^4 e^{-\alpha_{tm}x} N/m^2$ with $\alpha_{tm} = 300m^{-1}$	based on [129], see Appendix B
M_{tmb}	$0.77\rho_{tm}A_{tm}^{eff}$	$0.77\rho_{tm}A_{tm}^{eff}$	
$C_{tmb}(N.s/m^2)$	0.5×10^{-1}	1.0×10^{-1}	

Table B.3: Organ of Corti properties (x is in m)

Properties	Value in Chapters III and IV	Value in Chapters V and VI	Reference
$K_{hb}(N/m^2)$	$5.8 \times 10^4 exp(-0.033x)$	$5.2 \times 10^4 exp(-0.033x)$	[151]
$K_{ohc}(N/m^2)$	$6.0 \times 10^3 exp(-0.0315x)$	$6.3 \times 10^3 exp(-0.0315x)$	
$K_{rl}(N/m^2)$	$6.0 \times 10^3 exp(-0.0315x)$	$6.3 \times 10^3 exp(-0.03.15x)$	

Table B.4: Geometrical parameters (x in m)

Properties	Value	Reference
L_{Ro}	$40\mu m$	[107]
L_{pc}	$\frac{b}{3}$	[107]
L_1	$13\mu m$	[107]
L_0	$0.5b$	[107]
L_t	$\frac{L_{tm}}{3}$	[107]
α	25degrees to 45 degrees (apex)	[147]
β	$= \alpha$	assumed
θ_1	60 degrees	[107, 30]
θ_2	60 degrees	[107, 30]
L_{ohc}	$20\mu m$ (base) - $6\mu m$ (apex)	[147]
L_{hb}	$1\mu m$ (base) -$6\mu m$ (apex)	[29]
Duct height for SV,ST	0.1cm	[42]
Duct Width (W)	0.1cm	[42]
Duct length (L)	1.85cm	[42]

Table B.5: Somatic motility and mechanotransduction parameters (x in m)

Prop.	Value in Chapter III	Value in Chapter IV	Value in Chapters V and VI	Ref.
ϵ_3 (N/m/mV)	$\epsilon_3^0 \times (1 + 10x)$ where $\epsilon_3^0 =$ -1.04×10^{-5} (TMLC) -0.784×10^{-5} (BMLC) -1.12×10^{-5} (TMBMLC) -0.616×10^{-5} (LR)	$\epsilon_3^0 \times (1 + 10x)$ where $\epsilon_3^0 =$ 1.04×10^{-5}	$\epsilon_3^0 \times (1 + 10x)$ where $\epsilon_3^0 =$ -1.04×10^{-5}	[72]
f_{gs} (pN)	5	5	10	[8]
γ	$\frac{0.5\times10^{-6}m}{L_{hb}}$	$\frac{0.5\times10^{-6}m}{L_{hb}}$	$\frac{0.5\times10^{-6}m}{L_{hb}}$	[103]
G_a^{max} (nS)	$462exp(-\alpha_G x)$ $\alpha_G = 0.0215m^{-1}$	$795exp(-\alpha_G x)$ $\alpha_G = 0.0225m^{-1}$	$357.5exp(-\alpha_G x)$ $\alpha_G = 0.0225m^{-1}$	[63]

Table B.6: Electrical parameters (x in m)

Properties	Value	Reference
G_a^0	100μS/m	[31]
$1/R_m$	5100μS/m (base) - 360 μS/m (apex)	[66]
C_a	50nF/m	[31]
C_m	1800nF/m (base) - 4200nF/m (apex)	[66]
$V_{sm} - V_{ohc}$	(150-1000x)mV	[149]
R_{vl}	10Ωm	[149]
R_{tl}	4Ωm	[149]
R_{vm}	25Ωm	[149]
r_{sv}	3MΩ/m	[149]
r_{sm}	5MΩ/m	[149]
r_{st}	150MΩ/m	[149]

APPENDIX C

Equations governing the nonlinear six state transduction channel model.

The equations governing the six state model of the HB dynamics (Fig. 5) are described next.

When the channel is open, the binding and unbinding rates are denoted as k_2 and $r_2 k_2$, where

$$k_2 = K_B^o C_{fa}^o \tag{C.1}$$

$$r_2 = \frac{K_D^o}{C_{fa}^o} \tag{C.2}$$

When the channel is closed, the binding and unbinding rate are denoted as $r_4 k_4$ and k_4 where

$$k_4 = K_B^c K_D^c \tag{C.3}$$

$$r_4 = \frac{C_{fa}^c}{K_D^c} \tag{C.4}$$

Note that k_2 and k_4 are assumed to be independent, which means that K_B^o and K_B^c have different values.

When no calcium ion is bound to the channel (states 1 and 2), the rate of channel opening k^0_{co}, and closing, k^0_{oc}, are given by:

$$k^0_{co} = k_1 \exp(\frac{f_{gs}x}{2k_BT}) \tag{C.5}$$

$$k^0_{oc} = r_1 k_1 \exp(-\frac{f_{gs}x}{2k_BT}) \tag{C.6}$$

where x is the displacement of the HB in the tip link direction, k_1 is a constant and r_1 is given by:

$$r_1 = \exp\left(\frac{-\Delta E_0}{k_BT}\right) \tag{C.7}$$

where ΔE_0 is a constant energy. The reaction coordinate of gating in the closed to open transitions [17], is assumed to be 0.5 for simplicity. When 1 or 2 calcium ions are bound to the channel ($n_{Ca} = 1$ or 2), the rates of channel opening, $k^{n_{ca}}_{co}$ and closing, $k^{n_{Ca}}_{oc}$ (where $n_{Ca} = 1, 2$) are given by:

$$k^{n_{Ca}}_{oc} = k_{2n_{Ca}+1} \exp(\frac{f_{gs}x}{2k_BT}) \tag{C.8}$$

$$k^{n_{Ca}}_{co} = r_{2n_{Ca}+1} k_{2n_{Ca}+1} \exp(-\frac{f_{gs}x}{2k_BT}) \tag{C.9}$$

where r_3 and r_5 are given by:

$$r_{2n_{Ca}+1} = \exp\left(\frac{\Delta E_0 - n_{Ca}\epsilon_{Ca}}{k_BT}\right), \text{where } n_{Ca} = 1, 2 \tag{C.10}$$

and k_3 and k_5 are given by:

$$k_{2n_{Ca}+1} = k_1 r_1 exp(\frac{n_{Ca}\epsilon_{Ca}}{2k_BT}), \text{where } n_{Ca} = 1, 2 \tag{C.11}$$

APPENDIX D

Computation of the effect of calcium on the model predictions.

The derivation of the equations governing the response of the HB for small pertubations in the external calcium concentration C^o_{fa} (Fig. 4) are described next. The vector of the probabilities, $\mathbf{P}$, is governed by the following equations at equilibrium:

$$\mathbf{A}(\frac{f_{gs}(x-x_a)}{2k_BT}, C^o_{fa})\mathbf{P} = \mathbf{0} \tag{D.1}$$

where the matrix $\mathbf{A}$ is a function of $\frac{f_{gs}(x-x_a)}{2k_BT}$ and of the extracellular calcium concentration C^o_{fa}. Only the rate k_2 and the ratio r_2 depends on C^o_{fa}. If $\mathbf{P^s}$ denotes the vector of resting probabilities with the resting calcium concentration and the position of the HB, x^s, and of the slow adaptation motor, x^s_a are $x^s = x^s_a = 0$ the change in the equilibrium probabilities of the channel for small pertubations in the calcium concentration is governed by the following equation:

$$0 = \mathbf{A}\frac{\partial \mathbf{P}}{\partial C^o_{fa}}\delta C^o_{fa} + \Big[\frac{\partial(x-x_a)}{\partial C^o_{fa}}\frac{f_{gs}}{2k_BT}\frac{\partial \mathbf{A}}{\partial(x-x_a)} + \frac{\partial \mathbf{A}}{\partial C^o_{fa}}\Big]\mathbf{P}^s\delta C^o_{fa} \tag{D.2}$$

so that the pertubations in the resting probabilities are:

$$\frac{\partial \mathbf{P}}{\partial C_{fa}^o}\delta C_{fa}^o = -\mathbf{A}^{-1}\Big[\frac{\partial(x-x_a)}{\partial C_{fa}^o}\frac{f_{gs}}{2k_BT}\frac{\partial \mathbf{A}}{\partial(x-x_a)} + \frac{\partial \mathbf{A}}{\partial C_{fa}^o}\Big]\mathbf{P}^s\delta C_{fa}^o \tag{D.3}$$

The slow adaptation motor force, f_{mot}, is assumed to be independent of the calcium concentration. At equilibrium, the equation governing the slow adaptation motor [153] is:

$$f_{gs} - k_{es}(x_a - x_{es}) - f_{mot} = 0 \tag{D.4}$$

where k_{es} is the extent spring stiffness (to account for incomplete adaptation [144]). For small pertubations in the calcium concentration,

$$\frac{\partial x_a}{\partial C_{fa}^o} = \frac{k_{gs}}{k_{es}+k_{gs}}(\frac{\partial x}{\partial C_{fa}^o} - d\frac{\partial P_0}{\partial C_{fa}^o}) \tag{D.5}$$

At equilibrium, the equation governing the displacement of the HB, Eq. 5, is reduced to:

$$N\gamma f_{gs} + K_{sp}(u_{hb} - X_{sp}) = F_{ext}. \tag{D.6}$$

For small pertubations in the calcium concentration,

$$N\gamma k_{gs}(\frac{\partial x}{\partial C_{fa}^o} - \frac{\partial x_a}{\partial C_{fa}^o} - d\frac{\partial P_0}{\partial C_{fa}^o}) + K_{sp}\gamma\frac{\partial x}{\partial C_{fa}^o} = \frac{\partial F_{ext}}{\partial C_{fa}^o} \tag{D.7}$$

To determine the new operating point would require solving Eqs. D.3, D.5 and D.7. However, the right hand side in Eq. D.7 depends on the forces in the cochlea at equilibrium and on the resting position. Rather than computing the equilibrium in our macroscopic model of the cochlea, we make an approximation so as to uncouple the resting position of the HB from the other equilibrium displacements and forces in the cochlea. We chose to neglect the change in the external force: if we assume that $\frac{\partial F_{ext}}{\partial C_{fa}^o} = 0$, the pertubations in the resting probabilities, resting HB position and

Parameter	Description	Value
k_{es}	Extent spring stiffness	$5mN/m$
K_{sp}	Stereocilia pivot stiffness	$3.3mN/m$

resting motor position is found by solving Eqs. D.3, D.5 and D.7, with the right hand side of Eq. D.7 set to 0.

The dynamics of the HB in response to small harmonic pertubations is then computed using Eq. 4.5. The matrix of the system, $\mathbf{A}$, is evaluated for the new operating point of the HB with the new calcium concentration and the resulting HB and slow adaptation motor position ($\mathbf{P^n}$,x^n,x_a^n), where:

$$\mathbf{P^n} = \mathbf{P^s} + \frac{\partial \mathbf{P}}{\partial C_{fa}^o} \delta C_{fa}^o \tag{D.8}$$

$$x^n = \frac{\partial \mathbf{x}}{\partial C_{fa}^o} \delta C_{fa}^o \tag{D.9}$$

$$x_a^n = \frac{\partial \mathbf{x_a}}{\partial C_{fa}^o} \delta C_{fa}^o \tag{D.10}$$

The parameters necessary to compute the effect of calcium on acoustic stimulation are listed in Table D.

APPENDIX E

Optimization of the transduction channel

The parameters of the HB model (the rates k_1, k_2, k_4 and the ratio r_1, r_2 and r_4) are chosen to maximize the energy generated by the HB. The value of k_3, k_5, r_3 and r_5 are then computed by Eqs. C.11 and C.10. Instead of using k_1, k_2 and k_4 for the optimization, nondimensional parameters are used: $R_1 = \frac{k_1}{\omega_{ref}}$, $R_2 = \frac{k_2}{\omega_{ref}}$ and r_{K_B}, where ω_{ref} is a reference angular frequency and r_{K_B} is given by:

$$r_{K_B} = \frac{K_B^c}{K_B^o} \tag{E.1}$$

ω_{ref} is chosen to equal to k_1 (so that $K_1 = 1$). The angular frequency, ω, is varied

between $0.01 \times \omega_{ref}$ and $10 \times \omega_{ref}$. The following optimization problem [115] is solved:

$$
\begin{aligned}
&\text{maximize} && f(R_2, r_{K_B}, r_1, r_2) = \max_{\omega}\Big[E_{hb}(\omega, R_2, r_{K_B}, r_1, r_2)\Big] \\
&\text{with respect to} && R_2, r_{K_B}, r_1, r_2 \\
&\text{subject to} && 0.3 \leq P_0^s \leq 0.7 \\
& && 0.1\omega_{ref} \leq \omega_{peak} \\
& && 0.01 \leq R_2 \leq 4 \\
& && 0.01 \leq r_{K_B} \leq 10 \\
& && exp(-20) \leq r_1 \leq 1.0 \\
& && 0.05 \leq r_2 \leq 1.0
\end{aligned}
$$

The objective function f, is the maximum of the energy generated by the HB over the frequencies considered here. The parameters are optimized to maximize this objective function. The resting probability, P_0^s, is constrained to be between 0.3 and 0.7. ω_{peak} denotes the peak radian frequency of the transduction channel sensitivity $|J(\omega)|$; it is constrained to be at least $0.1\omega_{ref}$. The other constraints are the upper and lower bounds on the optimization variables. The opposite of the objective function $(-f)$ is minimized using the routine $fmincon$ in MATLAB for nonlinear constrained minimization with a line search algorithm. The optimal values of the optimization parameters are listed in the second column of Table S2. Only the upper bound on the ratio of the calcium binding coefficient, r_{K_B}, is an active constraint.

The magnitude and phase of the transduction channel filter, as well as the real part of the active HB stiffness and mechanical energy generated by the HB are plotted as a function of the normalized frequency $\Omega = \frac{\omega}{\omega_{ref}}$ in Fig. E.1. The magnitude of the transduction channel is maximal for $\Omega = 0.37$ and the mechanical energy generated by the HB is maximal for $\Omega = 0.065$. We found that the energy that the HB can deliver is too small to have a significant impact on cochlear amplification. However the

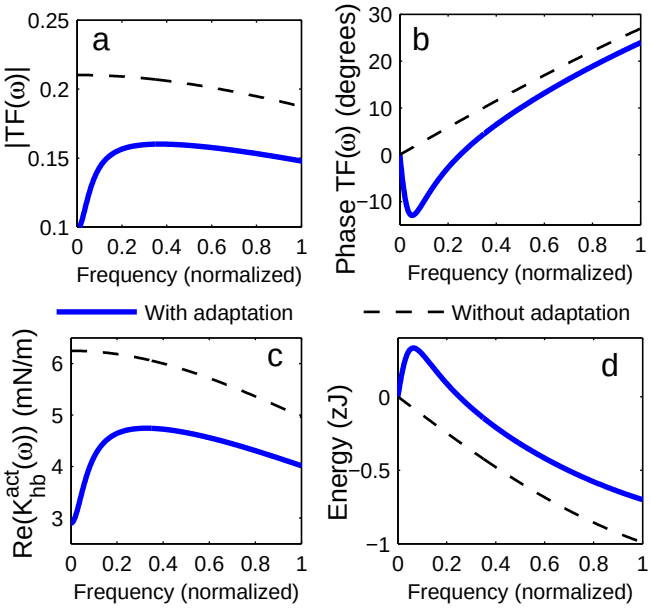

Figure E.1: Response of the HB with optimal parameters, as a function of the nondimensional frequency Ω. a. Magnitude and b. phase of the transduction channel filter, $TF(\omega)$. c. Real part of the active HB stiffness and d. mechanical energy generated by the HB per cycle for a 0.5nm HB displacement. Thick solid line: adaptation is included. Thin dashed line: adaptation is not taken into account

Parameter	With $K_1 = 1.0$	For peak frequency of 17kHz
R_1	1.0	2.7027
R_2	0.107	0.2892
r_{K_B}	10	10
r_1	0.8143	0.8143
r_2	0.4974	0.4974
r_4	0.1256	0.1256

energy delivered by somatic motility depends on the sensitivity of the MET channel [121]. Therefore in the macroscopic simulations of the cochlea we chose to tune the transduction channel filter, $TF(\omega)$, to the CF. This can be obtained by dividing the value of R_1 and R_2 by 0.37. The resulting nondimensional parameter values are shown in the 3rd column of Table E for the 17kHz best place.

APPENDIX F

Computation of the error in the nonlinear simulations

We denote $\tilde{u}_{bm}^m(x)$ the approximate solution of the component m of the BM displacement at the location x and $u_{bm}^m(x)$ the converged solution of the component m of the BM displacement at the location x. The relative error at the location x in the component m of the BM displacement is defined as:

$$E(x,m) = |\frac{\tilde{u}_{bm}^m(x) - u_{bm}^m(x)}{u_{bm}^m(x)}| \tag{F.1}$$

The root mean square of the relative error in the component m of the BM displacement is:

$$RMS_E(m) = \sqrt{\frac{1}{N_x}\sum_{i_x=1}^{N_x} E(x(i_x),m)^2} \tag{F.2}$$

where N_x is the number of spatial points in the longitudinal direction ($N_x = 741$ has been used for the simulations).

BIBLIOGRAPHY

BIBLIOGRAPHY

[1] C. C. Abnet and D. M. Freeman. Deformations of the isolated mouse tectorial membrane produced by oscillatory forces. *Hearing Research*, 144:29–46, 2000.

[2] J. B. Allen. Cochlear micromechanics – a physical model of transduction. *Journal of the Acoustical Society of America*, 68(6):1660–1670, 1980.

[3] J. Ashmore. Cochlear outer hair cell motility. *Physiol. Rev.*, 88(1):173–210, January 2008.

[4] J. Ashmore, P. Avan, W. E. Brownell, P. Dallos, K. Dierkes, R. Fettiplace, K. Grosh, C. M. Hackney, A. J. Hudspeth, F. Julicher, B. Lindner, P. Martin, J. Meaud, C. Petit, J. R. S. Sacchi, and B. Canlon. The remarkable cochlear amplifier. *Hearing Research*, 266:1–17, 2010.

[5] J. A. Assad and D. P. Corey. An active motor model for adaptation by vertebrate hair-cells. *Journal Of Neuroscience*, 12(9):3291–3309, 1992.

[6] P.W. Atkins. *Physical chemistry.* 1986.

[7] G. V. Bekesy. *Experiments in hearing.* McGraw Hill, NY, 1960.

[8] M. Beurg, J. H. Nam, A. Crawford, and R. Fettiplace. The actions of calcium on hair bundle mechanics in mammalian cochlear hair cells. *Biophysical Journal*, 94(7):2639–2653, 2008.

[9] D. Bozovic and A. J. Hudspeth. Hair-bundle movements elicited by transepithelial electrical stimulation of hair cells in the sacculus of the bullfrog. *Proceedings Of The National Academy Of Sciences Of The United States Of America*, 100(3):958–963, 2003.

[10] W. E. Brownell. Microscopic observation of cochlear hair cell motility. *Scanning Electron Microscopy*, pages 1401–1406, 1984.

[11] W. E. Brownell, C. R. Bader, D. Bertrand, and Y. De Ribaupierre. Evoked mechanical responses of isolated cochlear hair cells. *Science.*, 227:194–196, 1985.

[12] T. J. F. Buunen and W. S. Rhode. Response of fibers in the cat's auditory nerve to the cubic difference tone. *The Journal of the Acoustical Society of America*, 64(3):772–781, 1978.

[13] T. M. Cameron and J. H. Griffin. An alternating frequency/time domain method for calculating the steady-state response of nonlinear dynamic systems. *Journal of Applied Mechanics*, 56(1):149–154, 1989.

[14] R. S. Chadwick. Compression, gain, and nonlinear distortion in an active cochlear model with subpartitions. *Proceedings of the National Academy of Sciences of the United States of America*, 95(25):14594–14599, 1998.

[15] R. S. Chadwick, E. K. Dimitriadis, and K. H. Iwasa. Active control of waves in a cochlear model with subpartitions. *Proc. Natl. Acad. Sci. USA.*, 93:2564–2569, 1996.

[16] M. A. Cheatham, S. Low-Zeddies, K. Naik, R. Edge, J. Zheng, C. T. Anderson, and P. Dallos. A chimera analysis of prestin knock-out mice. *Journal of Neuroscience*, 29(38):12000–12008, 2009.

[17] Y. Choe, M. O. Magnasco, and A. J. Hudspeth. A model for amplification of hair-bundle motion by cyclical binding of ca2+ to mechanoelectrical-transduction channels. *Proceedings of the National Academy of Sciences of the United States of America*, 95(26):15321–15326, 1998.

[18] Niloy Choudhury, Guiju Song, Fangyi Chen, Scott Matthews, Tanja Tschinkel, Jiefu Zheng, Steven L. Jacques, and Alfred L. Nuttall. Low coherence interferometry of the cochlear partition. *Hearing Research*, 220(1-2):1 – 9, 2006.

[19] N. P. Cooper. Two-tone suppression in cochlear mechanics. *Journal of the Acoustical Society of America*, 99(5):3087–3098, 1996.

[20] N. P. Cooper. Harmonic distortion on the basilar membrane in the basal turn of the guinea-pig cochlea. *Journal of Physiology-London*, 509(1):277–288, 1998.

[21] N. P. Cooper. Radial variation in the vibrations of the cochlear partition. *Proceedings of the International Symposium On Recent Developments In Auditory Mechanics*, pages 109–115, 2000.

[22] N. P. Cooper and W. Dong. Sound-evoked changes in the baseline position of the cochlear partition at the apex of the guinea-pig cochlea. *Journal of Physiology-London*, 527:90P–91P, 2000.

[23] N. P. Cooper and W. S. Rhode. Basilar mechanics in the hook region of the cat and guinea pig cochlea: sharp tuning and nonlinearity in the absence of baseline position shifts. *Hearing Research*, 63(1-2):163–190, 1992.

[24] N. P. Cooper and W. S. Rhode. Nonlinear mechanics at the apex of the guinea-pig cochlea. *Hearing Research*, 82(2):225–243, 1995.

[25] N. P. Cooper and W. S. Rhode. Two-tone suppression in apical cochlear mechanics. *Auditory Neuroscience*, 3(2):123–134, 1996.

[26] N. P. Cooper and W. S. Rhode. Mechanical responses to two-tone distortion products in the apical and basal turns of the mammalian cochlea. *Journal of Neurophysiology*, 78(1):261–270, 1997.

[27] D. P. Corey and A. J. Hudspeth. Kinetics of the receptor current in bullfrog saccular hair-cells. *Journal Of Neuroscience*, 3(5):962–976, 1983.

[28] A. C. Crawford, M. G. Evans, and R. Fettiplace. Activation and adaptation of transducer currents in turtle hair-cells. *Journal Of Physiology-London*, 419:405–434, 1989.

[29] P. Dallos. Overview: Cochlear neurobiology. In Peter Dallos, Arthur N. Popper, and Richard R. Fay, editors, *The Cochlea*, pages 1–43. Springer, New York, 1996.

[30] P. Dallos. Organ of corti kinematics. *JARO - Journal of the Association for Research in Otolaryngology*, 4(3):416–421, 2003.

[31] P. Dallos and B. N. Evans. High-frequency motility of outer hair cells and the cochlear amplifier. *Science*, 267:2006 – 2009, 1995.

[32] P. Dallos, X. D. Wu, M. A. Cheatham, J. G. Gao, J. Zheng, C. T. Anderson, S. P. Jia, X. Wang, W. H. Y. Cheng, S. Sengupta, D. Z. Z. He, and J. Zuo. Prestin-based outer hair cell motility is necessary for mammalian cochlear amplification. *Neuron*, 58(3):333–339, 2008.

[33] H. Davis. An active process in cochlear mechanics. *Hearing Research*, 9(1):79–90, 1983.

[34] E. de Boer. No sharpening? a challenge for cochlear mechanics. *The Journal of the Acoustical Society of America*, 73:567–573, 1983.

[35] E. de Boer and A. L. Nuttall. The mechanical waveform of the basilar membrane. iii. intensity effects. *Journal of the Acoustical Society of America*, 107(3):1497–1507, 2000.

[36] Egbert de Boer, Jiefu Zheng, Edward Porsov, and Alfred L. Nuttall. Inverted direction of wave propagation (idwp) in the cochlea. *J. Acoust. Soc. Am.*, 123(3):1513–1521, 2008.

[37] E. deBoer. On active and passive cochlear models - toward a generalized analysis. *Journal of the Acoustical Society of America*, 73(2):574–576, 1983.

[38] N. V. Deo. *Micro and Macromechanics of the mammalian cochlea*. PhD thesis, University of Michigan, 2006.

[39] N. V. Deo and K. Grosh. Simplified nonlinear outer hair cell models. *Journal of the Acoustical Society of America*, 117(4):2141–2146, 2005.

[40] Wei Dong and Elizabeth S. Olson. Two-tone distortion in intracochlear pressure. *The Journal of the Acoustical Society of America*, 117(5):2999–3015, 2005.

[41] R. A. Eatock. Adaptation in hair cells. *Annual Review Of Neuroscience*, 23:285–314, 2000.

[42] C. Fernandez. Dimensions of the cochlea (guinea pig). *Journal of the Acoustical Society of America*, 24(5):519–523, 1952.

[43] G. Frank, W. Hemmert, and A. W. Gummer. Limiting dynamics of high-frequency electromechanical transduction of outer hair cells. *Proceedings of the National Academy of Sciences of the United States of America*, 96(8):4420–4425, 1999.

[44] A. Fridberger, J. B. de Monvel, J. Zheng, N. Hu, Y. Zou, T. Ren, and A. Nuttall. Organ of corti potentials and the motion of the basilar membrane. *The Journal of Neuroscience*, 24(45):10057–10063, 2004.

[45] Anders Fridberger, ke Flock, Mats Ulfendahl, and Britta Flock. Acoustic overstimulation increases outer hair cell ca2+ concentrations and causes dynamic contractions of the hearing organ. *Proceedings of the National Academy of Sciences of the United States of America*, 95(12):7127–7132, 1998.

[46] J. G. Gao, X. Wang, X. D. Wu, S. Aguinaga, K. Huynh, S. P. Jia, K. Matsuda, M. Patel, J. Zheng, M. A. Cheatham, D. Z. He, P. Dallos, and J. Zuo. Prestin-based outer hair cell electromotility in knockin mice does not appear to adiust the operating point of a cilia-based amplifier. *Proceedings of the National Academy of Sciences of the United States of America*, 104(30):12542–12547, 2007.

[47] N. Gavara and R.S. Chadwick. Collagen-based mechanical anisotropy of the tectorial membrane: implications for inter-row coupling of outer hair cell bundles. *PLoSOne*, 4:e4877, 2009.

[48] C. D. Geisler. A model of the effect of outer hair cell motility on coclear vibrations. *Hearing Research*, 24:125–131, 1986.

[49] C. D. Geisler. A cochlear model using feedback from motile outer hair cells. *Hearing Research*, 54:105–117, 1991.

[50] C. D. Geisler. *From Sound to Synapse*. Oxford Press , New York, 1998.

[51] C. D. Geisler and A. L. Nuttall. Two-tone suppression of basilar membrane vibrations in the base of the guinea pig cochlea using "low-side" suppressors. *Journal of the Acoustical Society of America*, 102(1):430–440, 1997.

[52] C. D. Geisler and C. Sang. A cochlear model using feed-forward outer-hair cells forces. *Hearing Research*, 86:132–146, 1995.

[53] C.Daniel Geisler, Graeme K. Yates, Robert B. Patuzzi, and Brian M. Johnstone. Saturation of outer hair cell receptor currents causes two-tone suppression. *Hearing Research*, 44(2-3):241–256, 1990.

[54] R. Ghaffari. *The functional role of the tectorial membrane in the cochlear mechanics*. PhD thesis, MIT, 2008.

[55] R. Ghaffari, A. J. Aranyosi, and D. M. Freeman. Longitudinally propagating traveling waves of the mammalian tectorial membrane. *Proceedings Of The National Academy Of Sciences Of The United States Of America*, 104(42):16510–16515, 2007.

[56] E. Givelberg and J. Bunn. A comprehensive three-dimensional model of the cochlea. *Journal of Computational Physics*, 191(2):377–391, 2003.

[57] J. W. W. Gu, W. Hemmert, D. M. Freeman, and A. J. Aranyosi. Frequency-dependent shear impedance of the tectorial membrane. *Biophysical Journal*, 95(5):2529–2538, 2008.

[58] R. Gueta, D. Barlam, R. Z. Shneck, and I. Rousso. Measurement of the mechanical properties of isolated tectorial membrane using atomic force microscopy. *Proceedings Of The National Academy Of Sciences Of The United States Of America*, 103(40):14790–14795, 2006.

[59] A. W. Gummer, W. Hemmert, and H. P. Zenner. Resonant tectorial membrane motion in the inner ear: Its crucial role in frequency tuning. *Proceedings of the National Academy of Sciences of the United States of America*, 93(16):8727–8732, 1996.

[60] A. W. Gummer, B. M. Johnstone, and N. J. Armstrong. Direct measurement of basilar membrane stiffness in guinea pig. *Journal of Acoustical Society of America*, 70(5):1298–1309, 1981.

[61] D. Z. Z. He and P. Dallos. Somatic stiffness of cochlear outer hair cells is voltage-dependent. *Proc. Natl. Acad. Sci. USA.*, 96(14):8223–8228, 1999.

[62] D. Z. Z. He and P. Dallos. Properties of voltage-dependant somatic stiffness of cochlear outer hair cells. *J. Assoc. Res. Otolaryngol.*, 01:64–81, 2000.

[63] D. Z. Z. He, S. P. Jia, and P. Dallos. Mechanoelectrical transduction of adult outer hair cells studied in a gerbil hemicochlea. *Nature*, 429(6993):766–770, 2004.

[64] W. X. He, A. L. Nuttall, and T. Y. Ren. Two-tone distortion at different longitudinal locations on the basilar membrane. *Hearing Research*, 228(1-2):112–122, 2007.

[65] SS Hong and DM Freeman. Doppler optical cocherence microscopy for studies of cochlear mechanics. *Journal of Biomedical Optics*, 11, 2006.

[66] G. D. Housley and J. F. Ashmore. Ionic currents of outer hair-cells isolated from the guinea-pig cochlea. *Journal of Physiology-London*, 448:73–98, 1992.

[67] J. Howard and A. J. Hudspeth. Compliance of the hair bundle associated with gating of mechanoelectrical transduction channels in the bullfrogs saccular hair cell. *Neuron*, 1(3):189–199, 1988.

[68] A. Hubbard. A traveling-wave amplifier model of the cochlea. *Science*, 259:68–71, 1993.

[69] A. J. Hudspeth. How the ear's works work. *Nature*, 341:397–404, 1989.

[70] T. J. R. Hughes. *The Finite Element Method: Linear Static and Dynamic Finite Element Analysis*. Dover, 2000.

[71] K. H. Iwasa. A two-state piezoelectric model for outer hair cell motility. *Biophysical Journal*, 81(5):2495–2506, 2001.

[72] K. H. Iwasa and M. Adachi. Force generation in the outer hair cell of the cochlea. *Biophys. J.*, 73:546–555, 1997.

[73] K. H. Iwasa and B. Sul. Effect of the cochlear microphonic on the limiting frequency of the mammalian ear. *Journal Of The Acoustical Society Of America*, 124(3):1607–1612, 2008.

[74] L. J. Kanis. *Cochlear Nonlinearity A Computational Model of the Cochlea Solved in the Frequency Domain*. PhD thesis, Universiteit van Amsterdam, 1995.

[75] L. J. Kanis and E. de Boer. Self-suppression in a locally active nonlinear model of the cochlea - a quasi-linear approach. *Journal of the Acoustical Society of America*, 94(6):3199–3206, 1993.

[76] L. J. Kanis and E. de Boer. 2-tone suppression in a locally active nonlinear model of the cochlea. *Journal of the Acoustical Society of America*, 96(4):2156–2165, 1994.

[77] L. J. Kanis and E. deBoer. Comparing frequency-domain with time-domain solutions for a locally active nonlinear model of the cochlea. *Journal of the Acoustical Society of America*, 100(4):2543–2546, 1996.

[78] D. T. Kemp. Simulated acoustic emissions from within the human auditory system. *Journal of the Acoustical Society of America*, 64:1386–1391, 1978.

[79] D. T. Kemp. Evidence of mechanical nonlinearity and frequency selective wave amplification in the cochlea. *Archives Of Oto-Rhino-Laryngology-Archiv Fur Ohren-Nasen-Und Kehlkopfheilkunde*, 224(1-2):37–45, 1979.

[80] H. J. Kennedy, A. C. Crawford, and R. Fettiplace. Force generation by mammalian hair bundles supports a role in cochlear amplification. *Nature*, 433(7028):880–883, 2005.

[81] H. J. Kennedy, M. G. Evans, A. C. Crawford, and R. Fettiplace. Fast adaptation of mechanoelectrical transducer channels in mammalian cochlear hair cells. *Nature Neuroscience*, 6(8):832–836, 2003.

[82] S. M. Khanna and L. F. Hao. Reticular lamina vibrations in the apical turn of a living guinea pig cochlea. *Hearing Research*, 132:15–33, 1999.

[83] S. M. Khanna and L. F. Hao. Amplification in the apical turn of the cochlea with negative feedback. *Hearing Research*, 149(1-2):55–76, 2000.

[84] P. J. Kolston and J. F. Ashmore. Finite element micromechanical modeling of the cochlea in three dimensions. *Journal of the Acoustical Society of America*, 99:455–467, 1996.

[85] M. Kossl and I. J. Russell. The phase and magnitude of hair cell receptor potentials and frequency tuning in the guinea–pig cochlea. *Journal of Neuroscience*, 12(5):1575–1586, 1992.

[86] P. K. Legan, V. A. Lukashkina, R. J. Goodyear, M. Kossl, I. J. Russell, and G. P. Richardson. A targeted deletion in alpha-tectorin reveals that the tectorial membrane is required for the gain and timing of cochlear feedback. *Neuron*, 28(1):273–285, 2000.

[87] M. C. Liberman, J. Gao, D. Z. Z. He, X. Wu, S. Jia, and J. Zuo. Prestin is required for electromotility of the outer hair cell and for the cochlear amplifier. *Nature*, 419:300–304, 2002.

[88] K. M. Lim and C. R. Steele. A three-dimensional nonlinear active cochlear model analyzed by the wkb-numeric method. *Hearing Research*, 170:190–205, 2002.

[89] S. Liu and R. D. White. Orthotropic material properties of the gerbil basilar membrane. *Journal of the Acoustical Society of America*, 123(4):2160–2171, 2008.

[90] Y. W. Liu and S. T. Neely. Distortion product emissions from a cochlear model with nonlinear mechanoelectrical transduction in outer hair cells. *Journal of the Acoustical Society of America*, 127(4):2420–2432, 2010.

[91] F. Mammano and R. Nobili. Biophysics of the cochlea: Linear approximation. *Journal of the Acoustical Society of America*, 93:3320–3332, 1993.

[92] Daphne Manoussaki, Richard S. Chadwick, Darlene R. Ketten, Julie Arruda, Emilios K. Dimitriadis, and Jen T. O'Malley. The influence of cochlear shape on low-frequency hearing. *Proceedings of the National Academy of Sciences*, 105(16):6162–6166, 2008.

[93] V. S. Markin and A. J. Hudspeth. Gating-spring models of mechanoelectrical transduction by hair-cells of the internal ear. *Annual Review Of Biophysics And Biomolecular Structure*, 24:59–83, 1995.

[94] P. Martin, D. Bozovic, Y. Choe, and A. J. Hudspeth. Spontaneous oscillation by hair bundles of the bullfrog's sacculus. *Journal of Neuroscience*, 23(11):4533–4548, 2003.

[95] P. Martin and A. J. Hudspeth. Active hair-bundle movements can amplify a hair cell's response to oscillatory mechanical stimuli. *Proceedings of the National Academy of Sciences of the United States of America*, 96(25):14306–14311, 1999.

[96] Pascal Martin. Active hair-bundle motility of the hair cells of vestibular and auditory organs, 2007.

[97] Julien Meaud and Karl Grosh. The effect of tectorial membrane and basilar membrane longitudinal coupling in cochlear mechanics. *The Journal of the Acoustical Society of America*, 127(3):1411–1421, 2010.

[98] S.W. F. Meenderink and M. van der Heijden. Reverse cochlear propagation in the intact cochlea of the gerbil: Evidence for slow traveling waves. *J Neurophysiol*, 103(3):1448–1455, 2010.

[99] P. Mistrik, C. Mullaley, F. Mammano, and J. Ashmore. Three-dimensional current flow in a large-scale model of the cochlea and the mechanism of amplification of sound. *Journal of The Royal Society Interface*, 6(32):279–291, 2009.

[100] D.C. Mountain and A.E. Hubbard. Rapid force production in the cochlea. *Hearing Research*, 42(2-3):195–202, 1989.

[101] R. C. Naidu and D. C. Mountain. Longitudinal coupling in the basilar membrane. *JARO*, 2(3):257–267, 2001.

[102] R. C. Naidu and D. C. Mountain. Basilar membrane tension calculations for the gerbil cochlea. *Journal Of The Acoustical Society Of America*, 121(2):994–1002, 2007.

[103] J. H. Nam and R. Fettiplace. Theoretical conditions for high-frequency hair bundle oscillations in auditory hair cells. *Biophysical Journal*, 95(10):4948–4962, 2008.

[104] S. Neely. A model of cochlear mechanics with outer hair cells motility. *Journal of the Acoustical Society of America*, 94:137–146, 1993.

[105] S. T. Neely. Finite-difference solution of a two-dimensional mathematical-model of the cochlea. *Journal of the Acoustical Society of America*, 69 (5):1386–1393, 1981.

[106] S. T. Neely and D. O. Kim. An active cochlear model showing sharp tuning and high-sensitivity. *Hearing Research*, 9(2):123–130, 1983.

[107] K. E. Nilsen and I. J. Russell. The spatial and temporal representation of a tone on the guinea pig basilar membrane. *Proceedings of the National Academy of Sciences of the United States of America*, 97(22):11751–11758, 2000.

[108] R. Nobili and F. Mammano. Biophysics of the cochlea ii: Stationary nonlinear phenomenology. *Journal of Acoustical Society America*, 99:2244–2255, 1996.

[109] A. L. Nuttal and D. F. Dolan. Two-tone suppresion of inner hair cell and basilar membrane responses in the guinea pig. *Journal of the Acoustical Society of America*, 93:390–400, 1993.

[110] A. L. Nuttall and D. Dolan. Steady-state sinusoidal velocity responses of the basilar membrane in guinea pig. *Journal of the Acoustical Society of America*, 99:1556–1565, 1996.

[111] A. L. Nuttall and D. F. Dolan. Two-tone suppresion of inner hair cell and basilar membrane responses in the guinea pig. *Journal of the Acoustical Society of America*, 93:390–400, 1993.

[112] A. L. Nuttall, D. F. Dolan, and G. Avinash. Laser doppler velocimetry of basilar membrane vibration. *Hearing Research*, 51:203–213, 1991.

[113] Alfred L. Nuttall and David F. Dolan. Inner hair cell responses to the 2f1-f2 intermodulation distortion product. *The Journal of the Acoustical Society of America*, 87(2):782–790, 1990.

[114] Elizabeth S. Olson. Harmonic distortion in intracochlear pressure and its analysis to explore the cochlear amplifier. *The Journal of the Acoustical Society of America*, 115(3):1230–1241, 2004.

[115] P.Y. Papalambros and D.J. Wilde. *Principles of optimal design. Modeling and computation*. Cambridge Univ Press, 2000.

[116] A. A. Parthasarathi. *Numerical Modeling and Electro-Acoustic Stimulus Response Analysis for Cochlear Mechanics*. PhD thesis, University of Michigan, 2000.

[117] A. A. Parthasarathi, K. Grosh, and A. L. Nuttall. Three-dimensional numerical modeling for global cochlear dynamics. *Journal of the Acoustical Society of America*, 107(1):474–485, 2000.

[118] A. A. Parthasarathi, K. Grosh, J. F. Zheng, and A. L. Nuttall. Effect of current stimulus on in vivo cochlear mechanics. *Journal of the Acoustical Society of America*, 113(1):442–452, 2003.

[119] Anthony W. Peng and Anthony J. Ricci. Somatic motility and hair bundle mechanics, are both necessary for cochlear amplification? *Hearing Research*, doi:10.1016/j.heares.2010.03.094, 2010.

[120] S. Ramamoorthy. *Passive and Active Structural Acoustic Filtering in Cochlear Mechanics Analysis and Applications*. PhD thesis, University of Michigan, 2004.

[121] S. Ramamoorthy, N. V. Deo, and K. Grosh. A mechano-electrio-acoustical model for the cochlea: Response to acoustic stimuli. *Journal of the Acoustic Society of America*, 121:2758–2773, 2007.

[122] Hudspeth A. J. Reichenbach T. A ratchet mechanism for amplification in low-frequency mammalian hearing. *PNAS*, 107:4973–4978, 2010.

[123] W. S. Rhode. Observation of the vibration of the basilar membrane in squirrel monkeys using the Mössbauer technique. *Journal of the Acoustical Society of America*, 49:1218–1231, 1971.

[124] W. S. Rhode. Basilar membrane mechanics in the 6-9 khz region of sensitive chinchilla cochleae. *Journal of the Acoustical Society of America*, 121(5):2792–2804, 2007.

[125] W.S. Rhode. *Psychophysics and physiology of hearing*, chapter Some observations on two tone interactions measured using the Mossbauer effect, pages 27–38. New York: Academic, 1977.

[126] A. J. Ricci, A. C. Crawford, and R. Fettiplace. Active hair bundle motion linked to fast transducer adaptation in auditory hair cells. *Journal Of Neuroscience*, 20(19):7131–7142, October 2000.

[127] A. J. Ricci, A. C. Crawford, and R. Fettiplace. Tonotopic variation in the conductance of the hair cell mechanotransducer channel. *Neuron*, 40(5):983–990, 2003.

[128] A. J. Ricci, H. J. Kennedy, A. C. Crawford, and R. Fettiplace. The transduction channel filter in auditory hair cells. *Journal Of Neuroscience*, 25(34):7831–7839, 2005.

[129] C. P. Richter, G. Emadi, G. Getnick, A. Quesnel, and P. Dallos. Tectorial membrane stiffness gradients. *Biophysical Journal*, 93:2265–2276, 2007.

[130] L. Robles, M. A. Ruggero, and N. C. Rich. Basilar membrane mechanics at the base of the chinchilla cochlea. i. input-output functions, tuning curves, and response phases. *Journal of the Acoustical Society of America*, 80(5):1364–1374, 1986.

[131] L. Robles, M. A. Ruggero, and N. C. Rich. Two-tone distortion in the basilar membrane of the cochlea. *Nature*, 349:413–414, 1991.

[132] L. Robles, M. A. Ruggero, and N. C. Rich. Two-tone distortion on the basilar membrane of the chinchilla cochlea. *Journal of Neurophysiology*, 77(5):2385–2399, 1997.

[133] M. A. Ruggero. Cochlear function – distortion in those good vibrations. *Current Biology*, 3(11):755–758, 1993.

[134] M. A. Ruggero, N. C. Rich, and A. Recio. Basilar membrane response to clicks. In T. Cazals, L. Demany, and K. Horner, editors, *Auditory Physiology and Perception*, pages 85–92. Pergamon Press, Oxford, 1992.

[135] M. A. Ruggero, L. Robles, and N. C. Rich. Two-tone suppression in the basilar membrane of the cochlea: mechanical basis of auditory-nerve rate suppression. *J Neurophysiol*, 68(4):1087–1099, 1992.

[136] I. J. Russell and M. Kossl. Voltage responses to tones of outer hair cells in the basal turn of the guinea-pig cochlea: Significance for electromotility and desensitization. *Proceedings: Biological Sciences*, 247(1319):97–105, 1992.

[137] I. J. Russell, P. K. Legan, V. A. Lukashkina, A. N. Lukashkin, R. J. Goodyear, and G. P. Richardson. Sharpened cochlear tuning in a mouse with a genetically modified tectorial membrane. *Nature Neuroscience*, 10(2):215–223, 2007.

[138] Murray B. Sachs and Nelson Y. S. Kiang. Two-tone inhibition in auditory-nerve fibers. *The Journal of the Acoustical Society of America*, 43(5):1120–1128, 1968.

[139] Alec N. Salt, Naoki Inamura, Ruediger Thalmann, and Arti Vora. Calcium gradients in inner ear endolymph. *American Journal of Otolaryngology*, 10(6):371–375, 1989.

[140] J. Santos-Sacchi. On the frequency limit and phase of outer hair cell motility: Effect of the membrane filter. *Journal of Neuroscience*, 12:1906–1916, 1992.

[141] Joseph Santos-Sacchi, Lei Song, Jiefu Zheng, and Alfred L. Nuttall. Control of mammalian cochlear amplification by chloride anions. *J. Neurosci.*, 26(15):3992–3998, 2006.

[142] P. M. Sellick, R. B. Patuzzi, and B. M. Johnstone. Measurement of the basilar membrane motion in the guinea pig cochlea using the Mössbauer technique. *Journal of the Acoustical Society of America*, 72:131–141, 1982.

[143] P. M. Sellick and I. J. Russell. 2-tone suppression in cochlear hair-cells. *Hearing Research*, 1(3):227–236, 1979.

[144] G. M. G. Shepherd and D. P. Corey. The extent of adaptation in bullfrog saccular hair-cells. *Journal Of Neuroscience*, 14(10):6217–6229, 1994.

[145] B. Shoelson, E. K. Dimitriadis, H. Cai, B. Kachar, and R. S. Chadwick. Evidence and implications of inhomogeneity in tectorial membrane elasticity. *Biophysical Journal*, 87(4):27682777, 2004.

[146] N. Slepecky. Structure of the Mammalian Cochlea. In P. Dallos, A. Popper, and R. Fay, editors, *The Cochlea*, pages 44–129. Springer–Verlag, New York, 1996.

[147] A. A. Spector, W. E. Brownell, and A. S. Popel. Effect of outer hair cell piezoelectricity on high-frequency receptor potentials. *Journal of the Acoustical Society of America*, 113(1):453–461, 2003.

[148] C. R. Steele and K. M. Lim. Cochlear model with three-dimensional fluid, inner sulcus and feed-forward mechanism. *Audiology Neuro-Otology*, 4:197–203, 1999.

[149] D. Strelioff. Computer-simulation of generation and distribution of cochlear potentials. *Journal of the Acoustical Society of America*, 54(3):620–629, 1973.

[150] D. Strelioff and A. Flock. Stiffness of sensory-cell hair bundles in the isolated guinea-pig cochleas. *Hearing Research*, 15(1):19–28, 1984.

[151] D Strelioff, A Flock, and KE Minser. Role of inner and outer-hair-cells in mechanical frequency-selectivity of the cochlea. *Hearing Research*, 18(2):169–175, 1985.

[152] B. Sul and K. H. Iwasa. Effectiveness of hair bundle motility as the cochlear amplifier. *Biophysical Journal*, 97(10):2653–2663, 2009.

[153] J. Y. Tinevez, F. Julicher, and P. Martin. Unifying the various incarnations of active hair-bundle motility by the vertebrate hair cell. *Biophysical Journal*, 93(11):4053–4067, December 2007.

[154] J. Tolomeo and C. R. Steele. Orthotropic piezoelectric properties of the cochlear outer hair cell wall. *Journal of the Acoustical Society of America*, 97(5):3006–3011, 1995.

[155] S. M. van Netten and C. J. Kros. Gating energies and forces of the mammalian hair cell transducer channel and related hair bundle mechanics. *Proceedings of the Royal Society of London. Series B: Biological Sciences*, 267(1455):1915–1923, 2000.

[156] L. Voldrich. Mechanical properties of the basilar membrane. *Acta Oto-Laryngologica*, 86(5-6):331–335, 1978.

[157] Y. C. Wu, A. J. Ricci, and R. Fettiplace. Two components of transducer adaptation in auditory hair cells. *Journal Of Neurophysiology*, 82(5):2171–2181, 1999.

[158] J. Zheng, W. Shen, D. Z. Z. He, K. B. Long, L. D. Madison, and P. Dallos. Prestin is the motor protein of cochlear outer hair cells. *Nature*, 405:149–155, 2000.

[159] J. F. Zheng, N. Deo, Y. Zou, K. Grosh, and A. L. Nuttall. Chlorpromazine alters cochlear mechanics and amplification: In vivo evidence for a role of stiffness modulation in the organ of corti. *Journal Of Neurophysiology*, 97(2):994–1004, 2007.

[160] Y. Zou, J. Zheng, T. Ren, and A. L. Nuttall. Cochlear transducer operating point adaption. In A. L. Nuttall, editor, *Auditory Mechanisms: Processes and Models*. World Scientific, 2006.

[161] J. J. Zwislocki and L. K. Cefaratti. Tectorial membrane ii: Stiffness measurement in vivo. *Hearing Research*, 42(2-3):211–228, 1989.

[162] J. J. Zwislocki and E. J. Kletsky. Tectorial membrane: A possible effect on frequency analysis in the cochlea. *Science*, 204:639–641, 1979.